SOUND ABSORPTION AND TRANSMISSION LOSS CHARACTERISTICS OF 3D PRINTED POROUS BIO-DEGRADABLE MATERIAL

Thesis

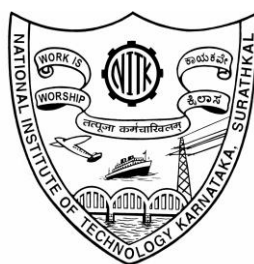Submitted in partial fulfilment of the requirements for the

degree of

DOCTOR OF PHILOSOPHY

by

SAILESH R

DEPARTMENT OF MECHANICAL ENGINEERING

NATIONAL INSTITUTE OF TECHNOLOGY

KARNATAKA, SURATHKAL, MANGALORE – 575025

June, 2022

DECLARATION

I hereby declare that the Research Thesis entitled "**SOUND ABSORPTION AND TRANSMISSION LOSS CHARACTERISTICS OF 3D PRINTED POROUS BIO DEGRADABLE MATERIAL**" which is being submitted to the **National Institute of Technology Karnataka, Surathkal** in partial fulfilment of the requirements for the award of the Degree of **Doctor of Philosophy** in **Department of Mechanical Engineering** is a *bonafide report of the research work carried out by me*. The material contained in this Research Thesis has not been submitted to any University or Institution for the award of any degree

Register Number   : 187092ME013

Name of the Research Scholar   : **SAILESH R**

Signature of the Research Scholar   :

Department of Mechanical Engineering

Place: **NITK, Surathkal**

Date: 21/06/2022

CERTIFICATE

This is to certify that the Research Thesis entitled "**SOUND ABSORPTION AND TRANSMISSION LOSS CHARACTERISTICS OF 3D PRINTED POROUS BIO-DEGRADABLE MATERIAL**" submitted by **Mr. SAILESH R** (Register Number: 187092ME013) as the record of the research work carried out by him, is accepted as the Research Thesis submission in partial fulfilment of the requirements for the award of degree of **Doctor of Philosophy**.

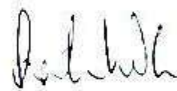**Research Guides**

Dr. Jeyaraj P

Associate Professor

Department of Mechanical Engineering

Dr. Mrityunjay Doddamani

Assistant Professor

Department of Mechanical Engineering

Chairman - DRPC

Date: 21 6 2022

ACKNOWLEDGEMENT

(Sailesh R)

ABSTRACT

Environmental concern pertaining to materials circular economy leads to the development of bio-degradable materials for various engineering applications. In recent years, noise pollution control and sound quality enhancement have been major concerns of industries, public places, automobiles, and even households. Noise pollution, especially at lower frequencies, causes a severe heath problem for humans, and it is difficult to control due to inadequate sound absorption capability of most of the existing material systems. Most of the materials currently used for sound absorption and transmission loss applications like glass wool, stone wool, plastics, synthetic foams, etc., are toxic and pose severe environmental and health issues. These materials leach toxins and are non-biodegradable, resulting in the production, usage, and disposal issues. Advancements in additive manufacturing motivated researchers to explore different eco-friendly materials and panels with unconventional geometric configurations that enhance their acoustic capabilities.

The influence of perforations having arbitrarily varying cross-sections on the acoustic behaviour of 3D printed bio-degradable panels made of Poly Lactic Acid (PLA) and wood/PLA materials is presented in this study. Circular perforations having six different types of cross-sectional variations, namely convergent-divergent (CD), divergent-convergent (DC), convergent (C), divergent (D) with two different perforation diameters are realized using fused filament fabrication (FFF) based 3D printing. Sound absorption (SA) and sound transmission loss (STL) characteristics are estimated by the impedance tube method. Results revealed that perforated panels with varying cross-sections have better SA than the conventional cylindrical perforation for the specific frequency range. Among the different cross-sectional variations explored, DC and D perforation patterns exhibit comparable and lower transmission losses with respect to the panels with 1 mm cylindrical pores. The sound transmission results of all other five specimens were significantly higher than the typical perforated panel with 8 mm cylindrical pores and observed to be increasing with frequency. This study indicate that geometrical variations of perforations play a vital role while designing the

soundproof panels. The experimental results compared with the numerical results are found to be in good agreement.

Samples with spherical perforations are considered to investigate the effect of graded porosity on acoustic performance. In these samples, the spherical bubble perforations are distributed either uniformly or graded across the specimen thickness. A sample having typical cylindrical perforations is also considered for the comparative analysis. The results reveal that the SA of samples with different types of functionally graded (FG) perforations is higher at low frequencies. Better sound absorption (SA coefficient higher than 0.8) with wider bandwidth has been observed for the sample with small sized (2 mm diameter) uniform spherical perforations. The STL of sample is highest among the specimens, and the difference in STL increases significantly with frequency. FG perforations exhibited superior performance for both SA and STL. The proposed graded spherical porosity can be effectively utilized in soundproofing applications across building and transportation sectors.

The impact of short wood fibers reinforcement on the 3D printed samples made of PLA for their acoustic characteristics is also investigated. Specimens having varying perforation geometries along with series connected uniform or graded size sphere perforations are analyzed. Results revealed that the addition of wood fibers in PLA improved the acoustic characteristics by significantly shifting the absorption range to the lower frequency side. Wood/PLA can be used in acoustic insulation for structural and transportation applications, especially where eco-friendliness and aesthetics are of major concern.

CONTENTS

LIST OF FIGURES

LIST OF TABLES

ABBREVIATIONS

ABS   : Acrylonitrile butadiene styrene

AM   : Additive manufacturing

ASTM   : American society for materials and testing

CFD   : Computational fluid dynamics

CNT   : Carbon nano tube

DAQ   : Data acquisition system

DLP   : Digital light processing

DMA   : Dynamic mechanical analysis

DSC   : Differential Scanning Calorimetry

FDM   : Fused deposition modelling

FFF   : Fused filament fabrication

FG   : Functionally graded

HRR   : Heat release rate

JCA   : Johnson-Champoux-Allard

MFI   : Melt flow index

MFR   : Melt flow rate

MPP   : Micro perforated panel

PLA   : Polylactic acid

PU   : Polyurethane

RMS   : Root mean square

SA   : Sound absorption

SAC   : Sound absorption coefficient

SLA   : Stereolithography

STL   : Sound transmission loss

TGA   : Thermogravimetric analysis

THD   : Total harmonic distortion

XRD   : X-ray Diffraction

3DP   : 3D printing

NOMENCLATURE

ω	Angular natural frequency	rad/s
ω_0	Resonant circular frequency	rad/s
A	Cross-sectional area	m^2
D	Air gap width between panel and wall	mm
M_1	Mass term of specific acoustic impedance	Pa-s/m
R	Resistive term of specific acoustic impedance	Pa-s/m
ρ	Density of air	kg/m^3
C	Velocity of sound in air	m/s
d	Diameter	mm
f	Natural frequency	Hz
f_0	Resonant frequency	Hz
t	Thickness of panel	mm
h	Total thickness of the sample	mm
p	porosity	%
α	Sound Absorption Coefficient	-----
R	Reflection Coefficient	-----

x

1   INTRODUCTION

In recent years, noise pollution control of the surrounding environment and enhancement of sound quality are major concerns of industries, public places, automobiles, and several household items (Jiang and Li 2018). Eco-friendly practices demand the utilization scope of bio-degradable and recyclable materials for numerous applications in controlling noise pollution (Putra et al. 2013). Noise pollution causes a severe problem for humans, and it is difficult to control due to inadequate sound absorption (SA) performance by most of the materials in practice (Leventhall 2004). Most of the materials currently being used on a large scale for acoustic applications, such as synthetic plastics, glass wool, and synthetic foams, are noxious and cause a grave threat to social life and the associated environment. The proliferation of synthetic plastics is already being rectified at all levels of humanity (Alshehrei 2017, Hong and Chen 2017). In addition to environmental hazards, they deplete the invaluable petroleum resources.

Glass fibers cause skin, eye, and respiratory irritations to living beings and act as a potential pollutant. Chemicals in polyurethane (PU) foams like propylene oxide, toluene diisocyanate (TDI), toluene, methylene chloride, hydrogen cyanide, volatile organic compounds and harmful flame retardants can cause irritation to eyes, skin, throat and nose. Further they can lead to headaches, nausea, loss of coordination; injure the liver, lungs, central nervous system, kidney and are cancerous, when exposed continuously. Toxicity of resulting effluents after the decomposition of plastics like Acrylonitrile butadiene styrene (ABS), nylon, polyester, polyethylenes, polystyrene, Polyvinyl chloride (PVC), and PU foams are analyzed under different temperature and environmental conditions by Levin (1987). The effects due to the inclusion of the additives during the manufacturing of these materials resulting in toxic products is analysed in his study. Assessment methods for fire toxicity of PU foams to quantify the harmful gases, especially carbon monoxide and hydrogen cyanide, were put forward by McKenna and Hull (2016). PU foams are easily ignitable, highly flammable, and emit highly toxic combustion products (Singh and Jain 2009). (Tarvainen et al. 1994)

reported that artificial mineral fibers cause irritant dermatitis. Contact dermatitis is also caused by phenol-formaldehyde urea, chrome compound, and epoxy resins.

Pioneering work in this area of acoustics was done by Maa (1975,1987,1998), a Chinese researcher who applied the acoustic principles formulated by Rayleigh and others for the design and fabrication of thin microperforated panels (MPPs) for better sound absorption with fundamental solutions. Simple computational fluid dynamic (CFD) models to calculate transfer impedances with end corrections for the analysis of MPP were developed by (Herdtle et al. 2013). The impedance is estimated from the pressure difference across a hole where a transient velocity is imposed. Micro-perforations employing microelectronic mechanical system (MEMS) technology were produced, and their normal absorption coefficients were analyzed by Qian et al. (2013). Better results were obtained with MPPs having micro-perforation of 100μm. MPP absorbers can have good sound absorption with high-frequency bandwidth that brings down the perforation diameter to sub-millimeter levels which is shown by Maa's findings.

Liu and Herrin (2010) reported that partitioning the back air cavity beside the MPP increases the attenuation to sound waves. Experimentation on thick MPPs with tapered perforations is done by Sakagami et al. (2008), and they found that these panels yielded a reasonable absorption coefficient with higher bandwidth. An investigation on the acoustic properties of concentric tube reverse flow resonators prepared through additive manufacturing techniques was carried out by Akiwate et al. (2019a). A double layer MPP with non-homogeneous perforations to get better absorption was fabricated by Mosa et al. (2020). They reported that both at higher and lower frequencies, the absorption bandwidth can be enhanced by varying the inter-plate distance and back cavity length, respectively. The progress in acoustics has been rapid during the recent decade, especially with the utilization of greener materials and the evolution of newer techniques in additive manufacturing, numerical analysis, and experimental techniques. Cylindrical, stepped perforations produce extra acoustic impedance enhancing dissipation depending on the cross-sectional ratio (Jiang et al. 2020).

Design, numerical modelling, and experimental validation of acoustic characteristics of periodic foam microstructures are carried out by Deshmukh et al. (2019). The absorption coefficients are high and consistent in the medium and high frequency regions. Manipulation of the opening of cells in PU foams by changing rheological properties during the foaming process is carried out by Park et al. (2017). The SA capacity of CNT reinforced PU foam is enhanced by the better surface interaction between the matrix and reinforcements (Baferani et al. 2017). Qian et al. (2014) developed a finite element model of thick MPPs having holes with perforations in the range of 100 μm. Results proved that these perforations improved absorption capacity significantly. Liu et al. (2017a) numerically synthesized a spiral-labyrinthine metamaterial with outstanding sound absorption and transmission loss capability. Meng et al. (2019) explored the usage of structural honeycomb sandwich panels by replacing one of the faceplates with perforated plate and studied sound absorption and sound transmission loss using analytical models. They also investigated the influence of different structures and compared the results with finite element models for validation.

An experimental procedure to find the SA coefficient of materials was proposed with a synthesized diffuse acoustic field under free-field conditions by Robin et al. (2014). Positive enhancement in SA by the usage of micro-grooved elements is highlighted by Auriemma (2017). Micro grooved elements can be used instead of MPPs where high levels of acoustic excitation and cost are of major concerns. SA of arbitrary cross sections is dealt with in detail by Ning et al. (2016). Triangular cross-sections had the best SA coefficient among the different geometries of perforations considered in the study. Simple pores and holes in both macro and micro structural elements can be oriented to get excellent acoustic performance, as mentioned by Attenborough (2019). The dissipation of acoustic energy of sound waves propagating through open and connected cells occurs through visco-inertial-thermal losses. A major part of acoustic energy disperses through viscous friction at cell walls through the heat conduction (Hoang et al. 2014). Another mechanism of the energy dissipation is visco-elastic frame damping, where intermolecular friction in solid walls converts the absorbed acoustic energy in vibration modes to heat (Biot et al. 1962). In a polymer foam, the visco-

inertial-thermal losses exceed the acoustic losses caused by viscoelastic frame damping (Park et al. 2017). Thus, by arranging the internal cell structure properly in the macro geometry, one can achieve good SA performance by virtue of enhanced dissipation. Latest 3D printing techniques can very well achieve this.

1.1 PLA – material

The usage of Polylactic acid (PLA) as a high potential green material has been discussed in this section. Table 1.1 gives a list of biodegradable polymers. Among them, PLA is the most popular material with comparable physical, mechanical, thermal, and acoustic properties with almost all materials used in the industry. PLA is an easily mouldable and 3D printable material widely used due to its surface finish, intricacy,

Table 1.1 Biodegradable polymers (Netravali and Chabba 2003).

	Natural		Synthetic
1	Polysaccharides	1	Poly (Amides)
	Starch	2	Poly (Anhydrides)
	Cellulose	3	Poly (Amide-Enamines)
	Chitin	4	Poly (Vinyl Alcohol)
	Pullulan	5	Poly (Ethylene-Co-Vinyl Alcohol)
	Levan	6	Poly (vinyl acetate)
	Konjac	7	Polyesters
	Elsinan		Poly (Glycolic Acid)
2	Proteins		Poly (Lactic Acid)
	Collagen/Gelatin		Poly (Caprolactone)
	Casein, Albumin, Fibrogen, Silks, Elastins		Poly (Ortho Esters)
	Protein From Grains	8	Poly (Ethylene Oxide)
3	Polyesters	9	Some Poly (Urethanes)
	Polyhydroxy Alkanoates	10	Poly (Phosphazines)
4	Other Polymers	11	Poly (Imino Carbomates)
	Lignin	12	Some Poly (Acrylates)
	Lipids		
	Shellac		
	Natural rubber		

dimensional accuracy, and printing conditions. A significant amount of research is currently going on to develop high-performance, sustainable materials from natural resources, but the great challenge is the feasible production costs and manufacturability. PLA is non-toxic, bio-degradable, clean and recyclable polymer, which makes it the most popular material to work with. Moreover, its mechanical properties and ease of working are comparable with the petroleum product counterparts (Farah et al. (2016) and Nampoothiri et al. (2010)). PLA is obtained by ring polymerization of lactic acid. Lactic acid can be chemically synthesized with the hydrolysis of lacronitrile using strong acids or fermenting corn, potato, beets, and sugar. PLA can also be blended with many materials to enhance its properties. Its increasing popularity and exponential growth of consumption have been illustrated in Figure 1.1. Mosanenzadeh et al. (2015) analyzed the acoustic behaviour of porous membranes having a structure of bimodal foam with a network of pores made from PLA of varying sizes interconnected, which were fabricated using a blend of PLA and polyethylene glycol. Chin et al. (2018) investigated sound absorption characteristics of biodegradable MPP made of kenaf fiber reinforced PLA composite which is prepared by mixing, hot-pressing, and drilling processes.
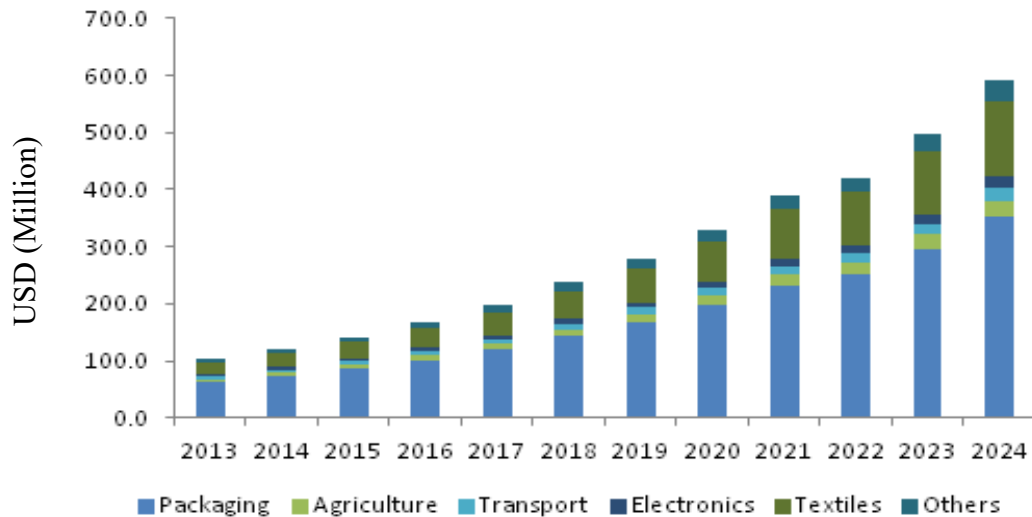
Figure1.1: Growing PLA market size by usage in USD million

(Source - gminsights.wordpress.com)

Ghaffari et al. (2015) studied the acoustic behaviour of MPPs made of PLA and Polyethylene glycol foam with pores of various sizes. PLA is a largely available

5

economical material of bio-origin, decayable, non-toxic, suitable disposable polymer with reasonable material and production costs and comparable mechanical characteristics that can be enhanced by blending and adding nanoparticles (Nofar et al. 2019). PLA has gathered substantial attention in biopolymer-based engineering applications due to its outstanding bio and eco-friendliness alongside the processability through the latest techniques like 3D printing (Eynde and Puyvelde 2018). Carlier et al. (2019) carried out an in-depth study and optimized fused deposition modelling (FDM) parameters for the extraction of PLA filament with and without additives. Structures made of PLA have a reasonably long life and are compostable when hydrolyzed at high temperatures under the action of microorganisms in industrial composting facilities (Karamanlioglu et al. 2017).

1.2   Wood-PLA material

Researchers have sorted ways to substantially replace polluting materials with bio-origin or recyclable alternatives in all fields for fabricating structures. Kariz et al. (2018) analyzed the effect of wood content on mechanical behaviour of PLA composites. They found that an increase in the wood powder content in a 3D filament of wood/PLA resulted in lower mechanical properties of printed specimens due to inhomogeneity of the mixture while blending and extrusion. Ecker et al. (2019) carried out tensile strength and stiffness tests on wood/PLA specimens and found that tensile strength and stiffness decreased due to the softening effect of wood in PLA. Firing characteristics of 3D printed wood/PLA and neat PLA are compared by Knez et al. (2021). They found that layer thickness and infill rate affected the time to sustained ignition and heat removal rate (HRR) time duration. Tensile characteristics, toughness, and energy absorption capacity of 3D printed specimens with different infill, layer height, and geometry were analyzed by Vigneshwaran and Venkateshwaran (2019). They found that the tensile strength decreased with increased layer height and increased with infill percentage, whereas tensile modulus increased with infill and layer height.

Tao et al. (2017) prepared a wood/PLA filament with 5 wt. % wood, and the 3D printed specimens were analyzed through TGA, XRD, and DSC tests and compared the tensile properties with pure PLA. They observed that the addition of wood altered the

material's microstructure, increased resistance to initial deformation, and showed a slight decrease in thermal degradation temperature and no change in melting temperature. Frass, a mixture of wood and faeces obtained from termites, was employed by Plarre et al. (2021) to 3D print the test specimens using the binder jet process. They reported that the strength is better due to the good flowability and packing density. The mechanical properties of 3D-printed samples depend remarkably on core configuration and infill rate (Ayrilmis et al. 2021). The mechanical properties were in the descending order with hexagonal, square and octagonal cores among the cores. A new alfa fiber and sawdust-wood reinforced composites were developed by Cherradi et al. (2021). They found that the composite had better SA characteristics than artificial fiber reinforced composites. Water absorption tests were performed on wood/PLA 3D printed specimens with four different thicknesses by Ayrilmis et al. (2019a). They found that water absorption was enhanced with increased printing layer thickness, whereas bulging of thickness was decreased. A tensile test on wood/PLA was performed by Petinakis et al. (2009). They observed that the tensile modulus is insensitive to the addition of coupling agents while the tensile strength increased remarkably. 3D printed wood fiber reinforced PLA was tested for mechanical characteristics by Ezzaraa et al. (2020). It is observed that mechanical properties are significantly influenced by the filler content and shape. Tensile, thermal, DMA, Vicat softening, and DSC tests of bamboo, wood, and coir fiber reinforced PLA were carried out by Zhang et al. (2012a).

3D printing and tensile testing of poplar wood reinforced PLA composite was carried out by Bhagia et al. (2020). They found that variability in density affected strength, whereas the β-glycosidic bond of polysaccharides influenced the modulus of elasticity. Ayrilmis (2018) found that the optimum layer thickness for 3D printed wood/PLA as 0.2 mm after checking for wettability, surface roughness, and printing time for four different layer thicknesses. Hemicellulose/PLA ratio was varied up to 25% in 3D printed scaffolds by Xu et al. (2018). It was identified as a highly promising compatible, renewable and degradable material in tissue engineering. The S-N curve for 3D printed wood/PLA with 8% wood fibers was experimentally plotted by Travieso et al. (2020). They found that endurance stress of 17.9 MPa provided an infinite life under test

7

conditions. Mechanical properties of wood/PLA were compared with pure PLA by Dong et al. (2018). They concluded that close layer to layer adhesion was present in pure PLA, resulting in better performance. Wettability and surface roughness of 3D printed specimens made of wood/PLA by varying the weight percentage of wood flour from 0 to 50% were analyzed by Ayrilmis et al. (2019b). They found that wettability decreased, whereas surface roughness increased considerably. The drawing temperature, speed, and percentage composition of straw in PLA composite filament were varied by Jiang et al. (2021). They observed that 3D printed specimens had reasonable hardness, bending, and tensile strength.

3D printed wood/PLA composite specimen containing 15 and 25 wt. % wood was studied by Kain et al. (2020). They analyzed the influence of the orientation angles of wood fiber from 0 to 90° with an interval of 15° and observed an improvement in mechanical properties upto 25%. The reinforcement of wood in PLA reduced the storage modulus by 40% (Kuzman et al. 2019) while the glass transition temperature remained unaffected. Ayrilmis et al. (2020) printed a set of gyroid structures and performed hardness, compression, face screw withdrawal resistance and bending tests. They reported that all the properties improved significantly when the skin thickness exceeded 2 mm.

1.3 Biodegradable sound absorption material

The acoustic absorption of a natural fiber composite combined with cylindrical granular materials was investigated by Mamtaz et al. (2017). They observed that the composites yielded high values of sound absorption. Othmani et al. (2017) demonstrated the utilization of sugarcane waste as a sound absorption material. Abdel et al. (2021) prepared a composite using saw dust reinforced in expanded polystyrene. They observed that the composite with 80% sawdust has a high absorption coefficient of about 0.9 at a low frequency of 315 Hz. Ghermezgoli et al. (2021) studied the effect of different ratios of hybrid waste wool composed of thick and fine wool fibers on thermal and acoustic properties. They observed that the mixing improved the thermal insulation and sound absorption characteristics of the material. Abdi et al. (2021) produced a composite from chrome shave and coffee silver skin. They found that the specimens of

30 and 50 mm thickness had an average absorption coefficient of 0.95 above 1 kHz at a density of 150 kg/m^3. Singh and Mohanty (2018) found that jute felt had the highest sound absorption coefficient among the naturally available materials. Taban et al. (2020) optimized the thickness of sound absorbers employing kenaf fibers. They found that at 40 mm thickness, the value of absorption coefficient increased up to 0.95 above 1250 Hz. Mehrzad et al. (2022) identified bagasse fibers as insulation and sound absorbing material in environment friendly buildings. The experimental and numerical results based on Johnson-Champoux-Allard (JCA) model were in good agreement pertaining to sound absorption curves. Soltani et al. (2020) carried out experimental and numerical studies on Yucca gloriosa fiber and found that samples of thickness 30 mm had a high absorption at 2500 Hz, and it can be used as a sustainable material to dissipate sound energy effectively. Hariprasad et al. (2020) studied sound absorption chracteristics of sample specimens made from hay, banana, sisal, kusha grass, and milkweed fibers. They observed that increased specimen thickness is not effective at the higher frequencies.

1.4   Acoustic materials and 3D printing

Advancements in 3D printing motivated researchers to explore different geometric configurations that enhance a material's SA capability. The SA characteristics of 3D printed ABS samples of three different open-porous configurations having the same volume ratio were compared by Vasina et al. (2020). They found that the SA depends on porous structure, excitation frequency, the thickness of the sample, and back cavity length. A procedure of modelling, 3D printing, and testing of a Kelvin cell structure was described by Rice et al. (2020). Their results signified the sensitiveness of SAC to geometric and surface finish uncertainties. Carpio et al. (2020) compared noise emitted by 3D printed perforated trailing-edge inserts in aerofoils with those produced using metallic foams. They found that a permeable trailing edge inserts with permeability (10^9) and tortuosity (0.05) and permeable extension to chord ratio of 0.05 provided the best trade-off between aerodynamic loss and broadband noise mitigation.

Interconnected pores in PU foams increased sound absorption remarkably (Zhang et al. 2012b). The open cell foams that interconnected the pores enhanced the sound

absorption by 100% compared to closed cell foams. Kennedy et al. (2019) compared the effect of different additive manufacturing techniques on SA of spherically porous metamaterials. The Stereolithography (SLA) technique was used to produce complex interior geometries with a remarkable surface finish. The FDM based specimens had high sound absorption due to low quality prints, and the digital light processing (DLP) process based samples had intermediate SA with low-cost option. 3D printing and other additive manufacturing techniques have excellent accuracy, flexibility, and finish for producing excellent sound absorbers having highly intricate structural geometry.

One dimensional functionally graded acoustic black hole beams manufactured by 3D printing technology with changing levels of visco-elastic characteristics are studied by Huang et al. (2019). The functionally graded acoustic black holes enhance the SAC compared to regular acoustic black holes by remarkably reducing the reflection of sound. Gao and Hou (2018) 3D printed a multi micro-helix metamaterial with PLA having high sound absorption characteristics. They achieved a very high sound absorption coefficient by optimizing helix dimensions. The microstructure of foam is designed to obtain desired acoustic performance using periodic foam structures, and prototypes of the same were manufactured using additive manufacturing by Deshmukh et al. (2019).

MPP backed up by a periodic honeycomb structure is fabricated using FDM by Akiwate et al. (2019b) with a perforated face sheet to study the effect of perforation shape with square, circle, and triangular geometries. Triangular perforation gave the best sound absorption coefficient among them for the same perimeter. The acoustic absorption capacity of a 3D printed micro-perforated multi-layered panel with different perforation ratios was investigated by Liu et al. (2017b). Statistical methods to find geometric characteristics through experimental absorption data for perforations of any shape were described by Liu et al. (2014). They varied the perforation angle and back air gap in 3D printed MPPs and found that increased perforation angle reduced absorption. In contrast, the frequency corresponding to the peak value was shifted to the lower side with an increasing air gap.

Temiz et al. (2015) obtained end correction coefficients in MPPs numerically for different end geometries and validated them experimentally. Akiwate et al. (2019a) successfully investigated the acoustic performance of 3D printed tubes with reverse flow resonators and showed that the longer tortuous paths improved the acoustic absorption. A double layer MPP with non-homogeneous perforations was worked upon to get better absorption by Mosa et al. (2020). They observed that the absorption bandwidth was enhanced at higher and lower frequencies by varying the inter-plate distance and back air gap, respectively. Acoustic parameters of thick MPPs with stepped holes were analyzed using thermoviscous acoustic simulations by Jiang et al. (2020). They found that stepped holes improved the absorption remarkably.

Advancements in additive manufacturing motivated researchers to explore different geometric configurations that enhance the SA capability. 3D printing and other additive manufacturing techniques have crossed limits on the accuracy, flexibility, and finish of producing excellent sound absorbers with highly complicated geometry. Zielinski (2015) carried out the design, generation, and testing of samples with arbitrary spherical foam configuration. They concluded that the relative number of pores and the window size of pores were decisive factors in determining sound absorption. Vasina et al. (2020) investigated the SA characteristics of 3D printed ABS samples of three different open-porous designs having the same volume ratio. They found that the SA depends on porous structure, excitation frequency, the thickness of the sample, and the back air gap.

Hentati et al. (2016) proposed a technique for minimizing the difference between computed and experimental values of the SA coefficient of foams. Simple pores and holes can be oriented for excellent acoustic performance, as Attenborough (2019) mentioned. Even though they cannot be currently manufactured by 3D printing, they can be fabricated and utilized in the future. Optimal sound absorption is attained when the size of pores is twice the viscous boundary layer thickness formed inside them (Cai et al. 2018). Kumar et al. (2020) proposed 3D printed ventilators made of PLA with high absorption coefficients and ventilation capacity and showed that effective noise control for low to mid frequency was possible by the designs.

Fotsing et al. (2019) observed that periodic acoustic structures manufactured by 3D printing gave acoustic characteristics comparable to porous materials. They also indicated that lower lattice parameters, lesser filament size, and proper filament orientation could enhance SA to a very great extent. Acoustic output parameters of 3D printed specimens were subjected to errors due to micro-geometric defects, dependent on the device and its wear, apart from the printing technique (Boulvert et al. 2020). An et al. (2020) printed a 3D truss lattice structure with high bandwidth of absorption in the low frequency range. Tunable 3D-printed small-scale resonators were proposed` to improve the STL of a curved panel by Droz et al. (2019). Since the inception of acoustic metamaterials, the field of acoustics has been driven by basic physical and geometrical concepts that guide the laws of structural design and contribute to the foundation for wave functionalities (Wu et al. 2018).

1.5   Closure

Even though a lot of innovative work is going on in acoustics and 3D printing using the latest numerical tools and experimental techniques, there is ample scope for more and more innovations making use of green materials and evolving techniques of additive manufacturing. Application-wise, these techniques help develop new products and ideas that may have wider applications in the field of structural, transportation, and entertainment.

From the literature reviewed

➢ *A significant amount of research is currently going on to get high-performance sustainable metamaterials from natural resources for sound absorption applications. However, the challenge is the feasible production costs and manufacturability of the proposed metamaterials with desirable geometrical variations.*

➢ *Influence of variation of the cross-section of the perforation and perforation ratio on the sound absorption capability of MPP is not analyzed.*

➢ *Even though several researchers developed bio-degradable material for sound absorption applications, none developed MPP with different perforation cross-sections through 3D printing.*

➢ *There are no studies on the acoustic performance of samples with graded spherical perforations.*

➢ *Effect of wood/PLA material on acoustic properties has not been investigated so far.*

1.6   Motivation

Environmental concern leads to the development of bio-degradable materials for various applications. Most materials currently used for SA and STL applications, such as Glass wool and foams, are toxic and pose severe environmental and health issues. Natural biodegradable PLA and wood/PLA are eco-friendly, non-hazardous materials compared to synthetic materials. These materials can replace the synthetic ones where the strength of the material is least considered, such as vehicle dashboards, interiors, seat back, and building interiors. These materials have potential applications in the aerospace, automobile, power plant, and marine industries. This is because they have better out-of-plane stiffness, strength, and toughness properties, lower fabrication costs, and easier handling in production quality. Moreover, the varying cross-section and FG perforations may remarkably enhance the SA and STL characteristics. Such highly complicated geometries can be best obtained to the desired accuracy and finish using 3D printing techniques only. 3D printed PLA and wood/PLA offer high intricacy and aesthetics required for acoustic, architectural structures in buildings and other cited applications.

The pioneering work done by Maa (1987) on thin microperforated panels has been extended to thick panels having sufficient stiffness and strength, with micro-perforations by Sakagami et al. (2008). The impedance matching in perforations in thick panels can be done by employing perforations of varying cross-sections. These complicated profiles can be generated in the most intricate way using 3D printing techniques like FDM. Thus, apart from simple cylindrical perforations in thick panels, unconventional perforations can be used to get better acoustic performance. Another option for improving panels' performance could be by employing functionally graded perforations that can also be generated via 3D printing. Moreover, porous materials like wood will further add to the performance of bio-degradable materials like PLA, which

can be used for 3D printing above panels.

1.7   Objectives

From literature, it is observed that very less work has been carried out on the acoustic properties of 3D printed PLA and its blends. These materials can be used as alternatives for synthetic materials to a certain extent. So, it is important to find out the acoustic properties of these materials. The main objectives of the proposed research work are to

- Characterize acoustic properties of 3D printed MPP made of PLA with varying perforation cross-sections.
- Characterize acoustic properties of 3D printed spherical connected pores of uniform and graded perforations.
- Analyze the influence of wood fiber reinforcement on acoustic properties of 3D printed MPPs with varying cross-sections and graded perforations.
- Compare the experimental results with numerical results for SA and STL characteristics.

1.8   Thesis Outline

Chapter 1.   Provides an exhaustive literature survey on acoustics and 3D printing followed by the objective and scope of the work.

Chapter 2.   Describes the materials used and methodology followed for obtaining SA and STL characteristics.

Chapter 3.   Presents design, manufacture, acoustic testing, and numerical analysis of MPPs with varying cross-section perforations.

Chapter 4.   Covers conceptualization, manufacture, numerical analysis, and experimental validation of acoustic behaviour of functionally graded perforation specimens containing spheres connected in series.

Chapter 5.   Presents comparison studies on wood/PLA specimens of the same geometry with that of the best performing specimens made of PLA analyzed in chapters 3 and 4 is done.

Chapter 6.   Summary and conclusions of the entire work are presented.

2 MATERIALS AND METHODOLOGY

2.1 Materials

In the present work, PLA is used to prepare all the test samples. The PLA specimens are fabricated using filament prepared from PLA granules graded 3052D procured from Natureworks, LLC, USA. The granules are dried in an oven at 65°C for 8 hours to remove the moisture content. The average molecular weight of PLA is 1,16,000 g/mol, while the degradation temperature is 336.7°C and the other properties are given in Table 2.1.

Table 2.1: Technical specifications of PLA (Material data sheet)

Physical Property	Value
Specific gravity	1.24
Relative viscosity	3.3
Melting temperature (°C)	195 - 220
Glass transition temperature (°C)	45 - 60
MFR, g/10min (210°C, 2.16 kg)	14
Yield strength, Tensile (MPa)	62
Tensile elongation (%)	3.5
Vicat softening point (°C)	66.2 ± 1.4

2.1.1 PLA filament

PLA is obtained by ring polymerization or condensation polymerization of lactic acid ((Nam et al. 2003), (Nurul Fazita et al. 2016)). Lactic acid can be chemically synthesized with the hydrolysis of lacronitrile using strong acids or fermenting corn, potato, beets, and sugar ((Huda et al. 2008), (Porras et al. 2012)). The PLA granules are extruded at an extruding speed 9 rpm, take-up speed 10.5 rpm, resulting in a filament having a diameter 1.75 ± 0.05 mm to be used for FDM based 3D printing. An extruder 25SS/MF/26, length to diameter ratio of 25:1 manufactured by Aasabi India Ltd; is used for filament extrusion with a temperature set at four critical points in the barrel to die section as 160-165-170-155°C. Protocenter 999 (Aha 3D Innovations Pvt. Ltd., Jaipur,

India) is used for printing the specimens through FDM employing the slicer software Simplify 3D 4.1.2.
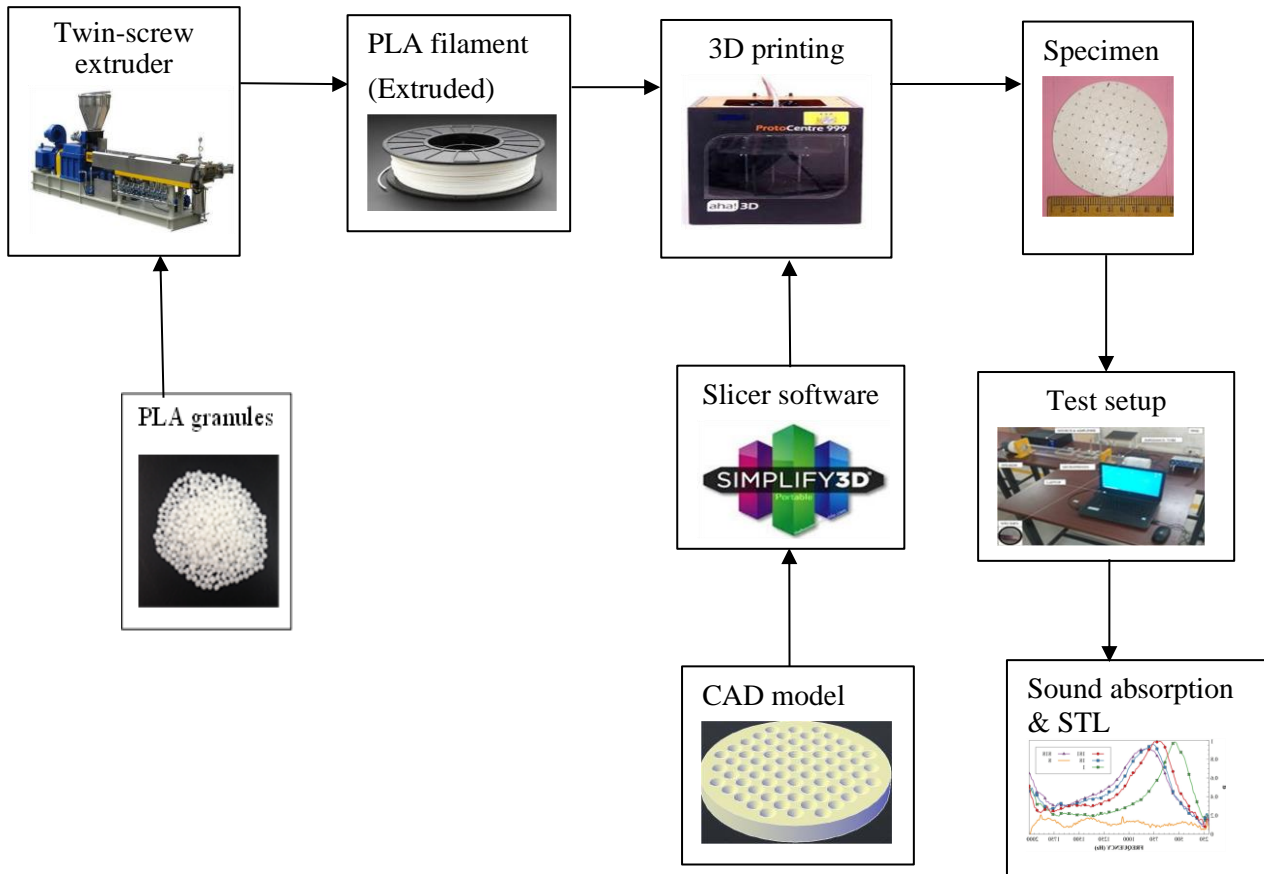
Figure 2.1: Schematic diagram of the proposed work based on PLA.

2.1.2 Wood-PLA filament

Wood filler reinforced PLA is also used to prepare specimens to study the effect of wood fiber addition on acoustic properties of samples fabricated using PLA alone. The mixture of 30% wood in PLA gave different behavior in the case of all specimens. Wood-PLA filament used for this study was procured from WOL3D India Ltd, Bengaluru, India. The procedure for the work using wood filament is shown in Figure 2.2. Ultimaker Extended 2+ 3D printer, manufactured by Ultimaker BV, Netherlands, is used for producing the specimens through FDM employing the slicer software Ultimaker Cura 4.8.

Table 2.2: 3D Wood/PLA filament specifications

Percentage of wood	30% by Wt
Diameter of filament	1.75 ± 0.05 mm
Weight	1 kg
Print temperature	180ºC - 230 ºC
Print bed temperature	20ºC - 60 ºC (Not compulsory)
Print surface	Kapton/Blue tape with glue stick
Nozzle size	> 0.5 mm
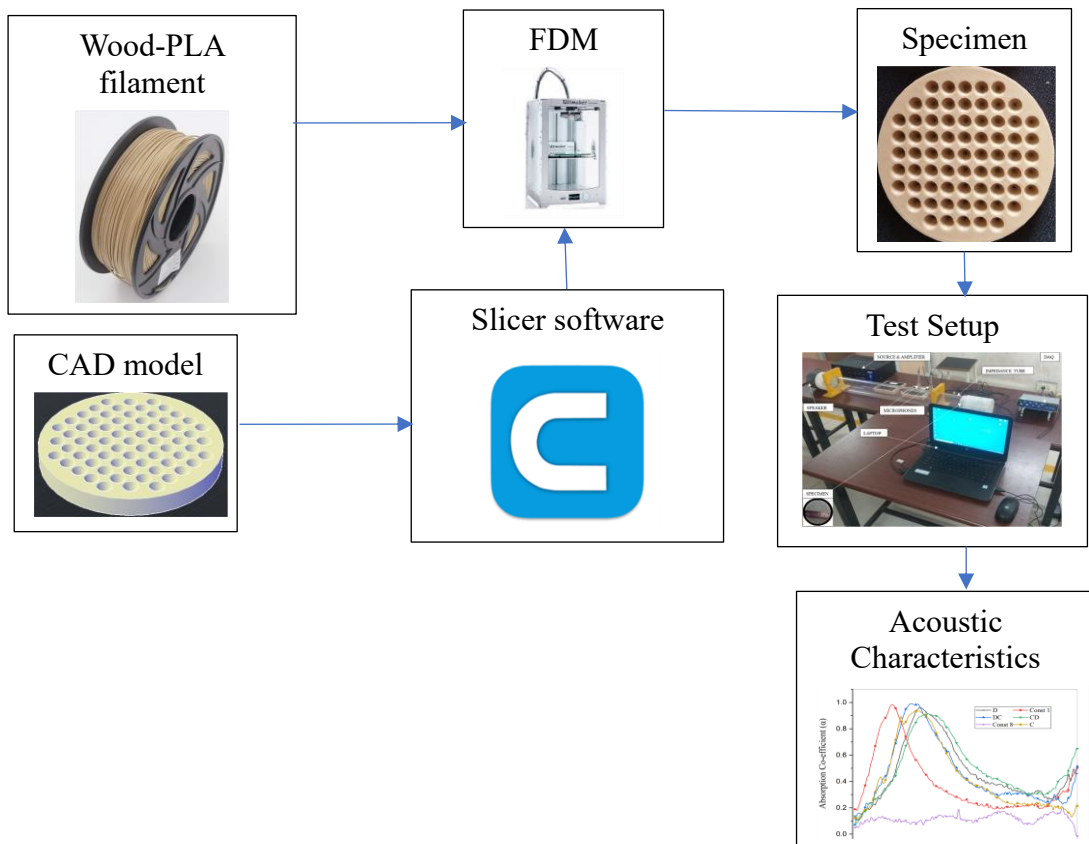
Figure 2.2: Flow diagram of the work using wood-PLA filament.

2.2 Experimental Details

MPPs with different non-uniform perforation cross-sections are tested for sound absorption and sound transmission loss characteristics in an impedance tube.
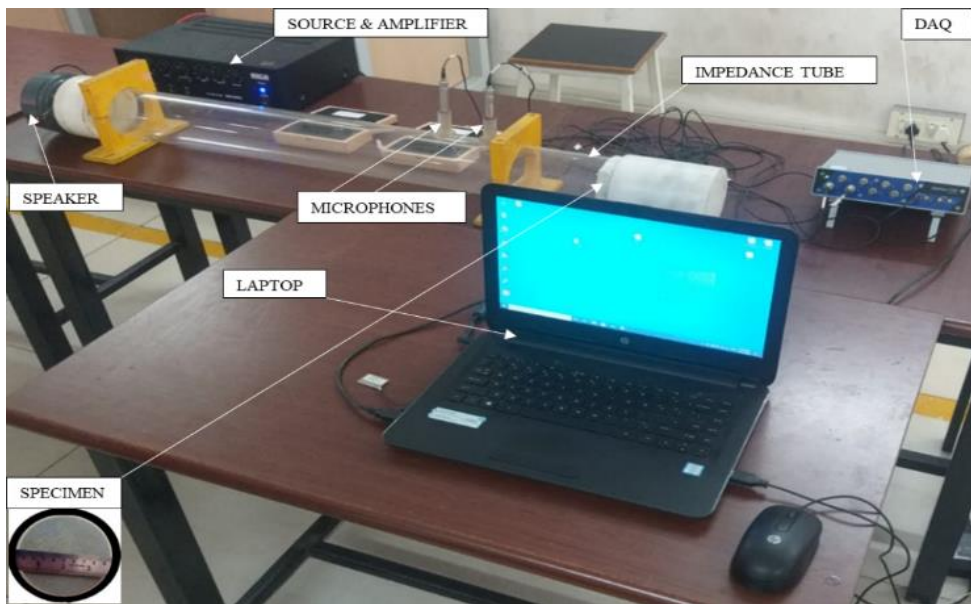
Figure 2.3: Impedance tube setup used for the experiments.

2.2.1 Sound absorption coefficient
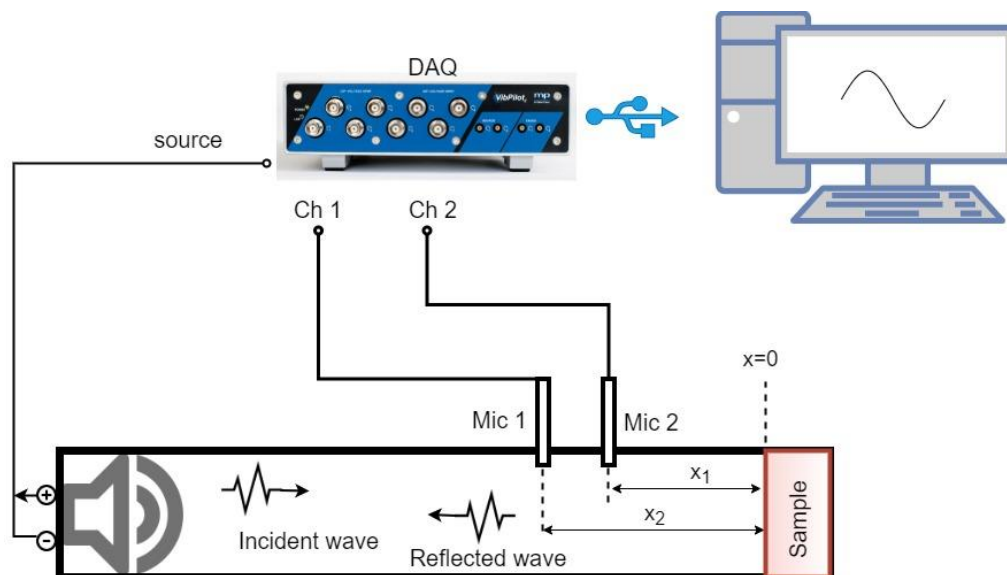
Figure 2.4: Schematic diagram of the experimental set-up used for sound absorption.

As per ASTM E1050-19, a two-microphone impedance tube is used to measure the sound absorption coefficient of the different MPPs in a frequency range of 200-2000 Hz (Figure 2.4). Three samples of circular sections with a diameter of 96 mm for each category are used for this test. The white noise generated from the source channel is fed to a 16Ω speaker fitted at one end of the tube through a power amplifier (90W RMS$_{max}$, 65W RMS at 10% THD, 60W RMS at 5% THD). Two 1/2" Microtech Gefell, random incidence type microphone, connected to M+P Vibpilot DAQ (8-channel with two source output made by Microtech Gefell GmbH., Germany) is used to measure the incident and reflected sound pressures. Using an M+P spectrum analyzer, the extracted time-domain signal is imported to MATLAB R2010a for computing the transfer function between two microphone pressure values. The wavenumber corresponding to a frequency is given by,

$$\text{Wavenumber (k)} = \frac{2\pi f}{c_0} \tag{2.1}$$

where f is the frequency and c_0 is the speed of sound. Similarly, the acoustic transfer function is given by,

$$(\text{H}_{12}) = \frac{p_2}{p_1} = \frac{e^{jkx_2} + re^{-jkx_2}}{e^{jkx_1} + re^{-jkx_1}} \tag{2.2}$$

where (H$_{12}$) is the acoustic transfer function, p_1 and p_2 are the measured acoustic pressure of the two microphones, and x_1 and x_2 are the distances between the reference plane (sample position of $x = 0$) and the two microphones, respectively. The reflection coefficient is calculated using,

$$\text{R} = \frac{e^{-jkS} - H_{12}}{H_{12} - e^{jkS}} \times e^{2jk(l+S)} \tag{2.3}$$

where R is the reflection coefficient, $S = x_2 - x_1$ is the distance between microphone positions, and l is the minimum distance between the microphone and sample. Sound absorption coefficient α is given by,

$$\alpha = 1 - |\text{R}|^2 \tag{2.4}$$

2.2.2 Sound transmission loss

According to ASTM E 2611-09, four microphone impedance tube tests are carried out to quantify sound transmission loss of the panel. The schematic diagram of the

experimental set-up for STL measurement and the position of microphones x_1, x_2, x_3 and x_4 from the sample is presented in Figure 2.5. The MPP is fixed between the upstream (reflection side) and downstream (transmission side) sections. White noise excitation is given by a loudspeaker attached to the left side of the tube, which leads to
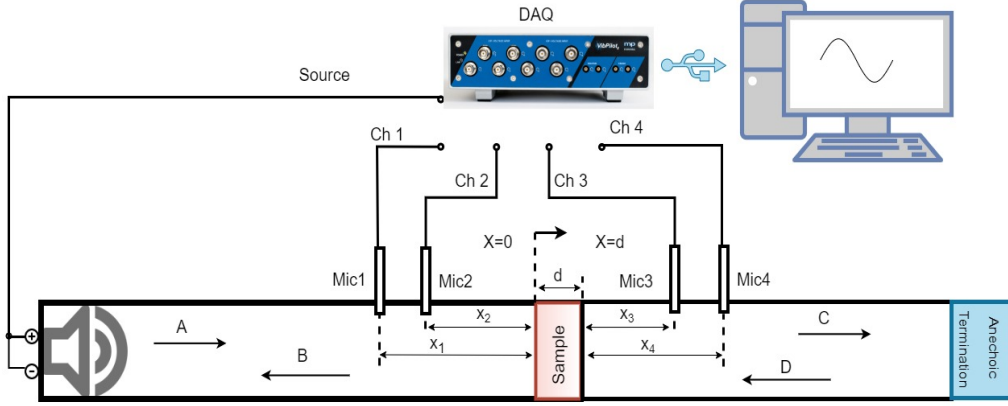
Figure 2.5: Experimental set-up for STL measurement using impedance tube.

plane wave condition inside the tube, and the other side of the tube has anechoic material with a rigid cap. Using microphones, the complex sound pressures (a combination of waves travel in the positive and negative direction both upstream and downstream) P_1 to P_4 measured at the different position x_1 to x_4 are given as,

$$P_1 = \left(Ae^{-jkx_1} + Be^{jkx_1}\right)e^{j\omega t} \tag{2.5}$$

$$P_2 = \left(Ae^{-jkx_2} + Be^{jkx_2}\right)e^{j\omega t} \tag{2.6}$$

$$P_3 = \left(Ce^{-jkx_3} + De^{jkx_3}\right)e^{j\omega t} \tag{2.7}$$

$$P_4 = \left(Ce^{-jkx_4} + De^{jkx_4}\right)e^{j\omega t} \tag{2.8}$$

Z_0 is the characteristic impedance defined as $Z_0 = \rho_0 c$, and ρ_0 is the density of air. The amplitudes of complex sound pressure of generated plane waves are given by

$$A = \frac{j(P_1 e^{jkx_2} - P_2 e^{jkx_1})}{2\sin k(x_1 - x_2)} \tag{2.9}$$

$$B = \frac{j(P_2 e^{-jkx_1} - P_1 e^{-jkx_2})}{2\sin k(x_1 - x_2)} \tag{2.10}$$

$$C = \frac{j(P_3 e^{jkx_4} - P_4 e^{jkx_3})}{2\sin k(x_3 - x_4)} \tag{2.11}$$

20

$$D = \frac{j(P_4 e^{-jkx_3} - P_3 e^{-jkx_4})}{2 \sin k(x_3 - x_4)} \tag{2.12}$$

Assuming, the sound wave travels on the x-axis, the complex pressure $p(x,t)$ and corresponding particle velocity $v(x,t)$ in the reflection, medium and transmitted medium is given by,

$$p(x,t)|_{x=0} = A e^{i(\omega t - kx)} + B e^{i(\omega t + kx)} \tag{2.13}$$

$$v(x,t)|_{x=0} = \frac{1}{Z_0}\left[A e^{i(\omega t - kx)} - B e^{i(\omega t + kx)}\right] \tag{2.14}$$

$$p(x,t)|_{x=d} = C e^{i(\omega t - kx)} + D e^{i(\omega t + kx)} \tag{2.15}$$

$$v(x,t)|_{x=d} = \frac{1}{Z_0}\left[C e^{i(\omega t - kx)} - D e^{i(\omega t + kx)}\right] \tag{2.16}$$

where t is the time, A and B are the amplitude of incident and reflected waves in the tube in front of the sample. Likewise, C and D are the amplitude of transmitted and reflected waves on the other side of the sample. For one-dimensional wave propagation, the relationship between acoustic pressure and particle velocity on both sides of the tube arrived by transfer matrix [T] is given by,

$$\begin{bmatrix} p_{x=0} \\ v_{x=0} \end{bmatrix} = \begin{bmatrix} T_{11} & T_{12} \\ T_{21} & T_{22} \end{bmatrix} \begin{bmatrix} p_{x=d} \\ v_{x=d} \end{bmatrix} \tag{2.17}$$

The time dependency in the equation is assumed to be neglected. The acoustic pressure and particle velocity on both sides of the MPP of thickness d are expressed as,

$$p\,|_{x=0} = A + B \tag{2.18}$$

$$v\,|_{x=0} = \frac{1}{Z_0}[A - B] \tag{2.19}$$

$$p\,|_{x=d} = C e^{-jkd} + D e^{jkd} \tag{2.20}$$

$$v\,|_{x=d} = \frac{1}{Z_0}\left[C e^{-jkd} + D e^{jkd}\right] \tag{2.21}$$

There is a minimal reflection downstream in the case of anechoic end termination. So, D can be assumed as negligible as compared to C. The acoustic pressure and particle velocity on both sides of the panel become,

$$p\,|_{x=0} = 1 + R \tag{2.22}$$

$$v\,|_{x=0} = \frac{1}{Z_0}[1 - R] \tag{2.23}$$

$$p\,|_{x=d} = T e^{-jkd} \tag{2.24}$$

$$v \mid_{x=d} = \frac{1}{Z_0} \left[Te^{-jkd} \right] \qquad (2.25)$$

where R=*B/A* is the plane wave reflection coefficient, and *T=C/A* is the plane wave transmission coefficient. When Equations 2.18 to 2.21 is replaced with Equations 2.13 to 2.16, the normal incident pressure transmission τ for an anechoic termination is given as,

$$\tau = \frac{2e^{jkd}}{T_{11} + (T_{12}/Z_0) + Z_0 T_{21} + T_{22}} \qquad (2.26)$$

Normal sound incident sound transmission loss is given by,

$$STL = 10 \, \log \frac{1}{|\tau|^2} \qquad (2.27)$$
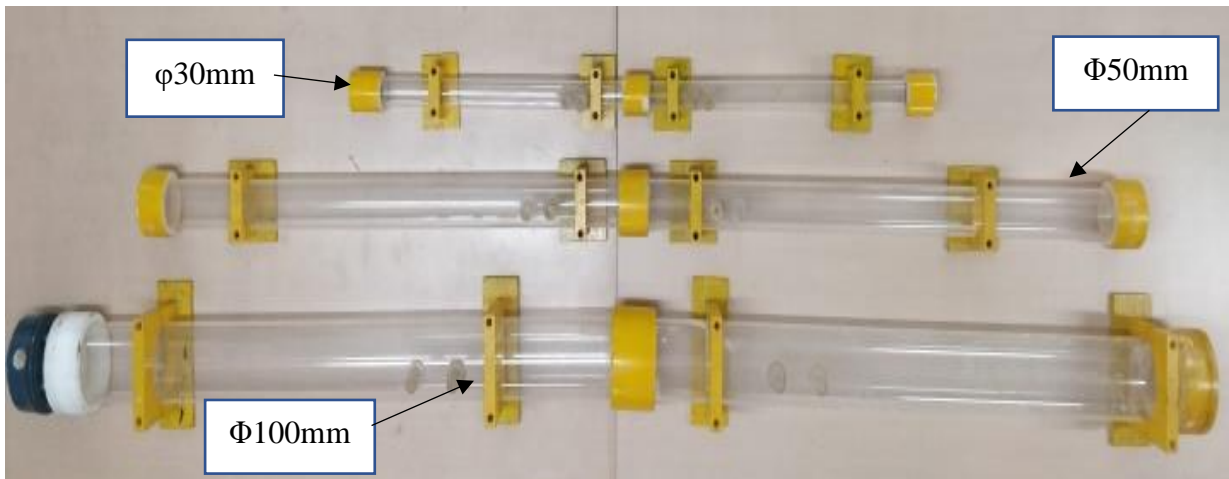
Figure 2.6: Assembly of tubes for STL measurement using impedance tube
(Diameters 30mm, 50mm, 100 mm).

2.3   Numerical analysis

Numerical analysis is performed using COMSOL Multiphysics 5.4 to evaluate sound absorption and transmission loss, and then the corresponding results are compared with experimental results. COMSOL pressure acoustics module, which is suited for plane wave simulation, is used. For a simplified approach, the model represents only the air volume occupied in the system, eliminating fluid-structure interaction and reducing resources and computational time usage. A 3D CAD file modelled with three domains, namely perfectly matched layer (PML), incident pressure field, and MPP is considered for sound absorption simulation. Additionally, two more parts, the transmitted pressure

field, and PML are modelled for sound transmission loss analysis. Further, the models are imported to the geometry section in a suitable format using CAD kernel. PML domain was used to absorb all the energy which came inside, and it won't reflect the waves from all non-PML domains. Hence, the PML is added to the end of pressure fields to activate the non-reflecting acoustic domain. Sound hard boundary wall condition is applied to all boundaries of the finite element model. Background pressure of 1 Pa is applied in the pressure field domain, and model material is assigned as air imported from the in-built library. The user-controlled mesh is defined in the model. The hexahedron element is mapped for the PML. The rest of the entire domain is meshed with free Tetrahedron elements. Finite element mesh size is chosen based on the requirement of six elements per wavelength corresponding to the highest frequency analyzed (Jones 2010). The wavelength corresponding to the highest frequency is calculated as given by,

$$\lambda_{min} = C_0/f_{max} \tag{2.28}$$

where C_0 is the speed of sound and f_{max} is the maximum frequency in the model.

The numerical model used to analyze sound absorption consists of two air domains corresponding to the incident region and the air gap behind MPP. However, the numerical model used to analyze sound transmission loss has added one more air domain to represent the transmission region. In both cases, the elements in the air domain are modelled using an acoustic pressure module. The air domain occupied inside the perforated hole is a narrow acoustic region. Hence, the corresponding region is modelled using a thermos-viscous acoustic module for accounting for viscous and thermal losses. Using the Multiphysics coupling option available in COMSOL (Zhang et al. 2015), a thermo-viscous physics interface with pressure acoustic physics is specified. After solving the problem, incident pressure (P_i) and reflected pressure (P_r) values are obtained in post-processing. Using these pressure values, the reflection coefficient, R=P_r/P_i, and absorption coefficient, $\alpha = 1 - |R|^2$. Values are estimated. Subsequently, STL is obtained by,

$$STL = 10 \log\left\{\frac{Wi}{Wo}\right\} \tag{2.29}$$

Wi is the input sound power, and Wo is the output sound power over the inlet and outlet port surfaces. Details of the calculations are given in Appendix-I.

3   PANELS WITH VARYING CROSS-SECTION PERFORATIONS

3.1   Design of MPPs with varying cross-section The influence of variation of perforation cross-section on sound absorption and transmission loss characteristics of typical MPP is presented in this chapter. Geometric parameters of MPP like perforation diameter and inter hole distance are calculated according to the procedure (Maa 1987), and the same is briefed here. Let,

ω_0 = Resonant angular frequency (rad/s)

R = Resistive term of specific acoustic impedance (Pa.s/m)

D = Air gap width between panel and wall (mm)

f_0 = Resonant frequency (Hz)

m = M_1/cρ where,

M_1 = Mass term of specific acoustic impedance (Pa.s/m)

c = Velocity of sound in air (340 m/s) at 15°C and one atmospheric pressure

ρ = Density of air (1.225 kg/m^3) at 15°C and one atmospheric pressure

- According to Maa and also reported by several researchers (Sakagami et al. 2008), (Chin et al. 2018) (Liu et al. 2014), (Jiang et al. 2020), the MPPs work well in the frequency range of 0 - 4 kHz, i.e., the range of hazardous frequency to humans. Based on this, most of the MPPs are designed with the resonant frequency of $f_0 = $ 2 kHz. Furthermore, Maa used exact equations to obtain dimensional parameters of MPP, such as least diameter d of tapered holes and inter hole distance b.

- Air gap width, D, was determined from (Dω_0/c) =1 as 27.05 mm. A smaller value of (Dω_0/c) will give a narrower absorption band.

- Determined the resonant frequency and ratio of panel thickness to perforation ratio using the equation $\omega_0 m \simeq 4\frac{f_0 t}{p}$. t is the thickness of the panel, which was 10 mm. and m = M_1/cρ, where M_1 = Mass term of specific acoustic impedance.

- The diameter of the hole was found from the equation (R/cρ) = 0.2t /pd^2, where p = perforation ratio was 0.01. Selected the diameter of the hole as 1mm among the choices obtained.

25

- Using the formula for perforation ratio, $p = 78 \, d^2/b^2$, we can find the hole-to-hole center distance, b, which was obtained as 8.86 mm. Further, rounding this value to 10 mm is done for ease of fabrication.
- Choose the values of D, t, b, and p to meet fabrication requirements since all values obtained by the procedure are approximate.

From the range of hole diameter of 0.1-1mm for good performance as given by Maa, the size was selected as 1mm taking into account the ease of printing with high accuracy. Also, the approximate center to center distance of holes was calculated as 8.86 mm, which was rounded off to 10 mm. The standard diameter of the specimen is 96 mm with a thickness of 10 mm for a low-frequency impedance tube. An acoustic test is carried out on five samples each for all the perforation cross-section variations and 3D printed specimens with details shown in Figure 3.1.

The distance between two holes is 10 mm (maximum hole diameter + 2 mm). Five perforation geometries were chosen for the study. Constant diameters 1 and 8 mm each. Convergent-divergent type perforation has maximum and minimum diameters of 8 and 1 mm (at half the thickness of the specimen). Divergent-convergent type perforation with minimum and maximum diameter, 1mm and 8mm (at half the thickness of the specimen). Divergent type of perforation with a maximum and minimum diameter of 8 and 1 mm, respectively, throughout the specimen's thickness, can be tested from the other end to get convergent geometry data. Five different geometries were chosen with cross-sections varying from 8 to 1 mm in diameter to study the effect of air column convergence, divergence, and enclosure on thermal and viscous dissipations of incident sound energy. Two specimens were kept with a constant hole diameter of 1 mm and 8 mm, respectively, as a standard of comparison to the varying cross-sections. The five specimens, each of 96 mm diameter, 10 mm thickness, and perforation diameter of 1 mm and 8 mm, respectively, are drawn in AUTOCAD 2019. The file is converted into a .stl form. G-codes are generated using a slicer software SIMPLIFY 3D 4.1.2 and are further used to print all the cross-sectional variations.

3.2   Preparation of 3D Model

The five models, each of 96 mm diameter, 10 mm thickness, and hole diameter of 1mm and 8 mm, respectively, were drawn in AUTOCAD, which offers more flexibility for both 3D and 2D drawings than other solid modelling packages CREO, SOLIDWORKS and SOLIDEDGE. The file was converted into standard *stl* format and loaded into a slicer software SIMPLIFY 3D for preparing g-code to 3D print the model. The slicer software slices the solid into multiple layers of definite thickness and gives the printing simulation wherein we can check the correctness of the process and refine the printing procedure.

3.3   Printing of the specimen

The specimen is then printed using a printer PROTOCENTER 999 available at the advanced manufacturing laboratory of NITK Surathkal, India. The standard printing parameters of PLA used are extrusion temperature of 210°C, the printing speed of 1440 m/min, and bed temperature of 60°C. The ABS paste as the bottom layer and the required environmental conditions like the ambient temperature of 20°C were followed to get the best surface finish and dimensional accuracy during the printing procedure. The skirt and raft layers were removed using a polishing machine. The finish and dimensional accuracy obtained using PLA were excellent, as expected.

3.4   Experimental details

MPPs with different perforation cross-sections are tested for sound absorption and sound transmission loss characteristics in an impedance tube, as mentioned in Section 2.3.

3.4.1   Sound absorption coefficient

As per ASTM E1050-19, a two-microphone impedance tube is used to measure the sound absorption coefficient of the different MPPs in a frequency range of 200-2000 Hz (Figure2.3). Three trials are carried out for samples of circular sections with a diameter of 96 mm for each category for this test. The white noise generated from the source channel is fed to a 16Ω speaker fitted at one end of the tube through a power amplifier (90W RMS$_{max}$, 65W RMS at 10% THD, 60W RMS at 5% THD). Two 1/2"
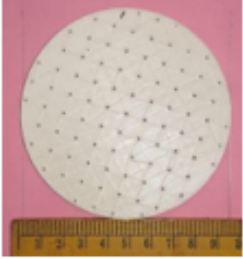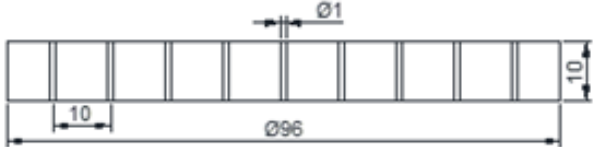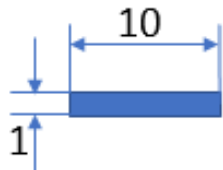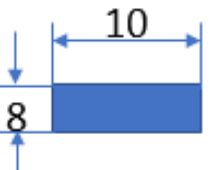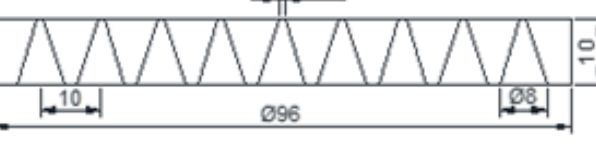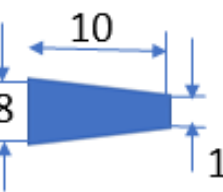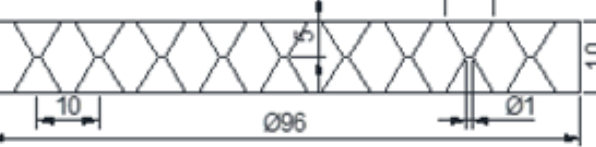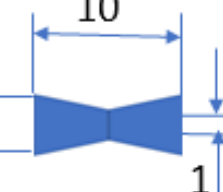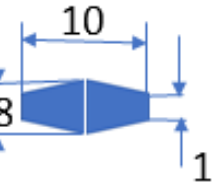
Figure 3.1: Perforation geometry and actual specimen with dimensions.

Microtech Gefell, random incidence type microphone, connected to M+P Vibpilot DAQ is used to measure the incident and reflected sound pressures. Using an M+P spectrum analyzer, the extracted time-domain signal is imported to MATLAB R2010a for computing the transfer function between two microphone pressure values. The reflection coefficient and sound absorption coefficient are calculated successively, as mentioned in Section 2.3.1.

3.4.2 Sound transmission loss

According to ASTM E 2611-09, four microphone impedance tube tests are carried out to quantify sound transmission loss of the panel. The schematic diagram of the experimental set-up for STL measurement and the position of microphones x_1, x_2, x_3 and x_4 from the sample is presented in Figure 2.4. The MPP sample is fixed between the upstream (reflection side) and downstream (transmission side) sections. White noise excitation is given by a loudspeaker attached to the left side of the tube, which leads to plane wave condition inside the tube, and the other side of the tube has anechoic material with a rigid cap. Using microphones, the complex sound pressures (a combination of waves travel in the positive and negative direction both upstream and downstream) P_1 to P_4 are measured at the different positions $x_1 \ to \ x_4$. Normal sound incident sound transmission loss is calculated as in Section 2.3.2.

3.5   Numerical analysis

Numerical analysis is performed using COMSOL Multiphysics to evaluate sound absorption and transmission loss, and then the corresponding results are compared with experimental results. COMSOL pressure acoustics module, which is suited for plane wave simulation, is used. For a simplified approach, the model only represents the air volume occupied in the system, eliminating fluid-structure interaction and lowering resources and computational time usage. A 3D CAD file modelled with three domains, namely perfectly matched layer (PML), incident pressure field, and MPP is considered for sound absorption simulation. Additionally, two more domains, the transmitted pressure field and PML, are modelled for sound transmission loss analysis.

Further, the models are imported to the geometry section in a suitable format using CAD kernel. PML domain was used to absorb all the energy which came inside, and it won't reflect the waves from all non-PML domains. Hence, the PML is added to the end of pressure fields to activate the non-reflecting acoustic domain. Sound hard boundary wall condition is applied to all boundaries of the finite element model. Background pressure of 1 Pa is applied in the pressure field domain, and model material is assigned as air imported from the in-built library. The user-controlled mesh is defined in the model. The hexahedron element is mapped for the PML. The rest of the entire domain is meshed with free Tetrahedron elements, and the meshed model with varying cross-section samples is presented in Figure 3.2. Finite element mesh size is chosen based on the requirement of six elements per wavelength corresponding to the highest frequency analyzed (Jones 2010). The wavelength corresponding to the highest frequency is calculated as given by,

$$\lambda_{min} = C_0/f_{max} \tag{3.1}$$

where C_0 is the speed of sound and f_{max} is the maximum frequency in the model. The acoustic wave propagation in homogeneous fluid media is governed by,

$$\nabla^2 P = \frac{1}{c_0^2} \frac{\partial^2 P}{\partial t^2} \tag{3.2}$$

where P is the sound pressure of the acoustic field and t is the time.
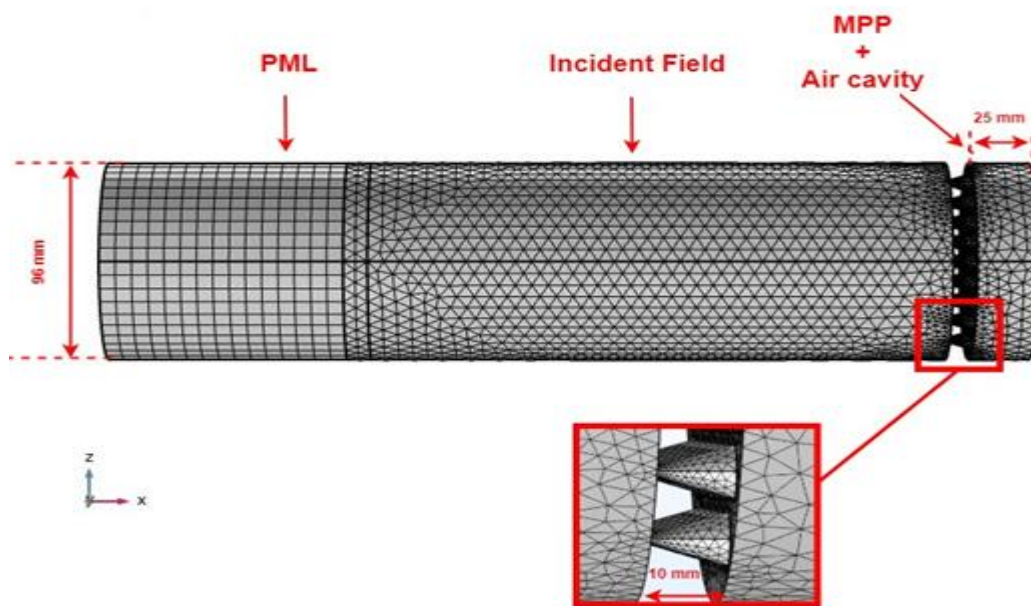
Figure 3.2: Numerical model for varying cross-section sample 'D'.

3.6   Results and discussion

3.6.1   Sound absorption coefficient

The influence of perforation cross-section variation on sound absorption coefficient obtained through the experiment is depicted in Figure 3.3. It is observed that the influence of the perforation pattern on the sound absorption coefficient is significant. The coefficient of the sample with 8 mm constant diameter perforation is significantly lower than the perforation variations. Wide perforations transmit sound energy uninterruptedly due to wider air column, which reduces the friction and viscous dissipation effects. Sub-millimeter holes act as good absorbers since they pose better resistance (Maa 1987). However, the maximum sound absorption coefficient in the range of 0.9 to 0.99 is observed for the other cases. Even though there is no perforation diameter variation for the Const 1 sample, its coefficient is very high compared to the Const 8 sample due to dense, viscous boundary layer formation inside, enhancing the solid-fluid friction and viscous dissipation.

It is also very interesting to note that the samples with perforations of varying cross-sections such as DC, CD, D, and C have better sound absorption coefficient over a wider frequency range than Const 1 sample (Table 3.1). It is also observed that an increase in the frequency band is associated with a slightly reduced SA co-efficient. A sharp peak with a narrow band is observed for Const 1 sample, while a reduced peak with a wider band is noted for the CD sample. Similar variation in peak and frequency band can be observed for C, D, and DC samples. Peak values of SA coefficient of different samples is observed to be declining (DC > Const 1 > D > C > CD > Const 8) and bandwidth is observed as CD > C > D > DC > Const1 for an absorption coefficient $\alpha > 0.75$ as noted from Table 3.1.
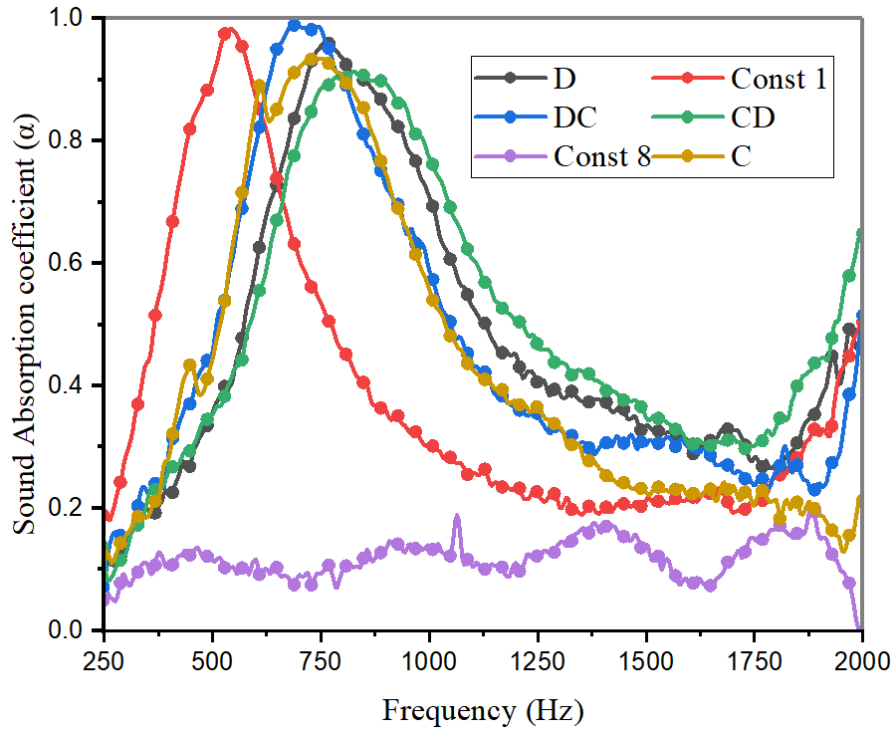
Figure 3.3: Influence of perforation cross-section on sound absorption coefficient.

Table 3.1: Influence of varying cross-section on peak value and bandwidth of SA coefficient.

Sl.No.	Specimen	Frequency bandwidth for SA co-efficient, $\alpha > 0.75$ (± 1 Hz)	The maximum value of SA co-efficient (α_{max}) obtained (for 250-2000 Hz)
1	Const 1	215	0.98333
2	DC	300	0.99025
3	D	320	0.96246
4	CD	345	0.91396
5	C	325	0.93554
6	Const 8	0	0.20630

3.6.2 Sound transmission loss

The influence of perforation cross-section variation on sound transmission loss is shown in Figure 3.4. From Figure 3.4, it is observed that the influence of perforation cross-sectional variations on the sound transmission loss is significant. The sound

transmission loss of the sample with 8 mm constant diameter perforation is much less than the other samples. However, transmission loss seems to increase with frequency from 250 to 2000 Hz for the other cases. Even though there is no perforation diameter variation for Const 1 sample, its sound transmission loss is much higher than the Const 8 sample due to the formation of a viscous boundary layer with closer flux lines with high velocity gradient which enhances dissipation.
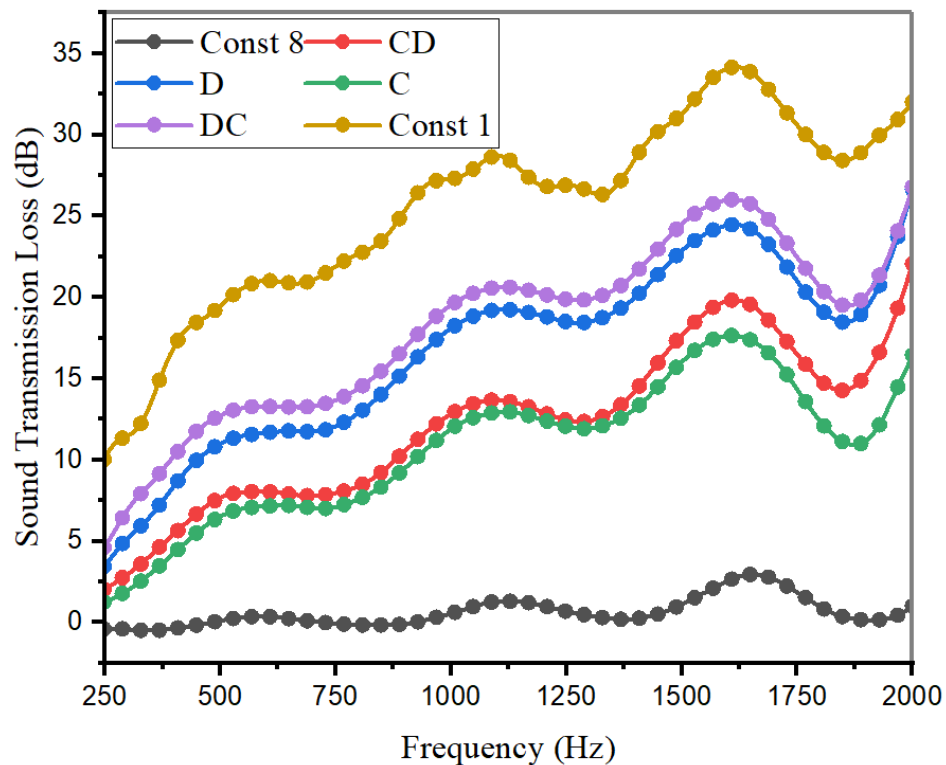
Figure 3.4: Influence of perforation cross-section on sound transmission loss.

It is also very interesting to note that the samples with perforations of varying cross-sections such as DC, CD, D, and C have remarkable sound transmission loss over a frequency range comparable to Const 1. It is also observed that the increase in sound transmission loss is associated with an increase in frequency up to 2000 Hz. Sound wave energy dissipation is increasing in proportion to frequency. Increase of STL of different samples is observed to be decreasing in the order of Const 1 > DC > D > CD > C > Const 8 as seen from Figure 3.4. The sound transmission loss of an MPP is influenced by the porosity and dissipation amount of acoustic energy while traveling through the perforation channel. From the present analysis, it is clear that the

33

perforation cross-section variation significantly affects the acoustic energy dissipation of MPPs.

Sample	Slice (m/s)	Stream line
D		
Const1		
DC		
C		
CONST 8		
CD		
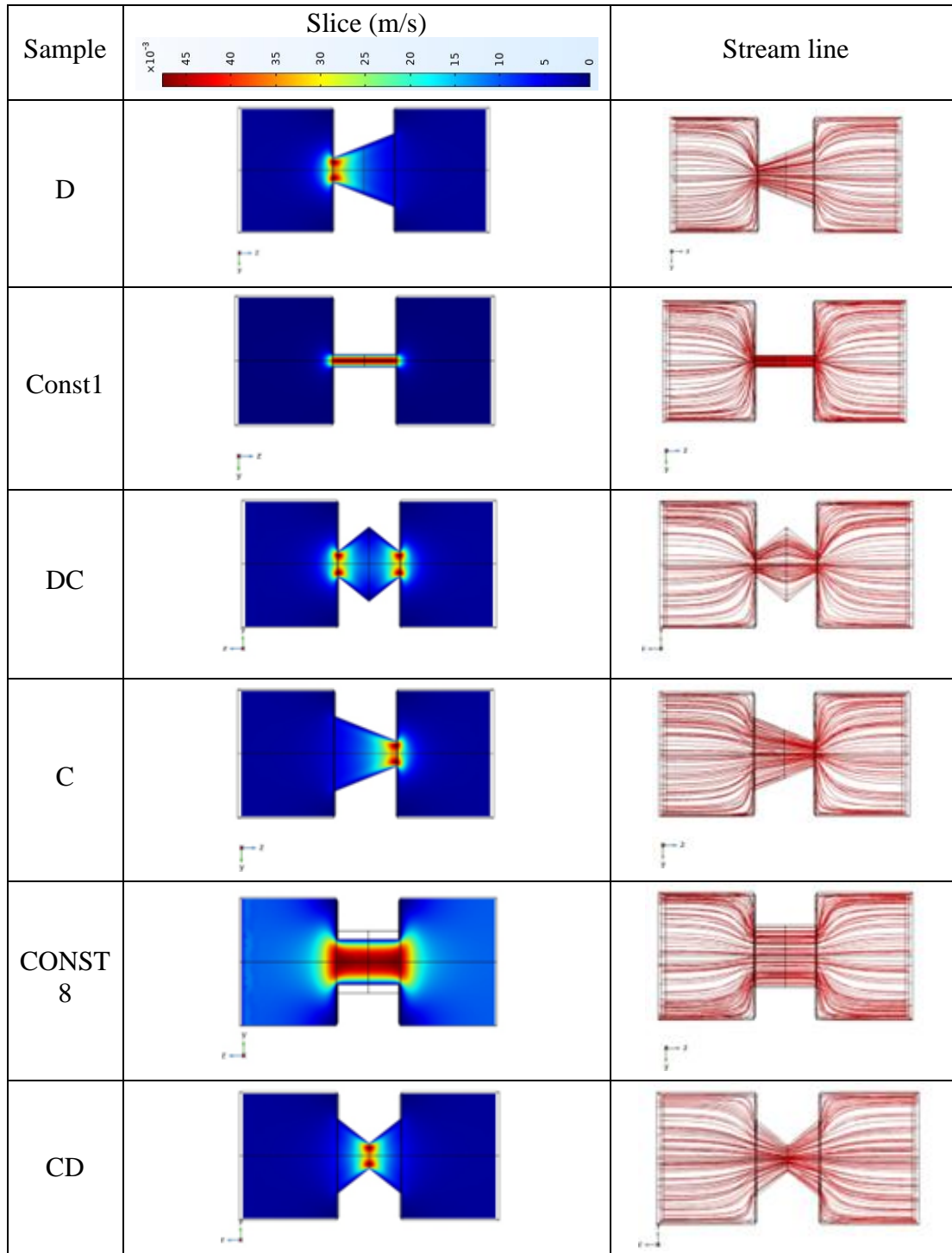
Figure 3.5: Viscous boundary layer formation inside the perforations.

From Figure 3.4, two different trends in the variation of sound transmission loss with respect to cross-sectional geometry are noted. The viscous boundary layer formed at the perforations is shown in Figure 3.5. Resonance and viscosity account for most dissipation (nearly 85%), whereas friction, thermal and inertial losses account for the rest of the dissipation. Also, higher viscosity promotes higher resonance losses.

The thicker and denser boundary layer with a longer length may cause higher dissipation in each case. Here the bends, expansion, and contraction cause scattering and tortuosity. The longer tortuous path will also give higher dissipation. These factors must be accounted for in making predictions, especially in practical studies. Divergent sections exhibit better energy dissipation compared to the converging pattern. DC section shows the best performance amongst the varying cross-section perforations. This section has the best dissipative capacity with two small perforations and thick boundary layers at entry and exit. Furthermore, enclosed air column acts as better sound energy dissipators, dissipating the pulsating sound waves. The Const 1 perforation shows the highest dissipation due to the thickest boundary layer formation inside a narrow path.

Although the MPPs are good absorbers, the transmission loss at mid frequencies is lower. Hence dissipation of human voices, which usually falls in this frequency range, is lower. This is due to the good surface finish of the perforations, which may degrade with usage for long periods. STL can be further enhanced by reducing the perforation diameter and increasing sound flux density inside the sub-millimeter perforations. The diverging sections gave comparatively better sound transmission loss than converging ones, with a significant margin of 5 dB at almost all frequencies. Thus, even though all the above specimens are good absorbers and can be used to effectively reduce sound reflection, sub-millimeter holes of constant diameter exhibit the highest transmission loss. Reducing diameter variations or introducing multiple steps might effectively enhance sound transmission loss due to the boundary layer thickening effect.

3.6.3   Comparison of experimental and numerical results

The sample with an 8 mm diameter hole was an inferior absorber (Maa 1987) and, hence, was not considered for numerical analysis. The FEM simulations are in good agreement for all the cross-sectional variations of perforations (Figure 3.6,3.7). A comparison has been made for other cases also. Resonant frequencies match closely for all the cases. The bandwidths are also closer to the absorption coefficient of 0.2 at medium frequencies. However, the experimental values are higher at very low and higher frequencies. This may be due to the violation of the assumptions of perfect rigidity of the wall and surface smoothness. Practically rough and non-rigid surfaces
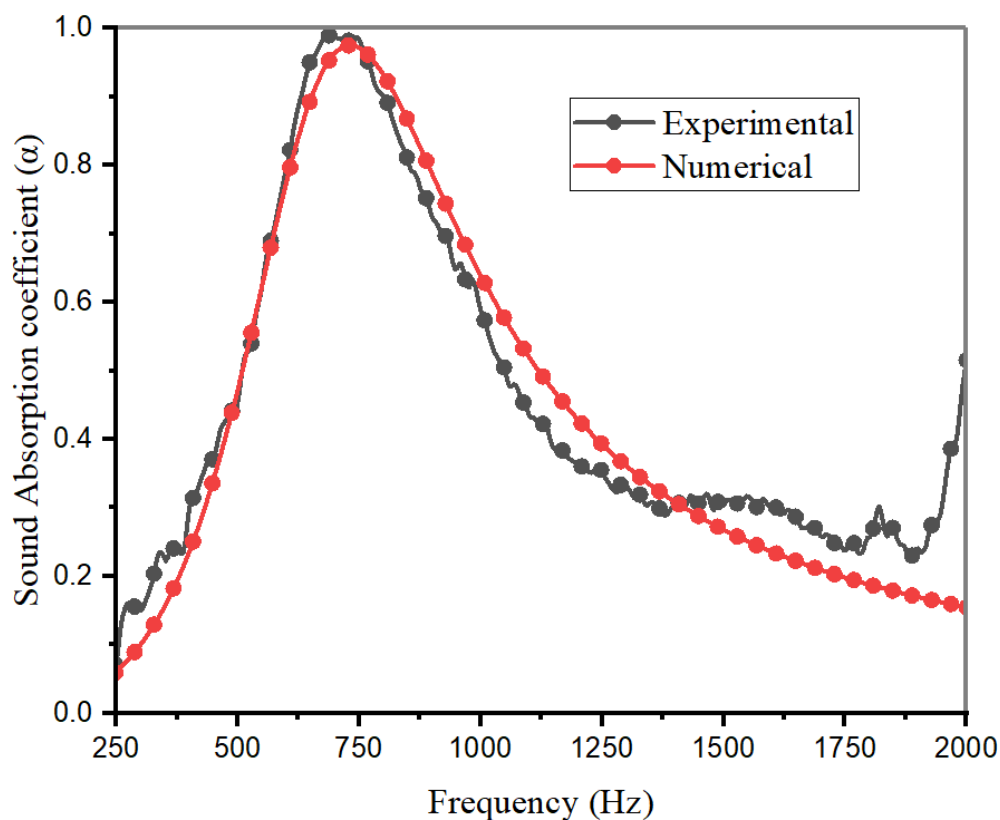

Figure 3.6: Numerical and experimental values plotted for DC perforation specimen.
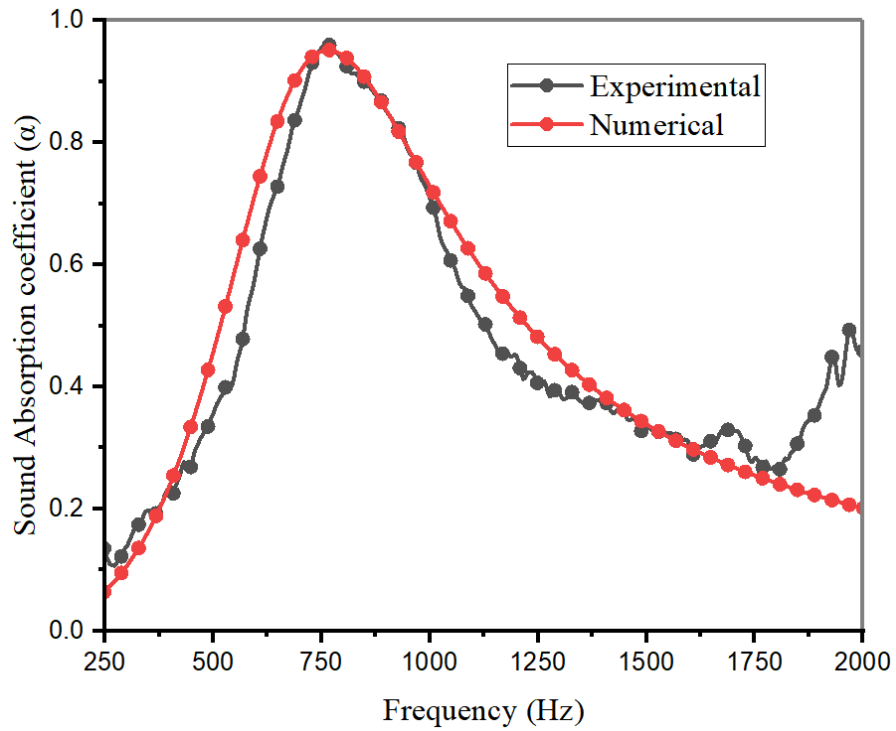
Figure 3.7: Numerical and experimental values plotted for D perforation specimen.
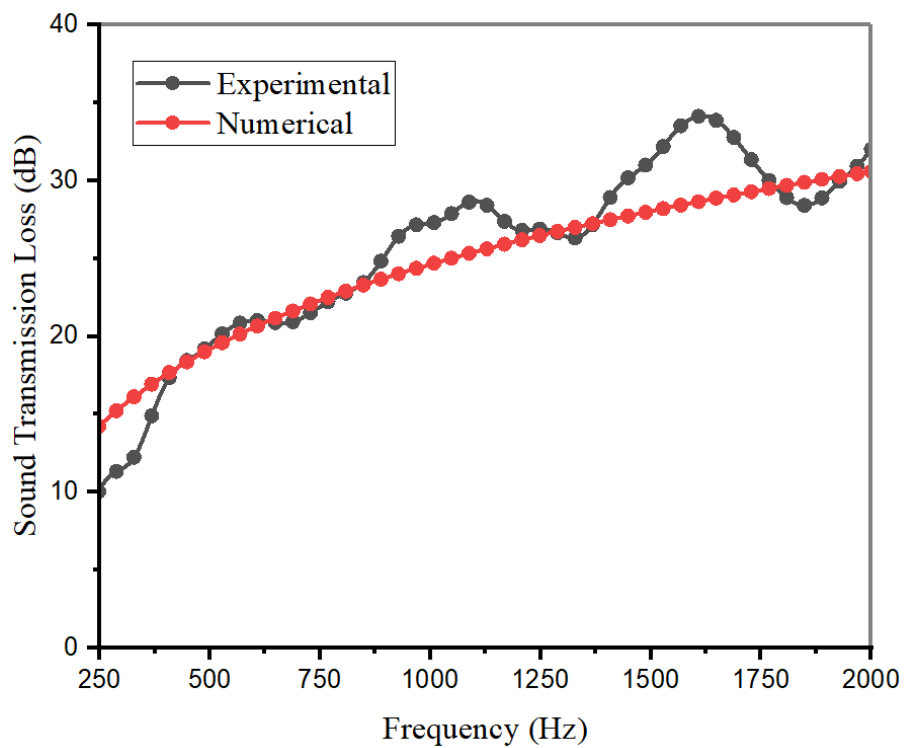
Figure 3.8: Sound transmission loss versus frequency - numerical and experimental curves for Const 1 perforation specimen.

enhance visco-thermal losses increasing absorptivity. Nonetheless, the PLA specimen did not show many deviations due to good surface finish, dimensional accuracy, and defect-less layered deposition in printing due to optimized printing parameters. The STL values obtained from numerical analysis are in close agreement with experimental values for Const 1 specimen (Figure 3.8). Such plots obtained from numerical analysis help achieve the performance characteristics before printing, leading to much lower lead times and satisfying the industrial demands in a much more effective way.

3.7   Conclusion

Geometrical variations of perforations influence the dissipation of sound (absorption coefficient and frequency bandwidth). From the sound absorption coefficient results as presented in this work, it is found that the DC perforation registered better performance compared to the constant 1 mm diameter perforation pertaining to both peak absorption coefficient and bandwidth. All other perforations depicted less peak absorption coefficient amid comparable values for a constant diameter of 1 mm. The bandwidths covered by all different perforations for a given range of absorption coefficients were higher than Const 1. Sound transmission losses are comparable to Const 1, especially where the entry point of perforation is small.

All other perforations show significantly higher sound transmission loss than Const 8, which increases with frequency. Const 1, DC, and D have very low transmission of sound. Const 1 mm perforation was maximum due to the dominant effect of friction at the narrow solid-air interface and a lengthy, narrow fluid column. The MPPs studied are excellent in sound absorption and have reasonably good dissipating power during sound transmission. Thus CD, DC, and tapered perforations can be effectively utilized in MPPs developed through 3DP. Maa's design theory can be extended to thick MPPs with sub-millimeter perforations with reasonable accuracy. MPPs made of PLA have a lifespan of 80 years under normal conditions, and their bio-degradability can be enhanced by enclosing them beneath industrial compost with suitable additives (Stloukal et al. 2015).

4 PANELS WITH FUNCTIONALLY GRADED SPHERICAL PERFORATIONS

This chapter presents the effects of spherical perforations and their grading pattern on sound absorption and transmission loss behaviour of typical MPP. 3D printing of a perfect sphere is practically impossible. Also, there is no entry point for sound waves if it is done so. Hence a cylindrical hole of 0.5 mm in diameter and height of 10 mm through the thickness of the specimen is provided for all touching points of spheres. This connects them in the incident direction of sound while testing.

4.1 Spherical perforations

Specimens with spherical bubble perforations connected in different sizes are manufactured by FFF-based 3D printing, and acoustic properties are obtained experimentally using an impedance tube. Specimen with series spherical bubble perforations of uniform size and graded size is chosen by exploring possible sizes of bubble variations within a reasonably thick standard cylindrical specimen of 96 mm diameter and 10 mm thickness. This thickness is selected for sufficient strength, stiffness, lesser weight, and good absorption at low frequencies by Sakagami et al. (2008). The bubbles formed an array with tangential point contact with each other. The maximum number of bubbles possible within the specimen is included.

Ten types of perforations formed by joining spherical bubbles connected along the thickness of the specimen were 3D modeled using AUTOCAD 2019. Eight samples having uniform spherical perforations such as U5, U5v, U4, U3, U2, U2v, U1, and U1v are considered (Table 4.1). Here, 'U' represents uniform spherical perforation. The number followed by 'U' represents the diameter of the spherical bubble in mm, and 'v' represents a variant with hemispheres at both the outer surfaces instead of a sphere. For example, U5v is a variant of U5 where two hemispheres of diameter 5 mm are coming at the entry and exit of sound to the specimen on either side of the single 5 mm sphere in the middle along the thickness connected by a 0.5 mm cylindrical hole as mentioned earlier. These samples are analyzed to study the effect of uniform spheres with different porosity in increasing order. As the size of spheres decreases, the number of spheres
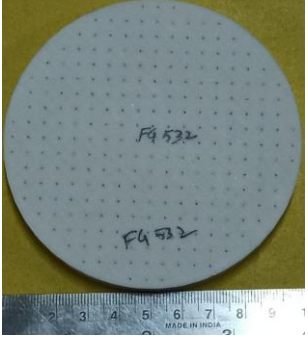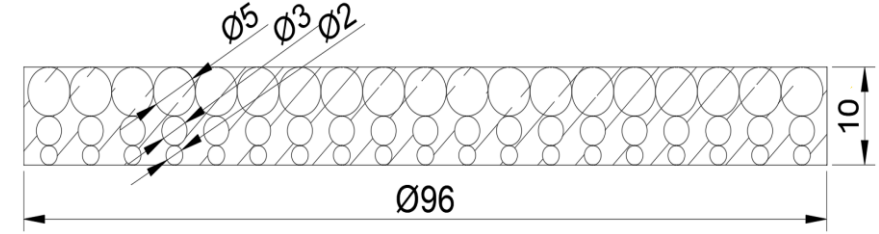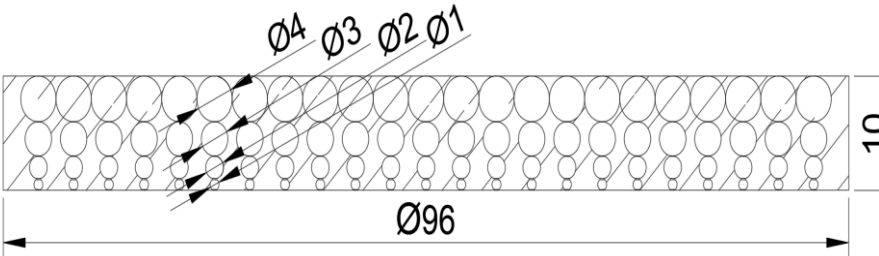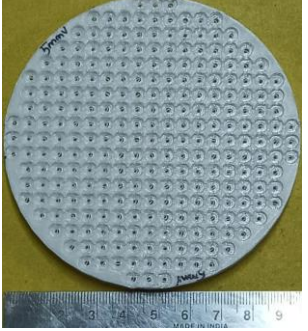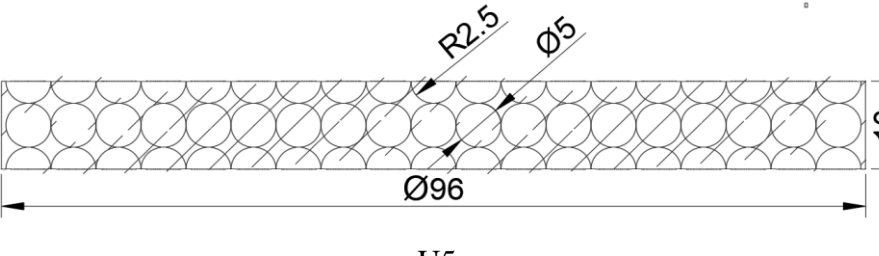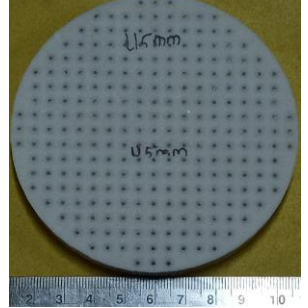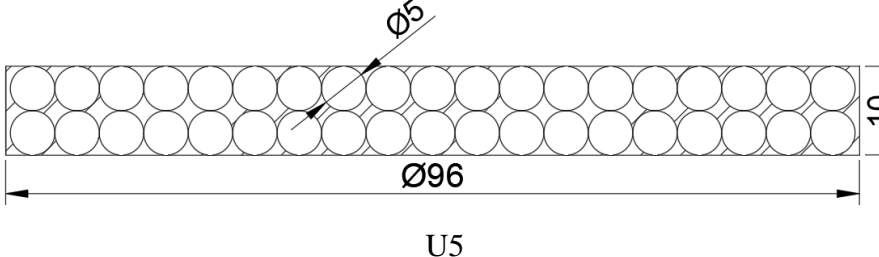
and porosity across cross-sections increases. This variation due to a decrease in the size of spheres and an increase in porosity will affect SA and STL significantly.

Two different functionally graded samples, such as FG532 and FG4321, are considered to study the effect of grading of porosity on SA and STL characteristics. For example, FG532 is a specimen with bubbles of diameter 5, 3, and 2 mm, respectively, connected along with the thickness. FG specimens can be tested for convergent and divergent types of graded porosity by exposing both end surfaces of the test specimen accordingly. For example, if a 5 mm bubble is exposed to incident sound, it is denoted as FG532, and if a 2 mm bubble side is exposed, it is denoted as FG532R (FG532 reversed). One test specimen with typical cylindrical perforation having a perforation diameter of 1 mm (C1), mentioned in chapter no.3 as Const 1, is also considered for the comparison purpose. The sample specimens with the sectioned view are presented in Table 4.1. All the geometries are modeled as CAD files and are converted to .stl format for 3D printing, and G-codes are created employing a standard slicing software SIMPLIFY 3D 4.1.2.

4.2 3D Printing of specimens

The 3D printing machine, PROTOCENTER 999 manufactured by Aha 3D Innovations Pvt. Ltd., India, is used to print the samples. It has a layer resolution of 100 µm along the vertical axis and an accuracy of 28 µm along the horizontal axes. Temperature and printing speed are constant at 200°C and 1440 m/min, respectively, for all the samples. The bed is held at 60°C with ABS paste as the adhesive. The layer thickness is kept constant at 0.25 mm. Room temperature is maintained at 25°C throughout printing. After removing solidified ABS, samples were finished with fine 2000 grit sandpaper, and subsequently, the cloth was used for the glossy-glassy finish. The suitable process parameters yielding excellent finish and fine inter-layer cohesion without porosity are obtained by repeated trials. This process ensures that specimens act as standards without unnecessary errors in SA and STL readings due to porosity or surface roughness developed during 3D printing.

Table 4.1: Samples with different types of spherical perforations.

Photograph of specimen	Full sectioned front view (All dimensions are in mm)
	 FG 532
	 FG 4321
	 U5v
	 U5
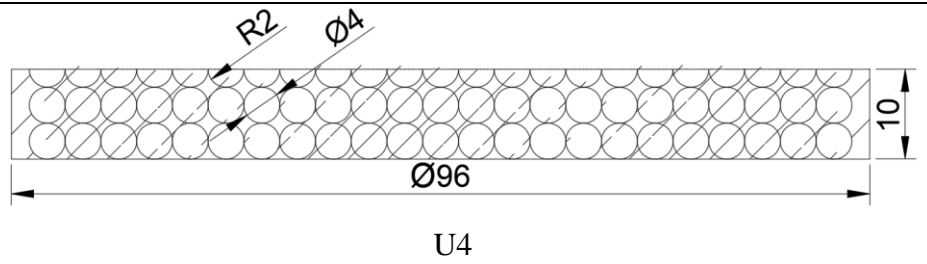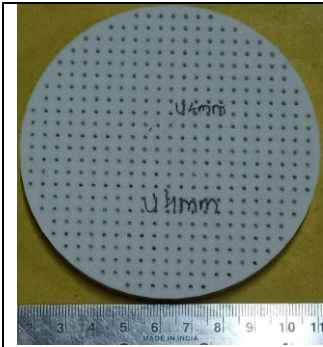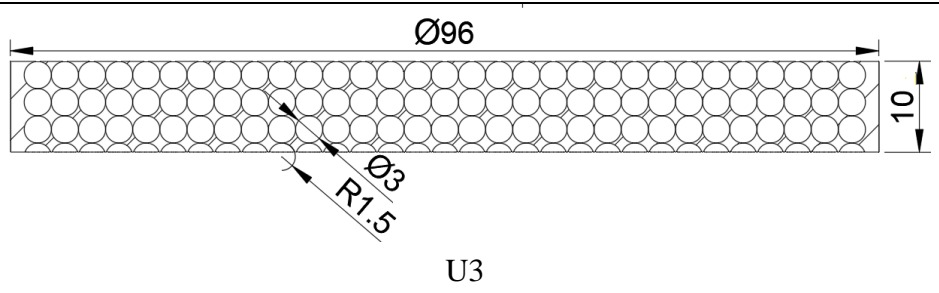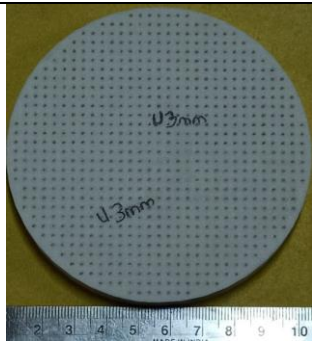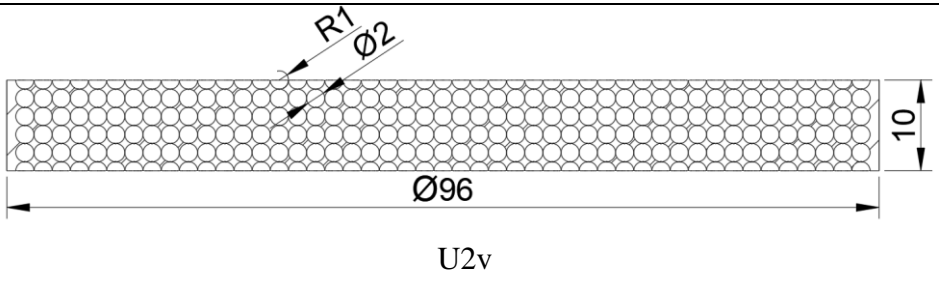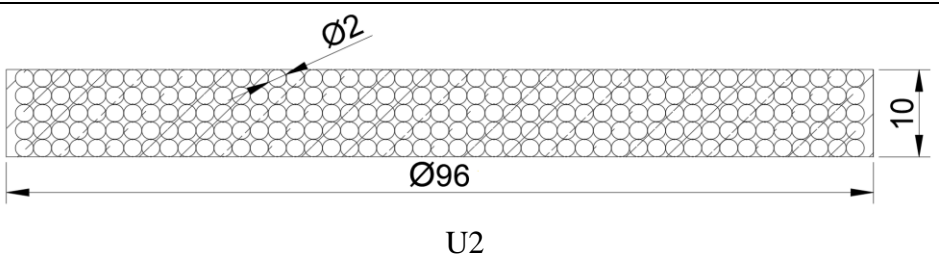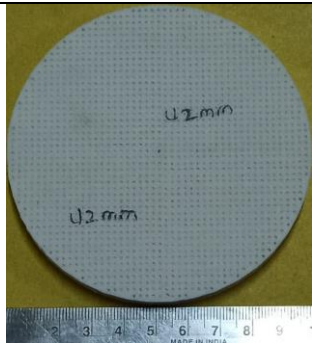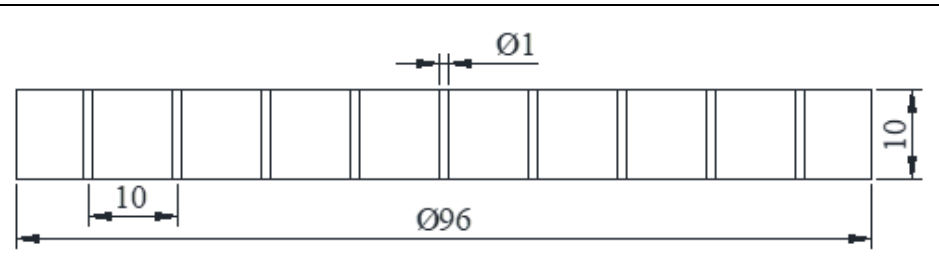
	R2 Ø4 10 Ø96 U4
	Ø96 10 Ø3 R1.5 U3
	R1 Ø2 10 Ø96 U2v
	Ø2 10 Ø96 U2
	Ø1 10 10 Ø96 C1

4.3 Experimental details

Sound absorption and sound transmission loss experiments are carried out on FG perforation specimens with different perforations using an impedance tube setup.

4.3.1 Sound absorption

Following ASTM E1050-19, the SA coefficient is obtained using the two-microphone impedance tube method within the 200-2000 Hz frequency range. Nine standard cylindrical samples with a diameter of 96 mm having a thickness of 10 mm are tested. As shown in Figure 2.3, the source's white noise is amplified and sent to a 16Ω speaker at one end of the impedance tube. Two 1/2" Microtech Gefell diffuse-field microphones quantify both incidents and reflected sound pressures. They are plugged into an M+P Vibpilot 8-channel data acquisition system. Through an M+P spectrum analyzer, the extracted time-domain signal is fed to the MATLAB R2010a program to evaluate the transfer function of the two pressure values. The reflection coefficient and sound absorption coefficient are calculated as mentioned in Section 2.3.1.

4.3.2 Sound transmission loss

As per ASTM E 2611-09, a four-microphone impedance tube test measures STL, as shown in Figure 2.4. The specimen is fixed between the tube's reflection side (upstream) and transmission side (downstream) section. White noise excitation is provided by a small loudspeaker secured at the open end of the upstream side. This leads to a plane wave condition in the tube. The opposite extreme of the transmission side has an anechoic material that is closed by a cap firmly. The microphones measure the complex acoustic pressures p_1 to p_4 at the different positions x_1 to x_4. Normal sound incident sound transmission loss is calculated as in Section 2.3.2.

4.4 Numerical analysis

FEM simulation of FG perforations with bubbles is conducted in the pressure acoustics module of COMSOL 5.4 to estimate SA and STL that are subsequently compared with the experimental values. This numerical model done in COMSOL Multiphysics 5.4 with only air neglects fluid-structure interaction for SA simulation. FG specimen, perfectly-matched-layer (PML), and incident pressure field are modelled. In STL

analysis, two extra domains, one more PML, and a transmitted pressure field are considered. The CAD modelled specimens are imported to COMSOL in a. iges format. PML domain perfectly absorbs all the sound energy incident on it. It is fixed at the pressure field end to prevent reflection. All boundaries are assigned the
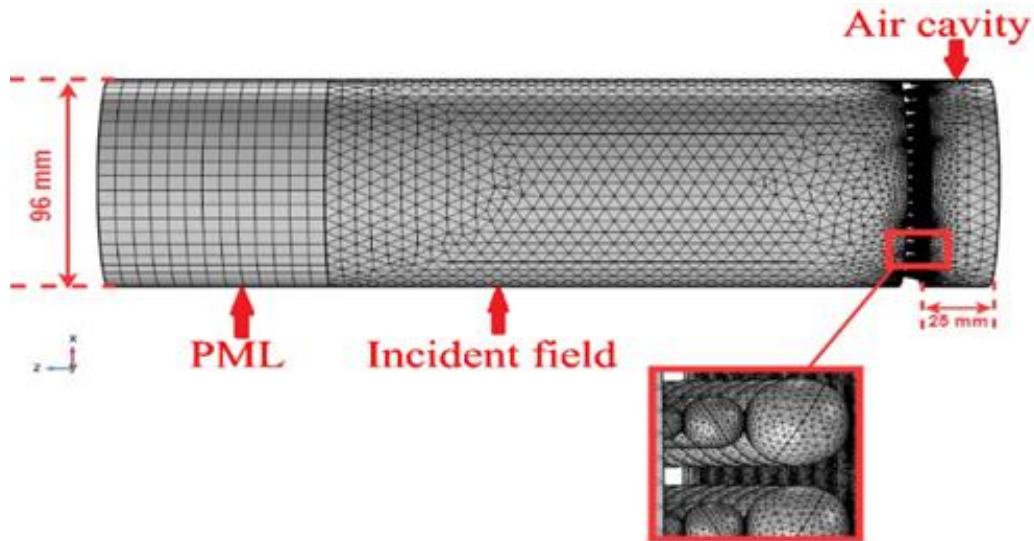
Figure 4.1: Numerical model for finding SA coefficient of the sample 'FG532'.

sound hard boundary wall condition. A background pressure of 1 Pascal is applied inside the pressure field domain. The material in the perforations of the imported CAD model is allocated as air from the in-built library.

A user-controlled mesh is firstly defined in the model. The entire PML is meshed with hexahedron elements. Apart from this, the whole domain is meshed with free tetrahedron elements, as in Figure 4.1. Tetrahedron elements are default elements used for most applications in COMSOL Multiphysics. All 3D volumes, irrespective of topology or shape, can be easily meshed. They can also be used with adaptive mesh refinement. The mesh size is chosen as six elements for each wavelength corresponding to the highest frequency analyzed (Jones 2010). The lowest wavelength, which corresponds to the highest frequency, is obtained by $\lambda_l = c_0/f_h$, where c_0 is the velocity of sound at given temperature, pressure conditions and f_h is the highest frequency considered. A numerical model for obtaining SA includes air domains such as incident field and back air gap (25 mm as above) as in the experiment. However, in the model

44

for STL, the two air domains are the reflection and transmission space, with the specimen separating them, as seen in Figure (4.2). COMSOL acoustic pressure module
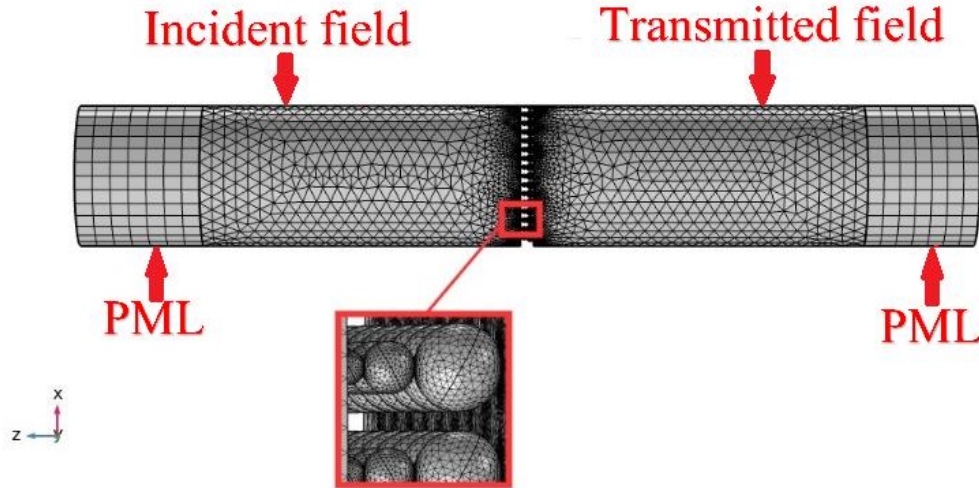
Figure 4.2: Numerical model for finding STL of the sample 'FG532'.

is used to model the elements in the air domain. The air domain in the perforated hole is modelled separately using the thermo-viscous acoustic module for quantifying dissipation due to visco-thermal effects. Multiphysics coupling enables combining thermo-viscous and pressure acoustic physics (Zhang et al. 2015). We get the incident acoustic pressure (pi) and the reflected acoustic pressure (pr) on post-processing. Reflection coefficient is calculated as, $R = (p_r/p_i)$. From this, the acoustic absorption coefficient, $\alpha = 1 - |R|^2$. Eventually, STL is obtained as,

$$STL = 10 \log \left[\frac{Pin}{Pout}\right] \tag{4.1}$$

where Pin and Pout are the input and output sound power at the inlet and outlet port surface.

4.5   Results and discussion

4.5.1   Sound absorption
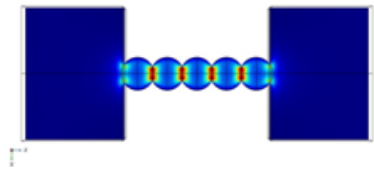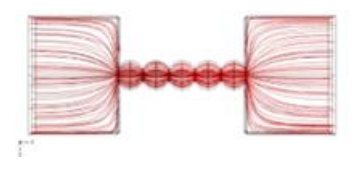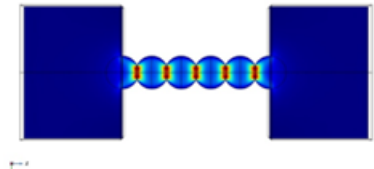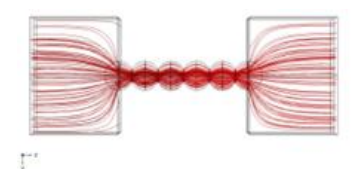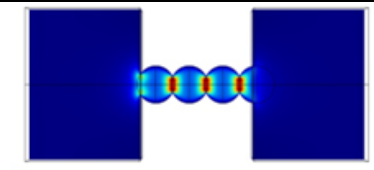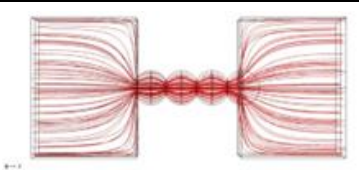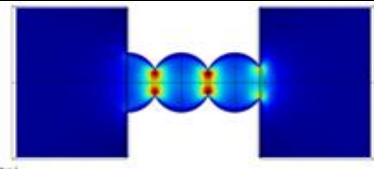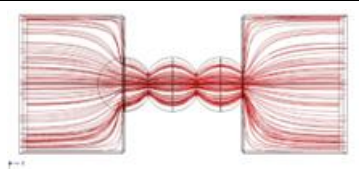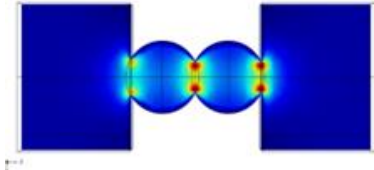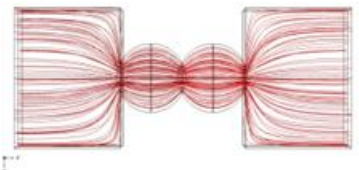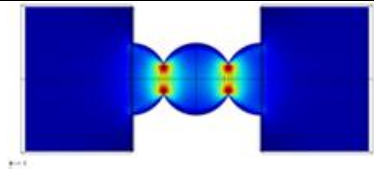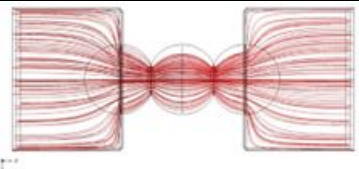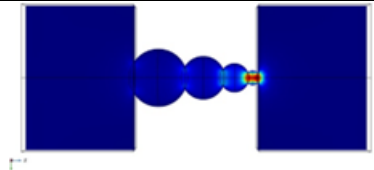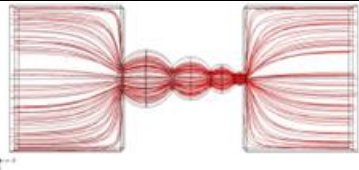
The effect of uniform spherical porosity on the SA coefficient with different spherical bubble sizes is presented in Figure 4.3. From Figure 4.3, it is clear that there is an enhancement in the SA coefficient with a reduction in the diameter of spherical bubbles.

It is also observed that, unlike typical cylindrical pores, the test specimen with uniform diameter bubbles exhibits a better SA coefficient over a wider range of frequencies. Here friction and viscous shear play a dominant role, and other mechanisms like structural vibration and scattering play a minor role in dissipation. As observed from Figure 4.3, specimens with uniform size bubbles act as good absorbers with peak absorption coefficients varying from 0.7323 to 0.9998. This points to the fact that the spherical hollow paths connected in the series act as very good dissipators of sound energy. As the diameter of spherical bubbles decreases, the absorption coefficient increases significantly, as seen in Figure 4.3.

As expected, the friction and thermo-viscous dissipation increase as the bubble diameter decreases due thickening of the boundary layer with a decrease in the bubble size (Table 4.2). The porosity associated with each specimen is listed in Table 4.3. The number of pores per unit area of a cross-section perpendicular to incident sound and overall porosity increases as the bubble diameter decreases. As the bubble size decreases from 5 to 2 mm, the number of bubbles increases, and the sound propagation path gets significantly narrowed with enhanced resistance. This substantially increases the thickening of streamlines and offers higher solid-fluid and fluidic intermolecular interactions. Thus, the friction and viscous shear will be much higher in smaller bubbles, which accounts for their better peak value and bandwidth performance.

The influence of uniform spherical bubble specimens with open hemispherical bubbles at the surfaces (U2v) on the SA coefficient is shown in Figure 4.4 for spherical bubbles with a 2 mm diameter. As observed in Figure 4.4, the constant diameter bubble specimen (U2v) variants have a higher SA coefficient than the U2. Open hemispherical bubbles at the surfaces also lead to wider frequency bandwidth with SA coefficient values greater than 0.75. This is due to a higher amount of sound energy with the fluid column incident at the wide hemispherical inlet of the perforations (Table 4.2), which leads to lower reflection. The energy has to pass through the smaller holes encountering a tortuous path resulting in comparatively higher dissipation through absorption. For example, U2v has thorough dissipation at five identical narrow necks, whereas U2 has

Table 4.2: Viscous boundary layer developed in each perforation with corresponding streamlines.

Specimen	Slice	Streamline
	$\times 10^{-3}$ 45 40 35 30 25 20 15 10 5 0 (m/s)	
U2		
U2v		
U3		
U4		
U5		
U5v		
FG4321		

FG532		
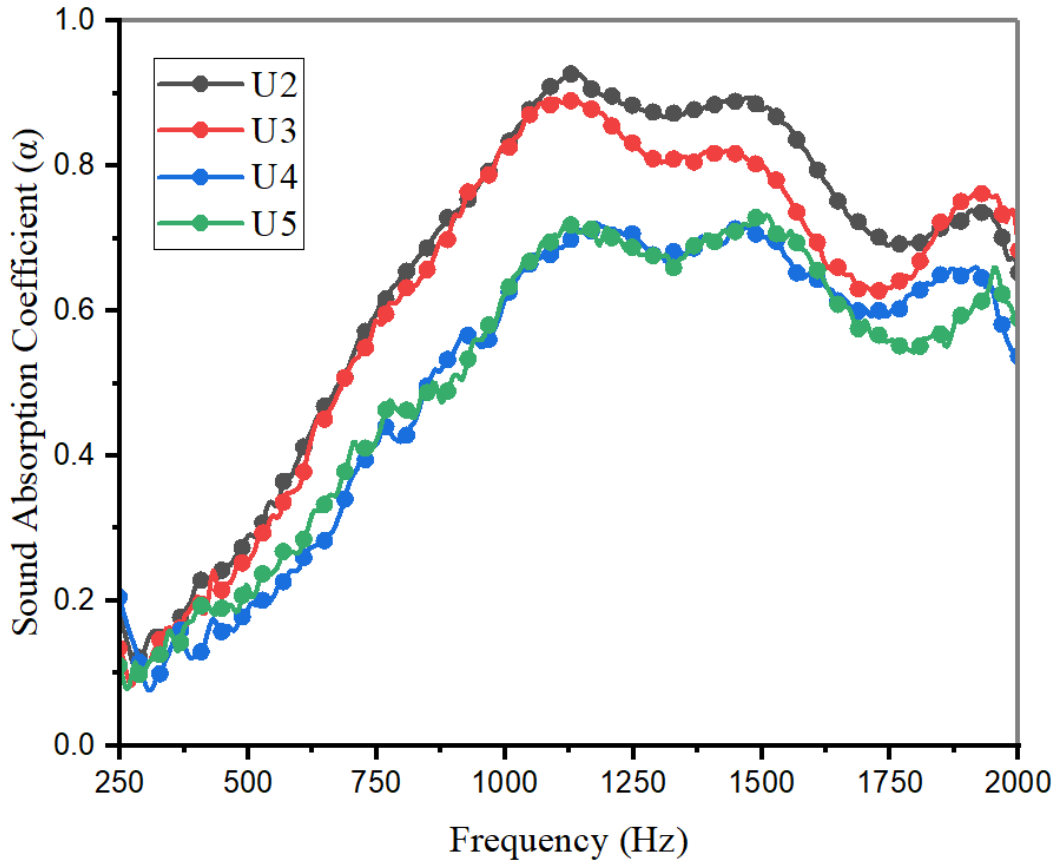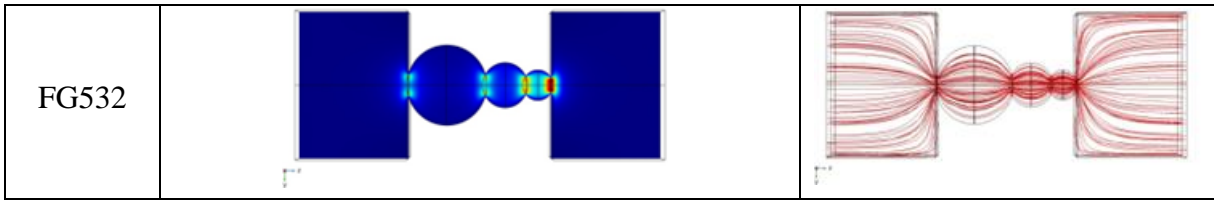
Figure 4.3: Influence of spherical bubble diameter on SA coefficient.

four, as observed in Table 4.2. Hence U2v gives better performance compared to U2 (Figure 4.4). Consequently, quantitatively, more energy absorption occurs effectively in 'U2v' than their U2 counterparts of the same bubble size.

The effect of graded spherical porosity on SA coefficients is significant, as seen in Figure 4.5. In Figure 4.5, in the FG4321 case, the test specimen's 4 mm spherical bubble side is exposed to the incident sound field, while in FG4321R, 1 mm faces the sound. It is performed to analyze the divergent (FG4321R) and convergent (FG4321) types of functionally graded porosity on the SA coefficient. From Figure 4.5, it is clear that the
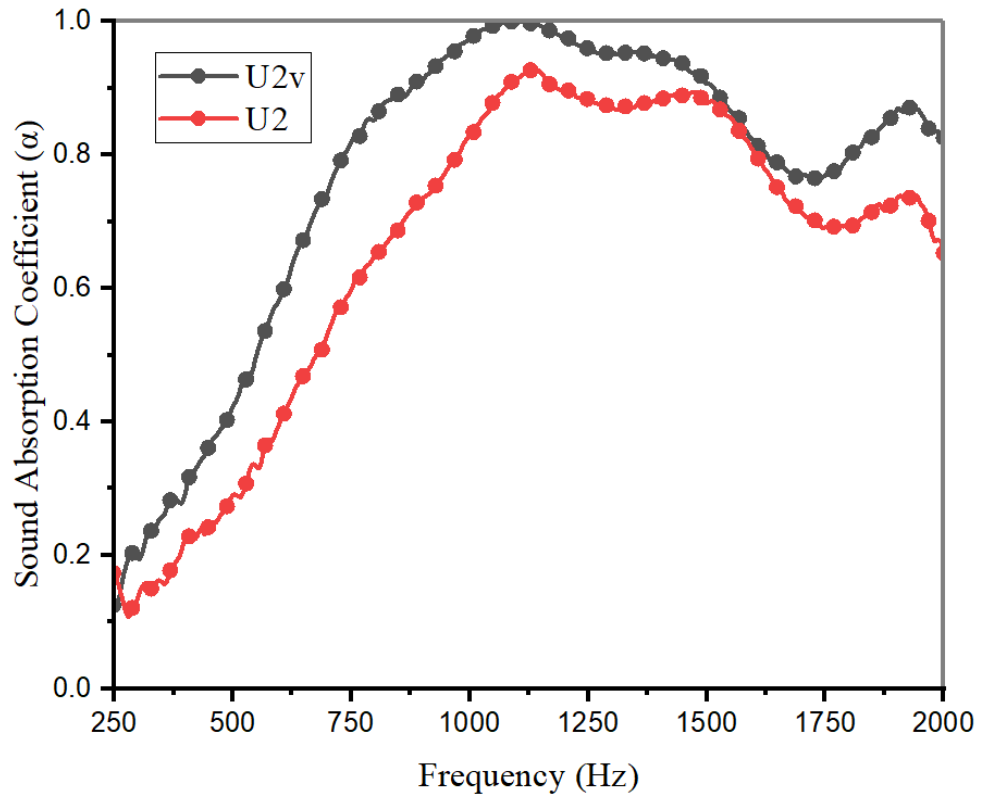
Figure 4.4: Influence of uniform spherical bubbles with open hemispherical bubbles at the extreme surfaces on SA coefficient.

behavior of FG4321 and FG4321R is entirely different from FG532 and FG532R in terms of peak value and frequency bandwidth with SA coefficient values greater than 0.75. In FG4321 and FG4321R, the peak value of the SA coefficient and bandwidth of frequency is less.

However, FG532 and FG532R are better at corresponding to peak values and bandwidth. The peak value of the SA coefficient for FG4321 and FG4321R samples is 0.8459 and 0.7139, respectively. Even though the peak values are relatively low, they are still excellent absorbers in 250-500 Hz. The bandwidth decreases in FG4321 and FG4321R cases due to the low number of perforations per unit area and lesser porosity, which increases reflection except nearer to the resonance frequency. However, FG532 and FG532R samples have a significantly higher bandwidth of 500-1500 Hz with the higher peak values of 0.9778 and 0.9720, respectively. In addition to solid-fluid friction

and viscous shear in the fluid resulting from it, the effect due to stepping is a significant factor for energy dissipation in FG specimens.

Sudden stepping increases thermo-viscous losses significantly due to additional impedance (Jiang et al. 2020). The paths become tortuous increasing friction, viscous shear, and scattering especially at the steps significantly. Besides this effect due to convergence in FG4321, FG532 and divergence in FG4321R, and FG532R, dissipation gets enhanced as in sound absorption with varying cross-sections (Section 3.6.1). There is a summation effect of uniform bubble size and its variation. Hence, they do not have significant bandwidth over a wide range at par with uniform bubble specimens, U2 or U2v. Nonetheless, the performance of FG specimens at lower frequencies up to 1500 Hz is superior to all uniform bubble specimens in terms of SA and bandwidth.
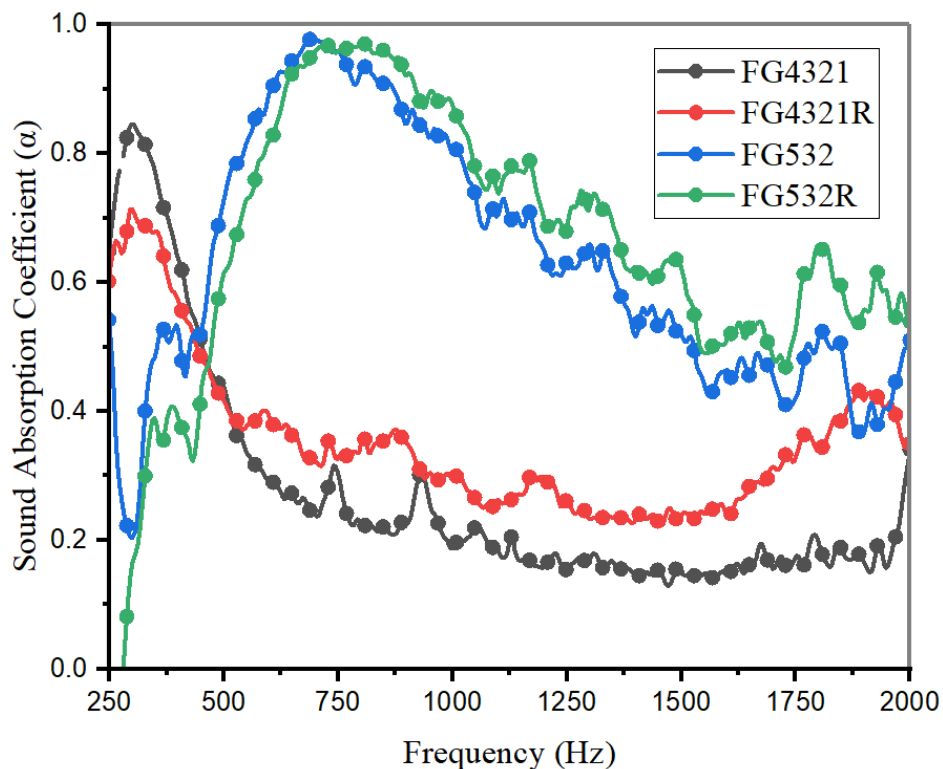
Figure 4.5: Effect of functionally graded spherical porosity on SA coefficient.

From Figure 4.5, it is observed that all specimens have high peak values and higher bandwidth than the FG specimen FG4321R. FG4321R is chosen for reference among all available specimens, since only this specimen could, in the best way, dimensionally

50

approximate the 0.5 mm cylindrically perforated specimen, with its 0.5 mm entry hole and 1 mm diameter sphere at the inlet itself. The performance of FG4321 is observed to be better both in terms of peak absorption and bandwidth in the range of frequency 250 to 400Hz. FG532 and FG532R performed better on the higher frequency side of FG4321R, with a very high peak 'α' value in 450 to 1500 Hz. Relatively better performing constant diameter spherical specimens, U2 and U2v performed better both in terms of peak SAC value and bandwidth in the range of frequency 675 to 2000 Hz.

The grading effect is significantly highlighted by comparing these specimens with the remaining samples. The higher the grading rate with respect to the distance, the sound absorption is better in terms of both bandwidth and values of SAC over the lower frequency range. Still, the lowest frequency range of 0-500 Hz is more absorbed by FG4321, with low diameter holes having a lower grading rate. The variation of bubble diameter will have a stepped perforation effect increasing expansion/contraction and bending of sound waves during travel and the effects produced in the case of constant diameter bubbles. With remarkably low porosity, the FG specimens give a very high peak absorption coefficient at a low frequency over a reasonable bandwidth of lower frequency (Table 4.3 and Figure 4.6). Figure 4.5 also clearly indicates that the spherical porosity and its grading can be tuned according to the sound absorption requirement for a given frequency range.

From Figure 4.6, it is observed that all specimens have high peak values and higher bandwidth than the FG specimen FG4321R. FG4321R was selected for reference among all available specimens, since only this specimen could, in the best way, dimensionally approximate the 0.5 mm cylindrically perforated specimen, with its 0.5 mm entry hole and 1 mm diameter sphere at the inlet itself. The performance of FG4321 is observed to be better both in terms of peak α and bandwidth in the range of frequency 250 to 400Hz. FG532 and FG532R performed better on the higher frequency side of FG4321R, with a very high peak α value in 450 to 1500 Hz. Compared to constant diameter spherical specimens, U2 and U2v performed better in terms of peak SAC value and bandwidth in frequencies 675 to 2000 Hz.

The grading effect is significantly highlighted by comparing the FG specimens with the remaining samples. The higher the grading rate regarding the distance, the better the sound absorption is in terms of bandwidth and values of SAC over the lower and mid-frequency range. Still, the lowest frequency range of 0-500 Hz is more absorbed by FG4321, with low diameter holes having a lower grading rate. The variation of bubble diameter will have a stepped perforation effect increasing expansion/contraction and bending of sound waves during travel and the effects produced in the case of constant diameter bubbles. The FG specimens with remarkably low porosity give a very high peak absorption coefficient at a lower frequency over a reasonable bandwidth (Table 4.3 and Figure 4.6). Moreover, their performances are best in the lower frequency range (200 to 1500 Hz), the best range for sound quality enhancement and pollution control for humans (Leventhall 2004). Figure 4.6 also clearly indicates that the spherical
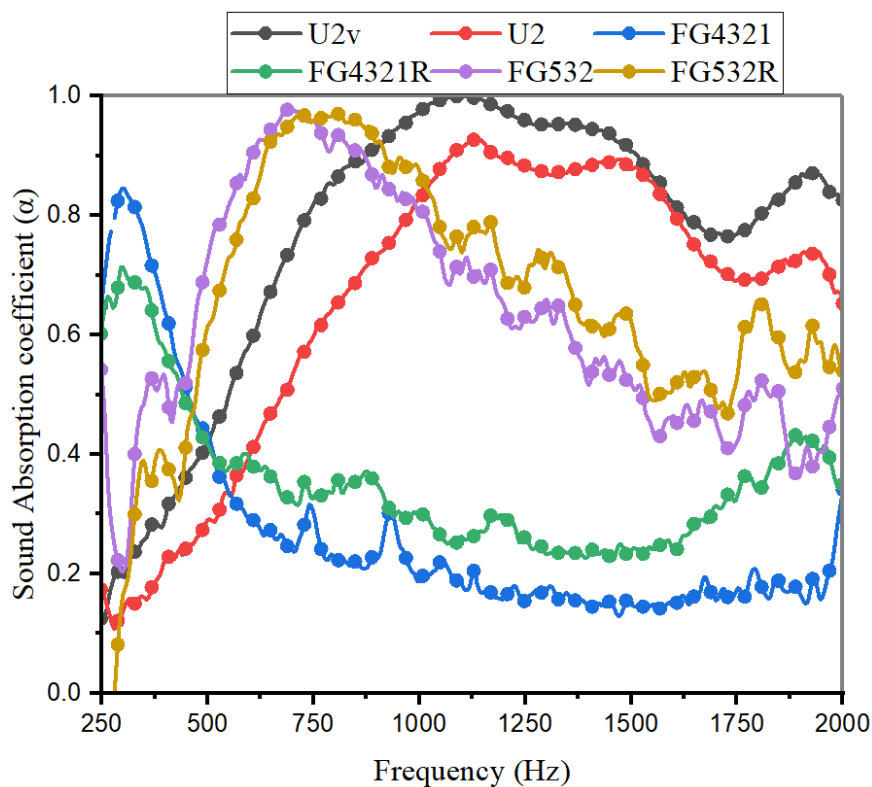
Figure 4.6: Comparison of the SA coefficient of best-performing specimens.

Table 4.3: Porosity and maximum experimental value of SA coefficient obtained for each specimen.

Sl.No.	Specimen	Average Porosity = (V_H/V_T)* in %	Maximum value of sound absorption coefficient (α_{max}) [for 200-2000 Hz]	Frequency bandwidth for SA coefficient, $\alpha > 0.70$ (± 2 Hz)
1	U2	50.38	0.9275	1032
2	U2v	50.38	0.9998	1336
3	U3	47.68	0.8922	880
4	U4	48.73	0.7207	264
5	U5	47.20	0.7323	304
6	U5v	47.20	0.7738	192
7	FG532	30.21	0.9778	640
8	FG532R	30.21	0.9720	752
9	FG4321	30.45	0.8459	116
10	FG4321R	30.45	0.7138	20

* Where V_H = Hollow volume of the specimen = No. of bubbles x Volume of each bubble. V_T = Total volume of the cylindrical specimen.

porosity and grading can be tuned according to the sound absorption requirement for a given frequency range.

4.5.2 Sound transmission loss

The effect of uniform spherical porosity on STL with different spherical bubble sizes is shown in Figure 4.7. From Figure 4.7, it is clear that there is an enhancement in STL with a reduction in the diameter of spherical bubbles based on the average of the pulsating curves. It is also observed that the test specimen with uniform diameter bubbles exhibits an increase in STL with an increase in frequency. The friction and viscous shear effects play a dominant role, and other mechanisms like structural vibration and scattering play a minor role in dissipation. As observed from Figure 4.7, specimens with constant size bubbles act as good dissipators with STL varying from 0-20 dB. This points to the fact that the spherical, hollow paths connected in the series
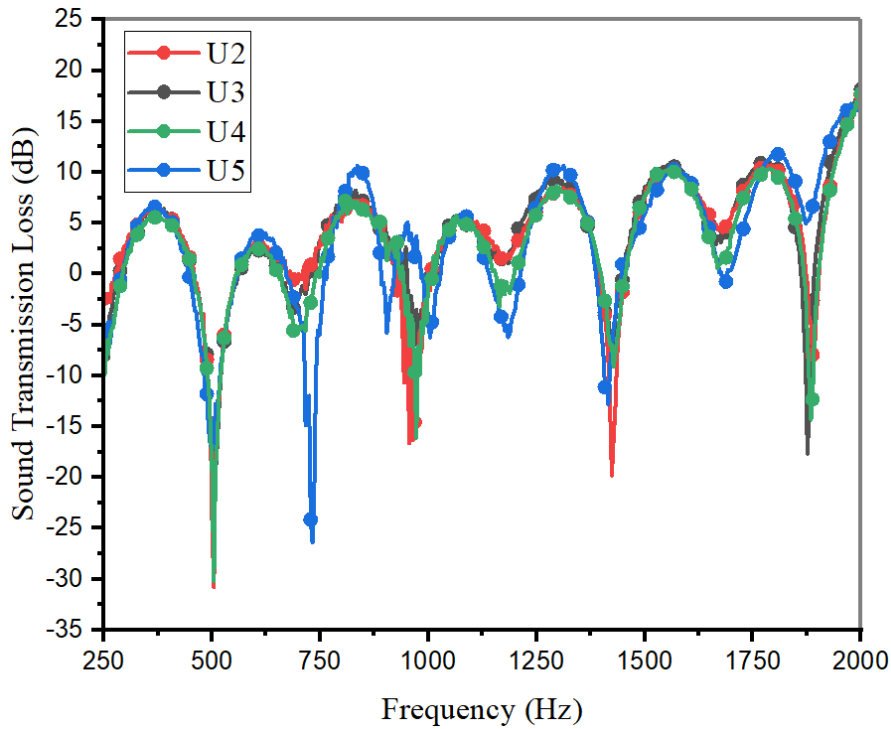
Figure 4.7: Influence of uniform spherical bubble size on STL.

act as very good dissipators of sound energy. As the diameter of spherical bubbles decreases,, the STL increases significantly, as evident from Figure 4.7.

All samples with bubble perforations in the series act as good dissipators of sound energy with dissipative effects increasing with frequency from 200 to 2000 Hz. The dissipation increases with a decrease in bubble size in specimens since smaller bubbles give rise to closer and denser streamlines, leading to higher friction and visco-thermal dissipation effects. Also, the number of perforations per unit area and the porosity are higher in smaller bubble specimens, further reducing the reflection of sound waves. Moreover, the number of small diameter bubbles encountered by the sound passing through the specimen is greater. These factors enhance transmission loss, significantly increasing overall dissipation (Figure 4.7).

The influence of uniform spherical bubble specimens with open hemispherical bubbles at the surfaces (Uv) on STL is shown in Figure 4.8 for spherical bubbles with a 2 mm

diameter. As observed from Figure 4.8, the variants of constant diameter bubble specimen (U2v) have higher STL compared to U2. Open hemispherical bubbles at the surfaces also lead to an increase in STL values by 7 dB. This is because a higher quantity of sound energy with the fluid is incident at the wide hemispherical inlet of the perforations as shown in Table 4.2, which after entering the tortuous path have a conjusted movement through the smaller hole yielding higher dissipation as well as higher transmission losses at the inlet bubble itself. For example, U2v will have thorough transmission losses at the five narrow necks compared to U2, which encounters only four similar necks, as shown in Table 4.2. The boundary layer gets crowded with streamlines enhancing velocity gradient at those necks, increasing the solid-fluid and inter-fluid frictional losses. Hence U2v exhibits better performance in terms of sound transmission loss than U2, as evident from Figure 4.8. The effect of functionally graded spherical porosity on STL is significant, as depicted in Figure 4.9.
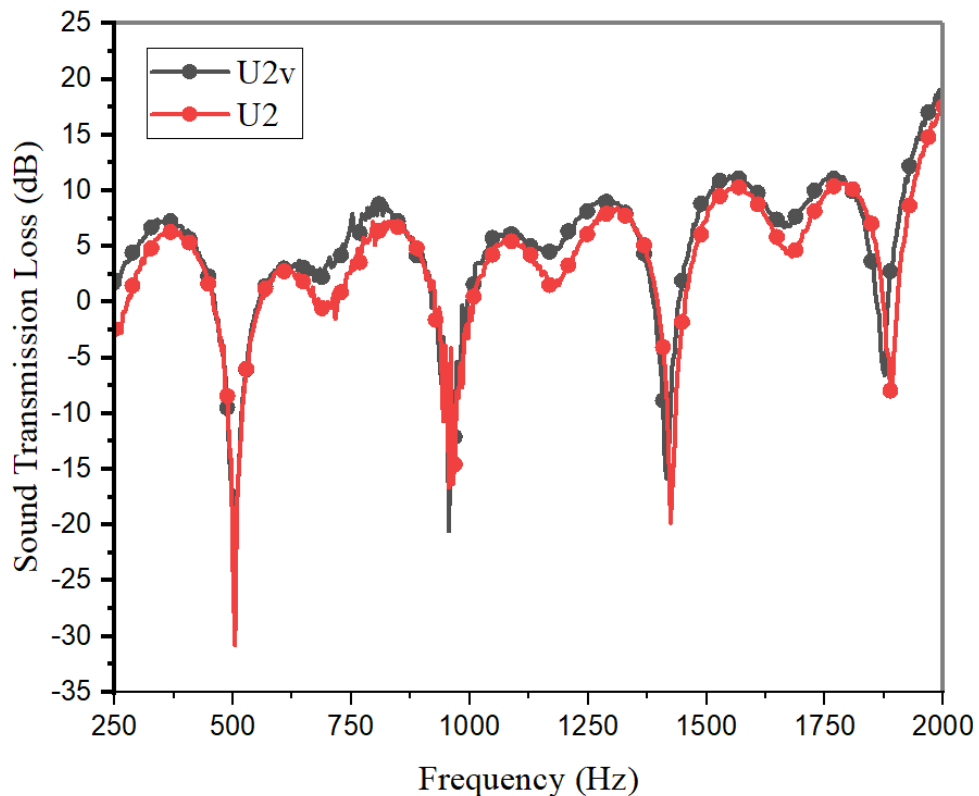
Figure 4.8: Influence of uniform spherical bubbles with open hemispherical bubbles at the extreme surfaces on STL.
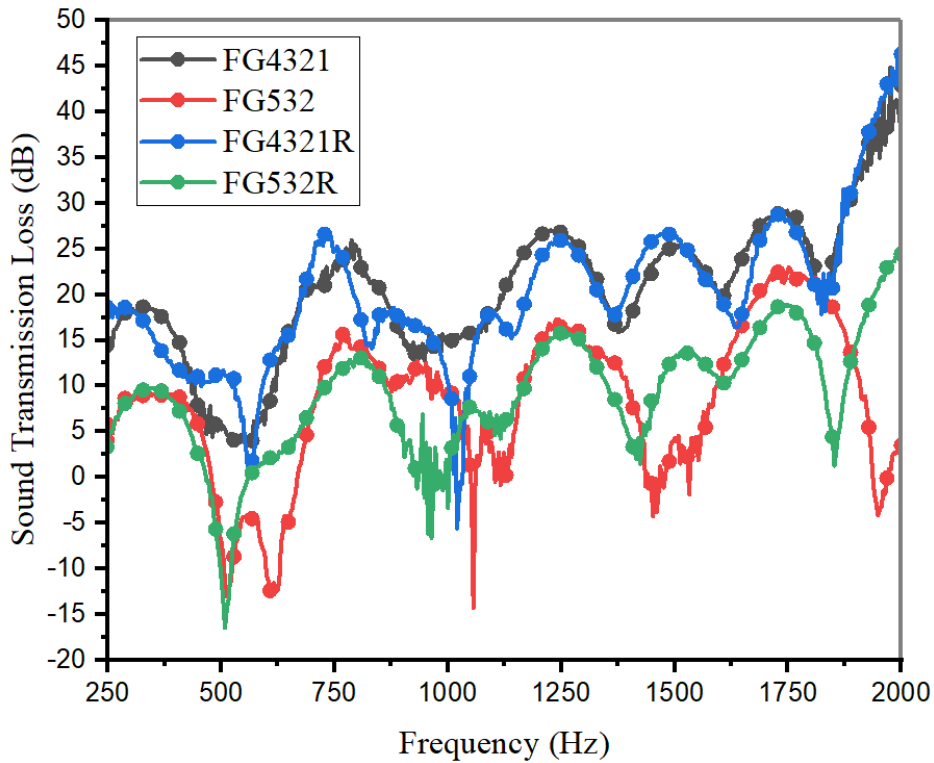
Figure 4.9: Effect of functionally graded porosity on STL.

In FG4321 specimens, the value of the STL exceeds the FG532 specimens by a margin of about 20 dB. The value of the STL for FG4321 varies from 5-40 dB, and for FG4321R samples, it is 7-45 dB. In addition to the normal dissipation phenomenon, stepping, convergence in specimens FG4321 and FG532, and divergence in specimens FG4321R and FG532R result in the highest transmission losses for FG specimens. Hence, they yield the best transmission loss over the whole range of frequency compared to all other specimens, and the margin also increases significantly with frequency, as observed in Figure 4.9. FG4321 specimens perform better than FG532 due to the thickest boundary layer having closer streamlines (Table 4.2) which gets thicker and thicker at each narrowing step in the case of converging paths. In diverging specimens like FG4321R and FG532R, the maximum losses occur at entry and expansion losses. Sound transmission loss of different specimens is obtained in the descending order of FG4321 > FG4321R > FG532 > FG532R > U2v > U2 > U3 > U4 > U5.
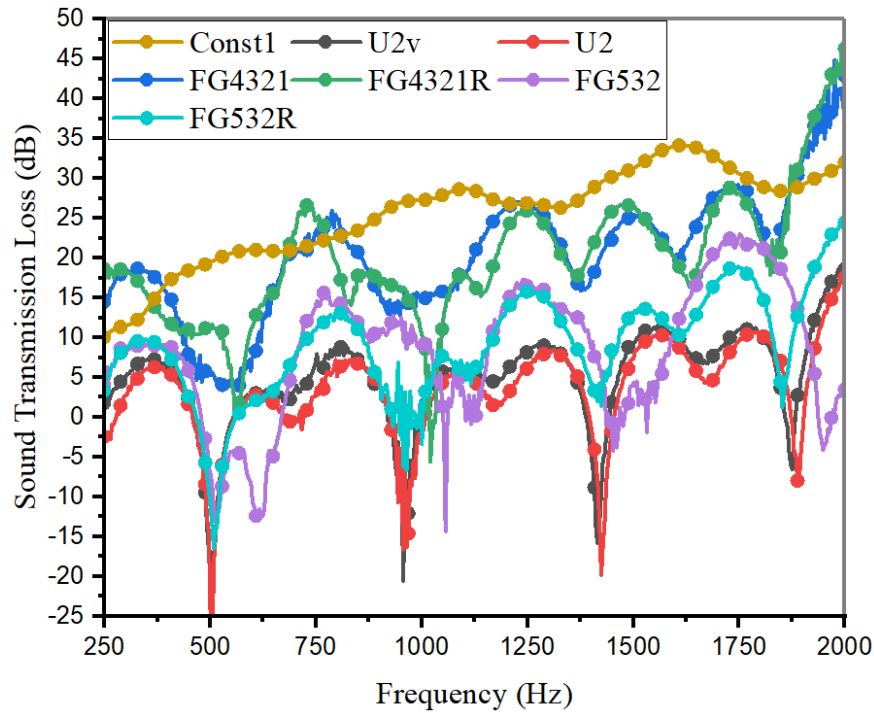
Figure 4.10: Comparison of STL of the best performing specimens obtained from experiment.

Even though the number of perforations and porosity is significantly lower in the case of FG specimens, they exhibited the best STL characteristics with more than 10 dB margin compared to the remaining samples (Figure 4.10). A comparison is carried out with a cylindrically perforated specimen of 10 mm thickness and 96 mm diameter designed as per Maa's procedure, having 1 mm diameter perforations. Resonance losses creep in FG and cylindrical specimens. It is observed that the performance is comparable up to 1800 Hz, wherein FG4321 specimens have a remarkably exceeding margin beyond that. This highlights the relevance of functional grading in specimens' perforations of similar profiles in terms of SA and STL. With fewer perforations, significant absorption is achieved, especially at lower frequencies with reasonable bandwidth and higher transmission losses which increase significantly with frequency compared to constant diameter bubble specimens.

The closer the streamlines in a long boundary layer, the heavier the dissipation. The curvatures, narrow entries, exit, expansion, and contraction induce the tortuosity and scattering. Longer tortuous paths result in a higher loss of energy. Further, enclosed air in bubbles might act as acoustic dissipators, effectively dispersing the oscillating sound

waves. The narrow bubble perforations exhibit the best dissipation due to the thickest boundary layer formed inside the narrowest paths, as seen in Table 4.2. In FG specimens, the frequency range drops close to 1000 Hz, which helps in the dissipation of human voices. After continuous usage, the surface finish of perforations deteriorates (due to accumulation of entering dust particles, moisture, and dirt), enhancing bubbles' dissipation capacity. Thus, FG specimens are superior application-wise in comparison to others.

4.5.3   Comparison of experimental and simulation results

The Air domain inside the spherical perforations is modelled using the thermos-viscous-acoustics module of COMSOL, accounting for visco-thermal losses. *The Thermo-viscous-acoustics module in COMSOL provides an accurate and straightforward procedure to set up and solve the acoustic model for* acoustic pressure, sound velocity, and temperature variation. Solid-fluid interactions are neglected to simplify the model. The model has an inlet and outlet (modeled using ports) and an intermediate part depending on the perforation geometry. The acoustics in the perforations are modelled with a thermo-viscous-acoustic module for a detailed analysis of the thermal and viscous losses, and the boundary layer diagram obtained for different perforations is plotted and presented in Table 4.2. Such graphs obtained from simulations help attain the best results before printing, reducing lead times and meeting industrial requirements more effectively.

The numerical result obtained using COMSOL for each specimen is compared with the corresponding experimental result of SA and STL. The FEM simulations agree with experimental results for all the cases (Figure 4.11-4.14). Numerical and experimental results match well, including resonant frequencies for all the cases. Nevertheless, the experimental results overpredict at extreme points of the frequency axis. It may happen due to the non-compliance to the assumptions that the solid is perfectly rigid and its surface is smooth. Practically a non-rigid, rough surface intensifies solid-fluid interaction via frictional and visco-thermal dissipation leading to increased absorptivity. Nevertheless, specimens made of PLA did not deviate from both

assumptions due to the excellent surface finish, the exactness of dimensions, and flawless deposition during 3D printing owing to suitable parameters.
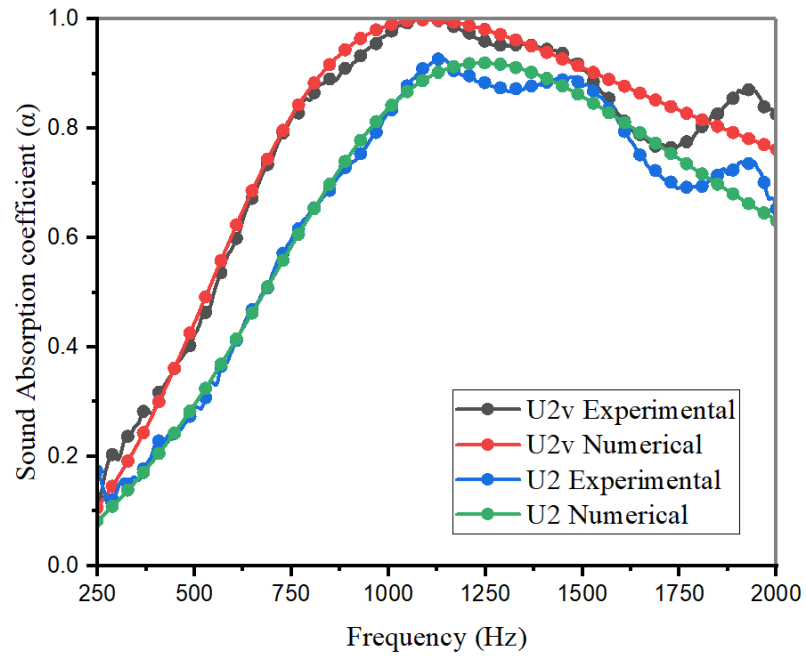
Figure 4.11: Numerical and experimental results comparison for U2 and U2v PLA specimens.
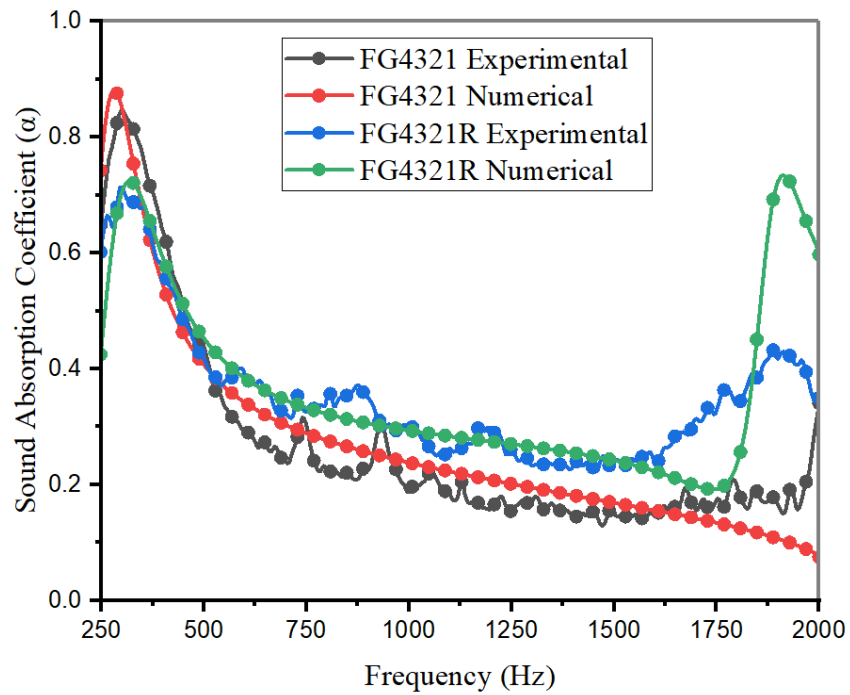
Figure 4.12: Numerical and experimental results comparison for FG4321 and FG4321R PLA specimens.
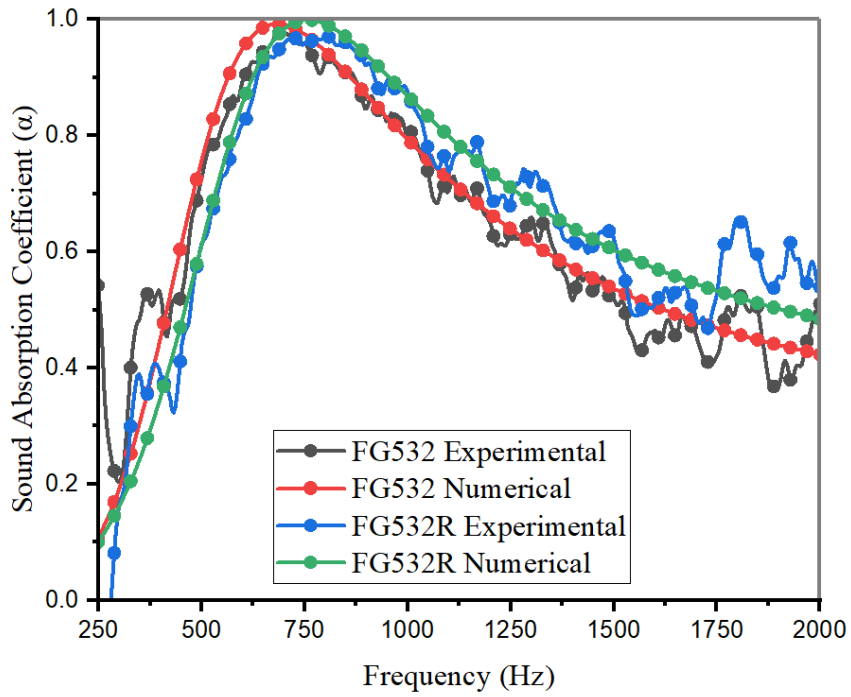
Figure 4.13: Numerical and experimental results comparison for FG532 and FG532R PLA specimens.
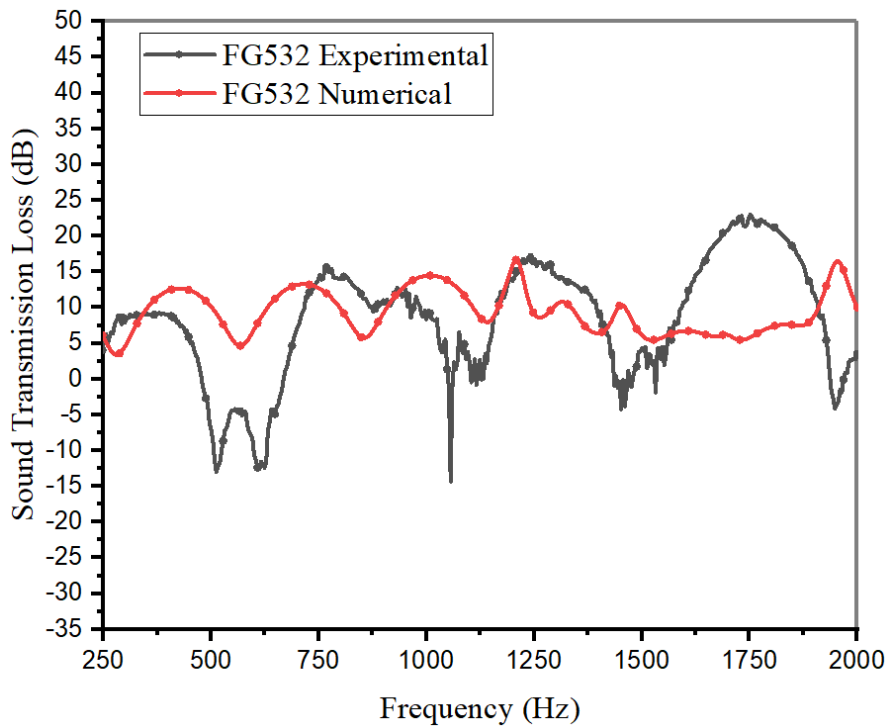
Figure 4.14: Numerical and experimental results comparison for STL of FG532 PLA specimen.

The fluctuations are usually observed in sound transmission loss obtained by an experimental approach. The ripples in the experimental STL curves cannot be avoided entirely in an experimental setup due to vibration or errors in setup and accessories. However, it can be minimized using high-quality components, fittings, and accessories to the best possible extent. The impedance tube is made of acrylic to reduce vibrations. All experiments are conducted with adequate damping, evident from oscillation-less SA curves. Anechoic termination is carried out using a 100 mm thick PU foam with a minimum SA coefficient of 0.95. The imperfect anechoic termination also causes oscillation in the STL curve. (Pispola et al. 2005) reported oscillation in the STL curve with anechoic termination of limited flow resistivity and high porosity material. The edges of the specimen are tapped using teflon, which fits tight inside the impedance tube. The tight fit of sample attribute oscillations in the STL curve (Kino and Ueno 2007).

4.6   Conclusion

The influence of spherical bubble perforation and its grading on SA and STL characteristics of 3D printed bio-degradable material is presented. Effects of size of the spherical bubble and different types of patterns of graded spherical perforation on SA and STL characteristics of 3D printed PLA specimens are studied experimentally. Furthermore, experimental results are weighed up against numerical results. Based on the studies, the following conclusions are drawn.

- The influence of spherical bubbles' size and grading pattern on SA and STL behavior is significant.
- In uniform diameter bubble specimens, smaller spherical bubbles have a better SA coefficient.
- FG532 perforations enhanced SA performance in the lower frequencies up to 1000 Hz in a functionally graded case.
- The STL response of FG4321 and FG4321R specimens are better than in the other cases.
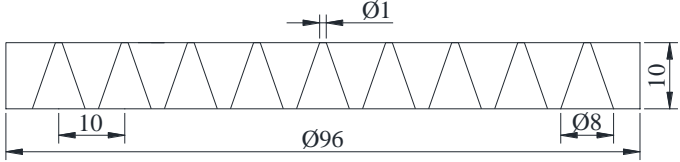
- Narrow perforations perform better in SA and STL characteristics since the dissipation is better due to closer streamlines, greater perforations per unit area, and higher porosity.

- Thus, spherical perforations with uniform and graded porosity can be tailored for applications that dissipate a wide range of desired frequencies, thereby controlling noise pollution.

5 STUDIES ON 3D PRINTED WOOD/PLA COMPOSITE PANELS

This chapter presents the influence of adding wood filler on sound absorption and transmission loss of PLA panels. The samples exhibiting the best performance among the different types of varying cross-sections and spherical perforations analyzed in chapters 3 and 4, respectively, are considered in this study.

5.1 Samples with varying cross-section and spherical perforations

Three best performing samples, i.e., C (earlier denoted as C1 and Const1), DC, and D, are based on the cross-section analysis in chapter 3, and four best performing samples, i.e., U2, U2v, FG532, and FG4321, are based on the spherical perforation analysis in chapter 4, are considered for this study. Here, U2 is a specimen having five interconnected spheres with a cylindrical hole connecting them along with the thickness of the specimen. U2v is a variant of U2 where two hemispheres of diameter of 2 mm are coming at the extreme ends of the perforation. Two samples containing sphere bubbles of different sizes like FG532 and FG4321 are considered to analyze the grading of porosity on SA and STL. FG532 is a specimen with bubbles of diameters 5, 3, and 2 mm, respectively, connected in series by the 0.5 mm cylindrical hole through the thickness. On similar lines, FG4321 is also 3D printed. In the FG532 sample, if the 5 mm bubble is exposed to incident sound, it is denoted as FG532, and if the 2 mm bubble is exposed, it is designated as FG532R (FG532 reversed). All the CAD files are converted to .stl format for printing, and G-codes are created employing a standard slicing software Ultimaker CURA 4.8.

Specimen Photograph	Sectioned view about diameter (Dimensions in mm)
	D

figure — sectioned view of specimen D with dimensions Ø1, 10, 10, Ø96, Ø8

	DC
	C
	U2
	U2v
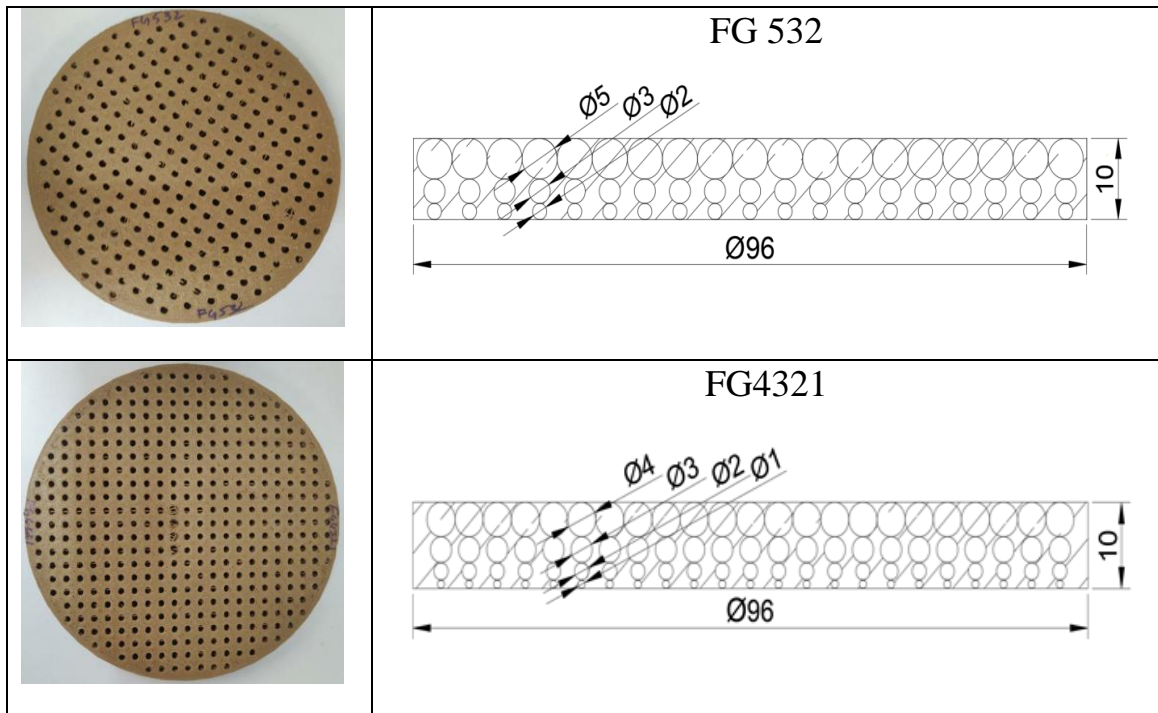
Figure 5.1: FDM specimens with details.

5.2   3D Printing of specimens

Ultimaker Extended 2+ 3D printer, manufactured by Ultimaker BV, Netherlands, available at 3D printing lab, B.M.S College of Engineering, Bangalore, India, is used to produce the specimens through FDM. The printing temperature is maintained constant at 205°C and 50 m/s feed rate and travel speed of 70 mm/s for all the samples. The printer bed and room temperature are maintained at 60°C and 25°C, respectively. Layer thickness is 0.2 mm. After removing the solid Glue used for fixing the model, samples are post-processed with 2000 grit sandpaper followed by cloth for the glossy-glassy finish. Repeated trials have resulted in suitable process parameters yielding excellent finish and fine inter-layer bonding without any porosity. A full section view of all specimens analyzed is shown in Figure 5.1. It was practically too difficult to print specimens with very small spheres inside them, especially 2 mm and 1 mm. A total of 250 of machine-hours were spent printing the seven specimens due to repeated nozzle clogging from the short wood fiber accumulation. The obtained specimens had an excellent finish.

5.3 Experimental details

Sound absorption and transmission loss experiments are carried out on all the 3D printed specimens through the impedance tube technique as discussed in sections 2.3.1 and section 2.3.2, respectively.

5.4 Numerical analysis

FEM simulation of varying cross-sections, constant diameter spheres, and FG spherical perforations with bubbles is conducted in the pressure acoustics module of COMSOL 5.4 to estimate SA and STL that are subsequently compared with the experimental values. This numerical model done in COMSOL Multiphysics 5.4 with only air neglects fluid-structure interaction for SA simulation. The perfectly-matched-layer (PML), specimen and an incident pressure field are modelled. In STL analysis, two extra domains, one more PML, and a transmitted pressure field are considered. The CAD modelled specimens are imported to COMSOL in a *.iges* format. PML domain perfectly absorbs all the sound energy incident on it. It is fixed at the pressure field end to prevent reflection. All boundaries are assigned the sound hard boundary wall condition. A background pressure of 1 Pascal is applied inside the pressure field domain. The material in the perforations of the imported CAD model is allocated as air from the in-built library as in earlier cases.

A user-controlled mesh is firstly defined in the model. The PML is meshed with hexahedron elements. The whole domain has meshed with free tetrahedron elements (Figures 3.2 and 4.1). Tetrahedron elements are default elements used for most applications in COMSOL Multiphysics. All 3D volumes, irrespective of topology or shape, can be easily meshed using them, even with adaptive mesh refinement. The mesh size is chosen as six elements for each wavelength corresponding to the highest frequency analyzed (Jones 2010). The lowest wavelength, which corresponds to the highest frequency, is obtained by,

$$\lambda_l = c_0/f_h \tag{5.1}$$

c_0 is the velocity of sound at given temperature, pressure conditions and f_h is the highest frequency obtained using the model.

The numerical model for getting SA includes air domains such as incident and back air gaps (25 mm). However, in the model for STL, the two air domains are the reflection and transmission space, with the specimen separating them (Figure 4.2). COMSOL acoustic pressure module is used to model the elements in the air domain. The air domain in the perforation is modeled separately using the thermo-viscous acoustic module for quantifying dissipation due to visco-thermal effects. Multiphysics coupling combines thermo-viscous and pressure acoustic physics (Zhang et al. 2015). The acoustic absorption coefficient is estimated as $\alpha = 1 - |R|^2$. Eventually, STL is obtained as,

$$STL = 10\log\left(\frac{W_{in}}{W_{out}}\right) \tag{5.2}$$

where W_{in} and W_{out} are the input and output sound power at the inlet and outlet port surface.

5.5   Results and discussion

5.5.1   Sound absorption

The influence of wood fiber on the sound absorption of PLA is shown in Figure 5.2 for specimen D. It is observed that the addition of wood fiber shifts the peak value of SAC to the low frequency side compared to the PLA case. The frequency shift is observed to be about 100 Hz and above. However, the peak value decreases, whereas bandwidth remains almost the same above $\alpha = 0.75$. Hence an overall improvement in performance is observed due to the shift in frequency to the low-frequency side when considering the aspects of sound quality enhancement and noise pollution control (Leventhall, 2004). Wood fibers in the PLA matrix have enhanced the absorption of sound waves at a lower frequency. Reflection of incident sound waves from specimen D's narrow tapered perforation path may have reduced peak value due to more reflection than pure PLA specimen.
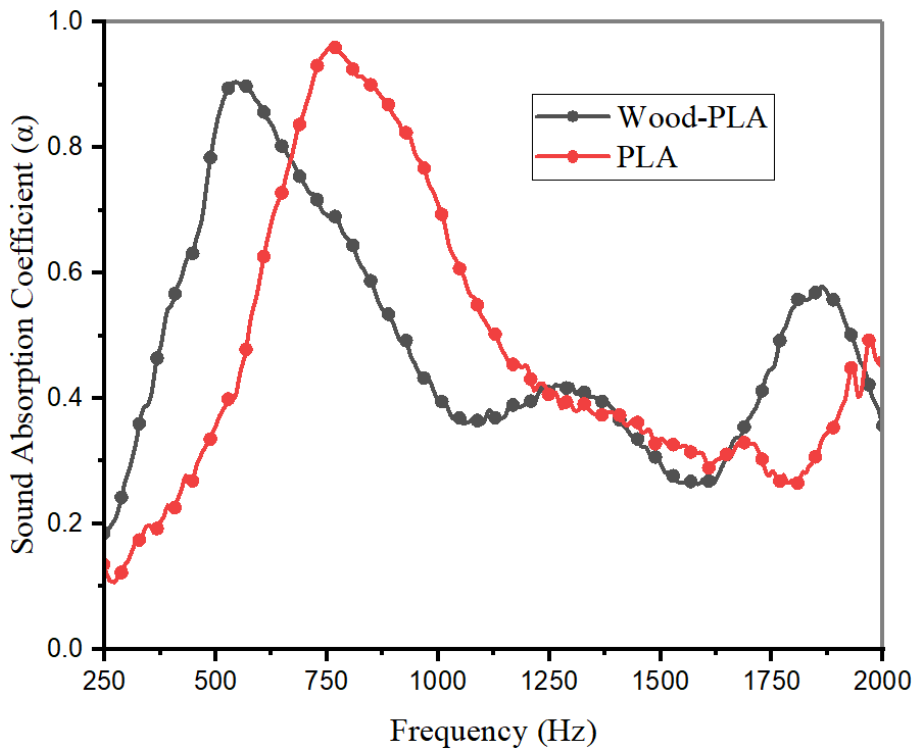
Figure 5.2: Influence of wood fibre reinforcement on SAC of D PLA specimen
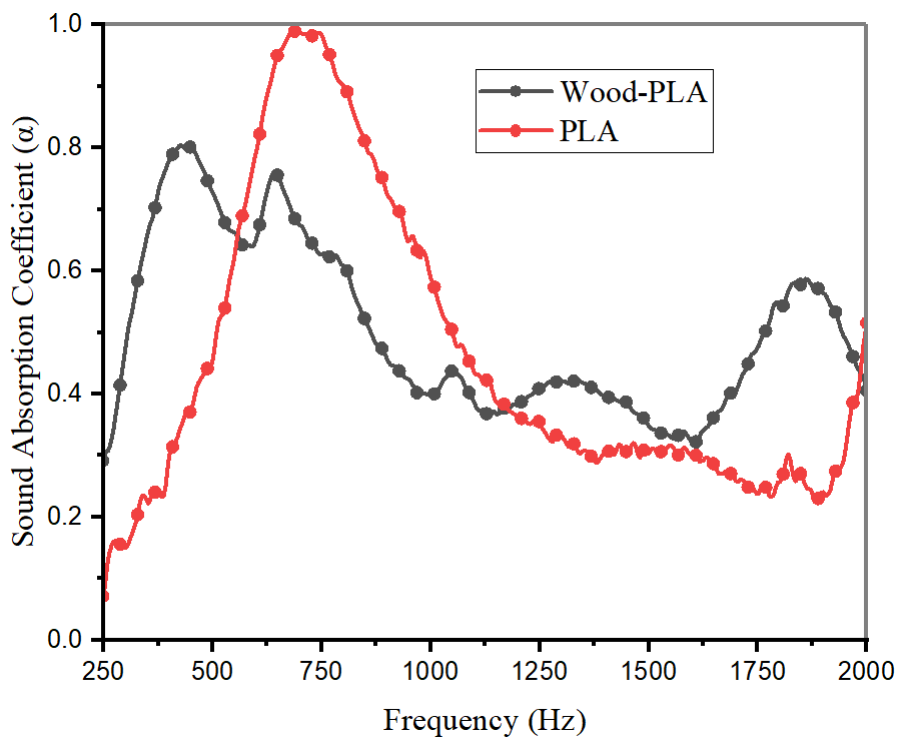
Figure 5.3: Influence of wood fibre reinforcement on SAC of DC PLA specimen.

The effect of wood fiber on the SA of PLA of the DC specimen is shown in Figure 5.3. From Figure 5.3, it is clear that the variation in SA due to the addition of wood fiber in the DC specimen is similar to specimen D. However the reduction in peak value is more than in the D case. The performance is observed to be less except for the shift in frequency to lower values. Reflection of incident sound waves from the narrow entry and shallow tapered perforation path of specimen DC may have resulted in a large reduction of peak value due to more reflection than a large reduction of peak value due to more reflection than pure PLA specimen. Furthermore, the enclosed space's entry may also be crowded with fibers at entry, enhancing higher reflection. In the case of pure PLA specimens, the enclosed spaces acted as better sound energy dissipators, as discussed in chapter 3.
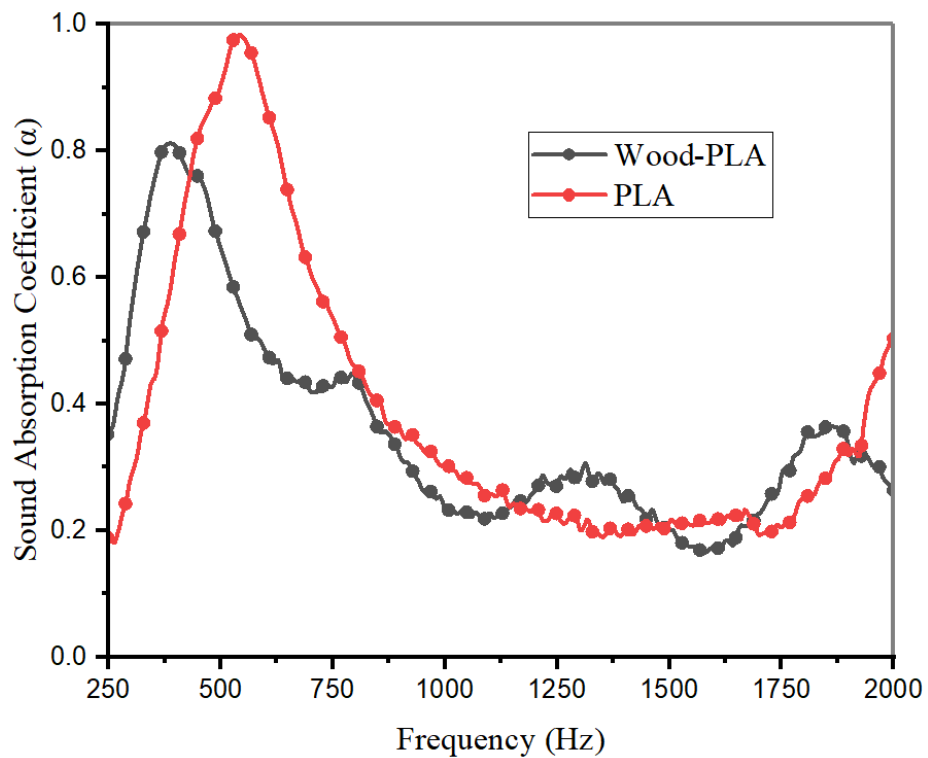
Figure 5.4: Influence of wood fibre reinforcement on SAC of C PLA specimen.

Variation in SA of the C specimen due to the addition of wood fiber is similar to the D and DC cases, as seen in Figure 5.4. However, the shift of the peak value towards the lower frequency is about 50 Hz only, unlike in the other two cases. Bandwidth decreases significantly below $\alpha = 0.75$. Here the overall performance is less except for

the shift in frequency to lower values. Even though wood fibers in the PLA matrix are expected to significantly enhance the absorption of sound waves, a reflection of incident sound waves from the entry of narrow cylindrical perforation path of specimen C may have resulted in a large reduction of peak value due to more reflection compared to pure PLA specimen. So, it can be inferred that adding wood fibers in PLA will increase wood fibers in PLA and increase the reflection of sound even in the case of a highly performing specimen like C (Sailesh et al. 2021).

The influence of wood fiber on the PLA sample with spherical perforations U2 is shown in Figure 5.5. Unlike all other cases analyzed above, i.e., samples with varying cross-sections, in this spherical perforation case, there is a significant increase in the peak value apart from the shift of peak towards the low-frequency side. Furthermore, the SA coefficient value increase is significant on the lower frequency side, which indicates that the inclusion of wood fibers in the PLA matrix has increased the absorption of sound waves. Reflection of incident sound waves from the very narrow 0.5 mm cylindrical perforation path of specimen U2 is insignificant due to a very large number of perforations compared to earlier cases. Moreover, the projected wood fibers inside
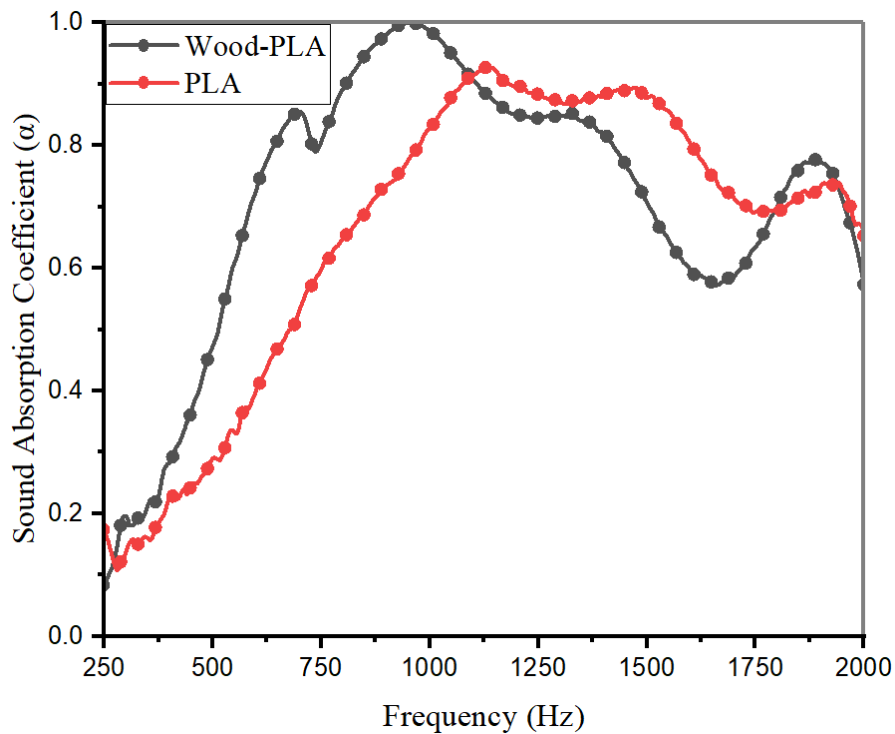
Figure 5.5: Influence of wood fibre reinforcement on SAC of U2 PLA specimen.
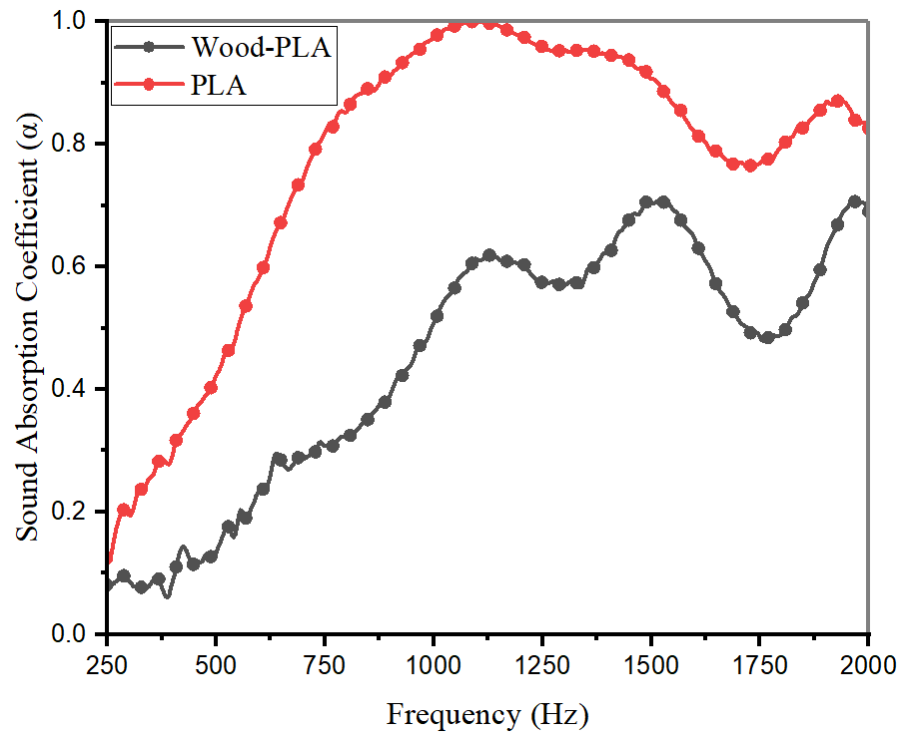
Figure 5.6: Influence of wood fibre reinforcement on SAC of U2v PLA specimen.

the spheres may have given the best dissipation with minimum reflection compared to pure PLA specimens. So, it can be concluded that adding wood fibers in PLA will increase the overall performance regarding absorption and bandwidth, especially in the low-frequency region in the case of specimen U2.

The influence of wood fiber addition on SA of PLA specimen U2v shown in Figure 5.6 indicates that the SA coefficient reduced and shifted towards the high frequency for about 250 Hz, contrary to the earlier cases discussed. Moreover, the peak value decreased significantly to $\alpha = 0.7077$ with much decrease in bandwidth. Here the performance is lower, especially in the low-frequency regions. Reflection of incident sound waves from the broad 2 mm hemispherical perforation path of specimen U2v at the incident region have remarkably influenced the absorption coefficient, resulting in a decrease compared to the pure PLA specimen and U2. Enclosed air in the bubbles of U2 provides better thermo-viscous dissipation than a loose open-air column because of
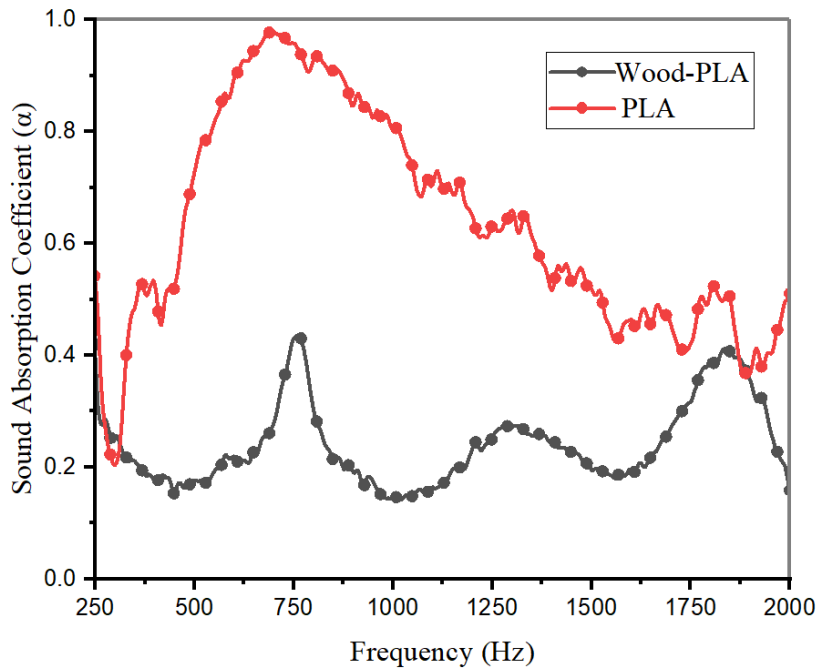
Figure 5.7: Influence of wood fibre reinforcement on SAC of FG532 PLA specimen.

the open hemispheres in the U2v sample. The compression and rarefaction in closed volumes give better dissipation when structural-fluidic interactions are taken into account, damping the oscillating sound waves more effectively. Compared to all other Wood-PLA specimens, the performance of U2v in the low-frequency region also decreased considerably. It can be inferred that adding wood fibers in PLA will decrease the overall performance regarding absorption and bandwidth, especially in the lower frequency region for specimens having a wider inlet and lesser number of perforations without a smooth divergence as in the case of the D specimen.

The inclusion of wood fiber on PLA reduces the SA coefficient of the functionally graded spherical perforation samples FG532 and FG4321, as seen in Figures 5.7 and 5.8. Accumulation of wood fiber and particles at the small necks and hollow spheres in the perforations act as barriers and narrow down the path of the propagating sound waves. Especially in the case of FG532, the curve shifted remarkably to a very low-frequency region. It formed a very similar curve like that of FG4321, which has a steeper surface gradient compared to FG532 in pure specimens. Hence, with wood fiber and powder, the paths get narrowed down. Approximately similar behavior is exhibited
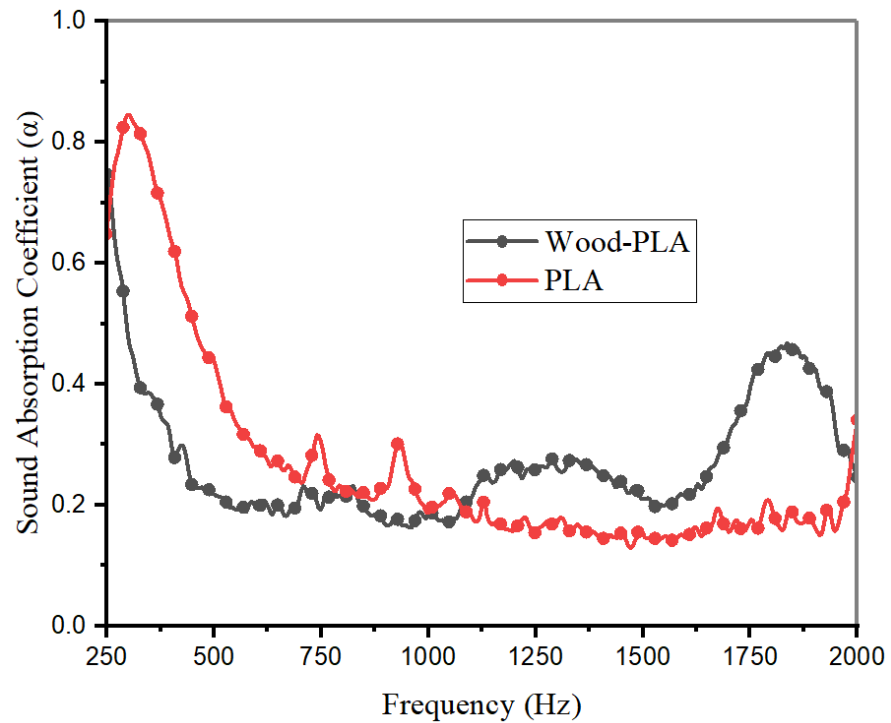
Figure 5.8: Influence of wood fibre reinforcement on SAC of FG4321 PLA specimen.

by FG532 and FG4321, who have very different characteristic graphs in the case of pure PLA specimens. Hence, the values of SA have remarkably decreased, as seen in Figure 5.7, and moderately reduced, as in Figure 5.8 in the case of FG specimens compared to earlier cases. The pattern of graphs is the same in both cases of FG532 and FG4321 wood-PLA specimens. Hence their performance improved much in the very low-frequency region. Even though the wood fiber seems to reduce the SA coefficient in general, in cases like C, DC, D, and FG4321, there is a significant increase in the SA coefficient on the lower frequency side.

In the case of wood-PLA specimens, the curve has shifted to a lower frequency region in all cases except U2v, which signifies that resonance occurs at a lower frequency due to the presence of wood in PLA. The peak value of the SA coefficient and frequency bandwidth corresponding to the SA coefficient higher than 0.75 of different samples analyzed are given in Table 5.1. Table 5.1 shows that all wood/PLA specimens except U2 have a reduction in absorption coefficient peak value due to the above mentioned reasons. Similarly, the bandwidth decreased remarkably for wood/PLA specimens

except for U2 but maintained the same order as in the pure PLA case.

Table 5.1: Frequency bandwidth and peak value of SA coefficient of different samples.

Sample	PLA		Wood-PLA	
	Peak α_{max}	Bandwidth-Hz ($\alpha > 0.75$)	Peak α_{max}	Bandwidth-Hz ($\alpha > 0.75$)
DC	0.9903	300	0.804	116
D	0.9625	320	0.9045	208
C	0.9833	215	0.8119	104
U2	0.9275	1032	0.9998	944
U2v	0.9998	1336	0.7077	-----
FG532	0.9778	640	0.6538	-----
FG4321	0.8459	116	0.7492	-----

5.5.2   Sound transmission loss
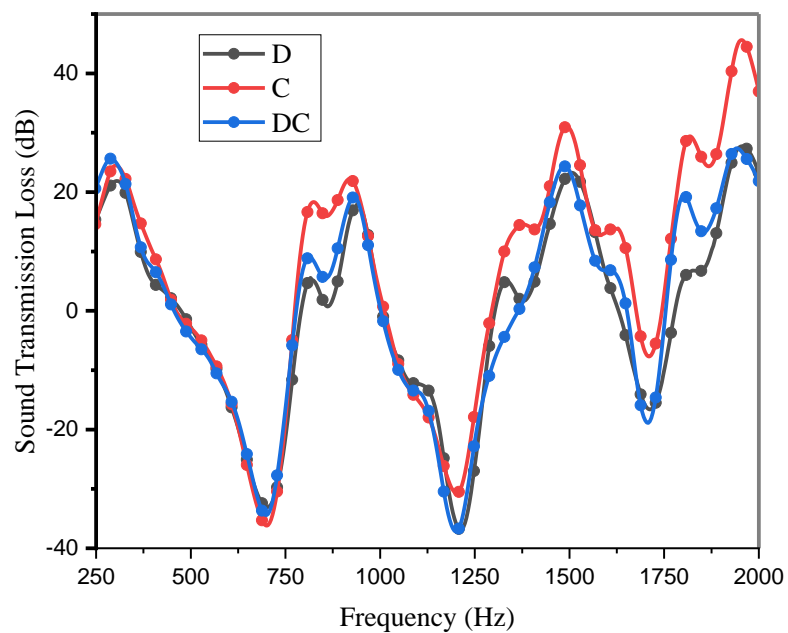
Figure 5.9: Influence of wood fibre reinforcement on STL of D, C and DC PLA specimens.

The influence of wood fiber on STL response of wood/PLA specimen is shown in Figures 5.9, 5.10, and 5.11 for samples with varying cross-sections, spherical and FG spherical samples, respectively. It is observed that the STL is improved very much at lower frequencies and gives higher values due to shift of the resonance region to the lower frequency side. All the specimens produced reasonable transmission loss in the same range up to 25 dB. However, as shown in Figure 16, the FG specimens performed better than their uniform spherical counterparts as in the case of the pure PLA specimens due to the combined effect of stepping and convergence and the usual dissipation phenomenon.
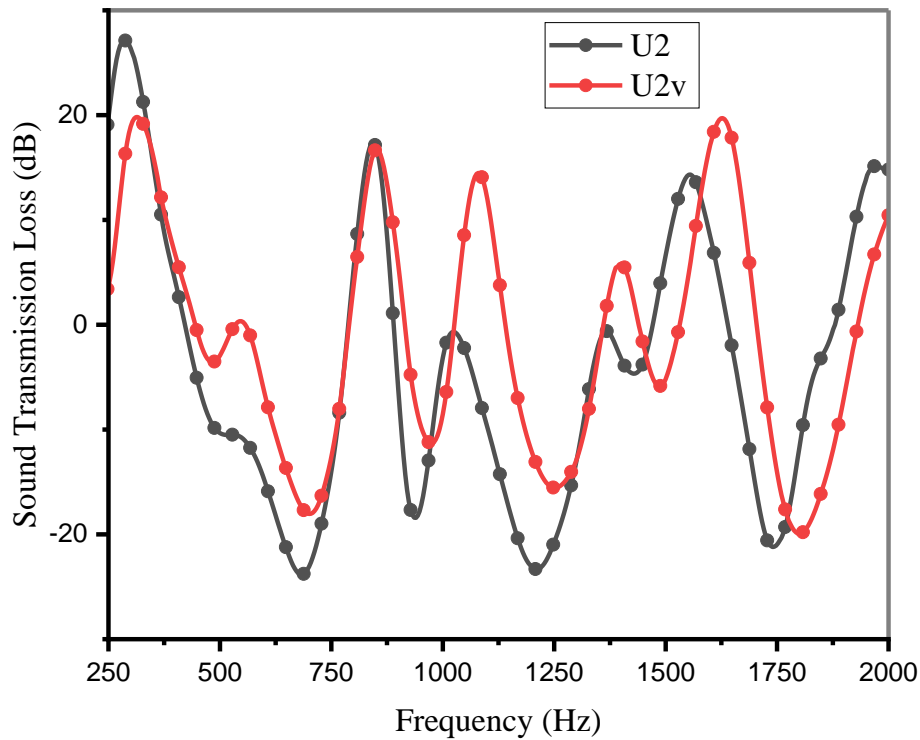
Figure 5.10: Influence of wood fibre reinforcement on STL of U2 and U2v PLA specimens.

Closer streamlines in longer boundary layers account for heavier dissipation. The curvatures, narrow entries, narrow exits, sudden expansions, and sudden contractions induce tortuosity and scattering. Long, tortuous paths dissipate more energy. Further, enclosed air in closed spaces with narrow inlets and exits might be better sound energy dissipators. All the necks in the paths act as bottlenecks dissipating further energy. Moreover, solid-fluid interactions, not accounted for in the numerical modelling, are

significantly higher for wood-PLA specimens with rough, porous surfaces inside the perforations than pure PLA specimens.

In the FG wood-PLA samples, the frequency range of higher absorption drops down to 300 Hz, which effectively dissipates the human voice. Major effects of sound pollution on most living beings come below 1000 Hz (Leventhall et al. 2004). Thus, FG wood-PLA specimens fare better in practical applications compared to other samples.
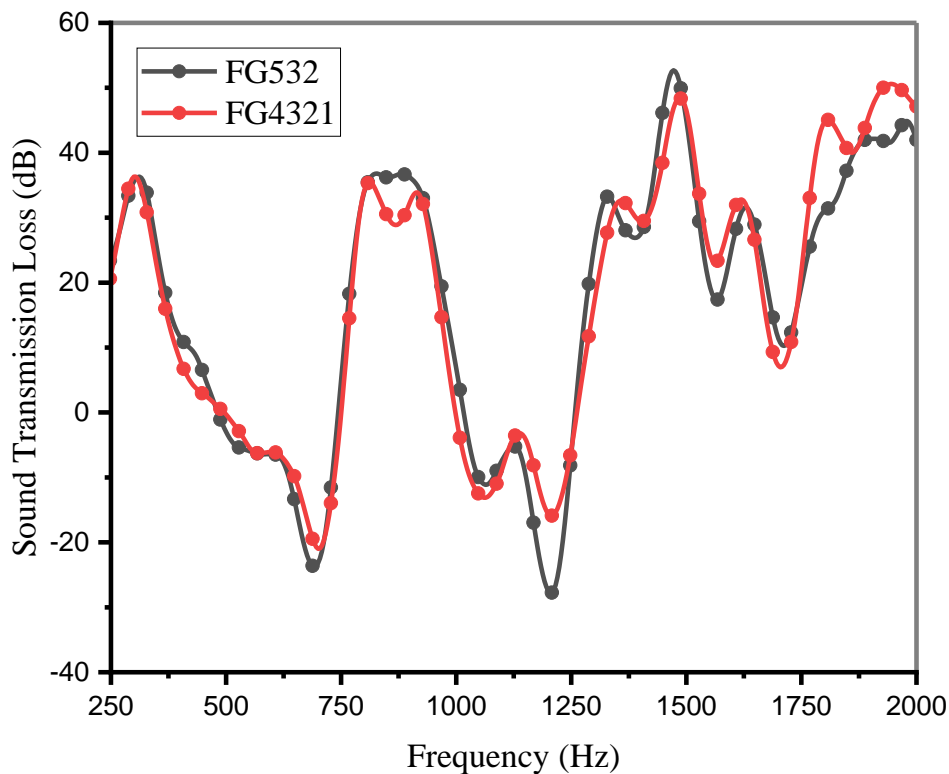
Figure 5.11: Influence of wood fibre reinforcement on STL of FG532 and FG4321 PLA specimens.

There is a continuous pulsation in the STL curves observed in the STL plots. Oscillation in the STL curve has been reported in many literatures. Examples of such oscillations can be observed in experimental studies of (Moore and Lyon 1991), (Wang et al. 2005) and (Arslan et al. 2020). The ripples in the curves cannot be avoided completely in any practical setup. Nevertheless, it can be minimized using high-quality components and accessories to the best possible extent. Most of the impedance tube material is metal to avoid vibration transmission, whereas, in this study, a tube made of acrylic is used to avoid vibration. Adequate damping is provided for the test setup which is ensured since

no oscillations are observed in SA curves. So, the impedance tube doesn't cause much oscillation in the STL curves.

A number of trials are done to obtain optimum readings for the experiment under a controlled lab environment with minimum error. The anechoic termination is obtained in the impedance tube with polyurethane foam thickness of 100 mm and an SA coefficient of 0.95 approximately. Oscillation in the STL curves also results from imperfect anechoic termination. Pispola et al. (2005) report that oscillation in the STL curve is caused by anechoic termination by high porosity material having limited flow resistivity. Maybe, more thickness of the anechoic terminator will reduce the fluctuating trend. The edges of the test sample are properly taped using teflon until it fits tightly in the impedance tube to avoid sound leakage between upstream and downstream. The tight fit of specimen attribute oscillations in STL curves (Kino and Ueno 2007). Specimen vibration also causes additional resonance peaks in sound attenuation characteristics (Tayong et al. 2010).

5.5.3   Comparison of experimental and numerical results

This section compares SA and STL results obtained using the impedance tube method with the numerical results obtained using FEM software COMSOL for selected cases. The air domain within all perforations is modeled using the thermos-viscous acoustic module in COMSOL, which accounts for both viscous and thermal loss and provides a simplified, accurate procedure for obtaining parameters such as temperature variations and sound velocity and acoustic pressure. Structural-fluidic interaction is completely neglected to simplify this model. This model constitutes an inlet port, outlet port, and intermediary part that depends on the perforation's geometry. Acoustic processes inside each perforation are modeled using the thermos-viscous module of COMSOL, doing a complete analysis of viscous and thermal dissipation.

The results are compared for C, FG4321, and FG532 wood/PLA samples in Figures 5.12, 5.13, and 5.14, respectively. Numerical results obtained are compared against experimental ones for both SA and STL. Patterns obtained in FEM simulation results are similar to the experimental ones for all the cases with a shift in frequency towards
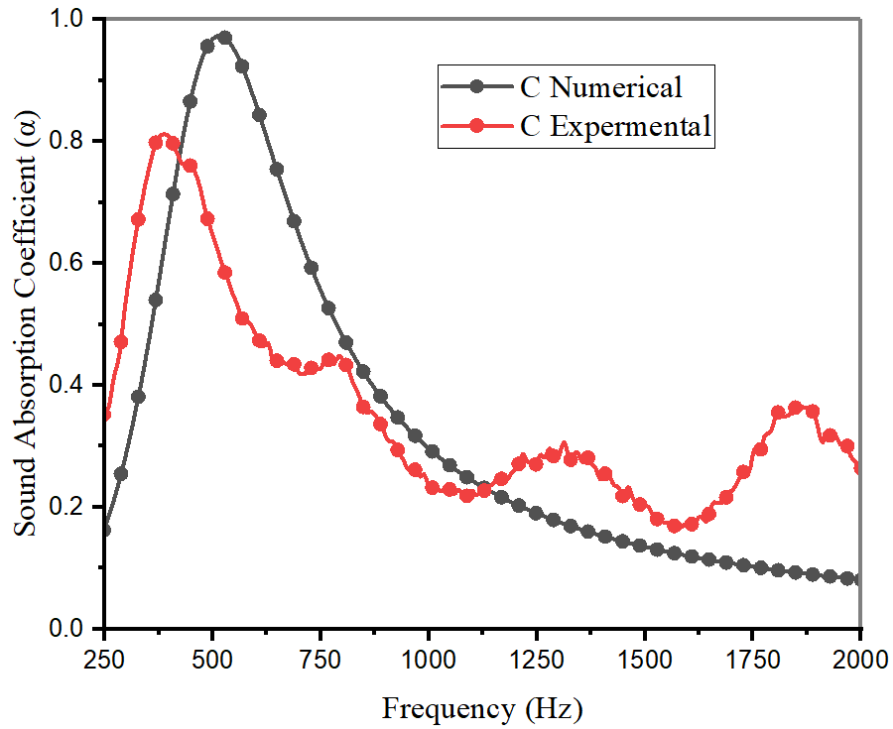
Figure 5.12: Comparison of experimental and numerical SAC of specimen C made of wood-PLA.
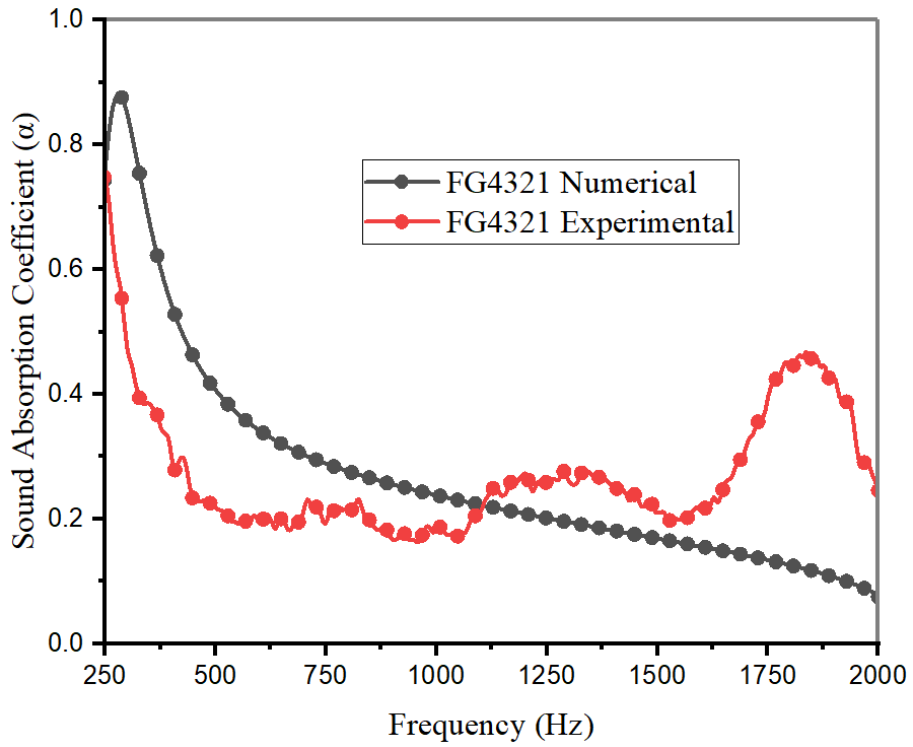
Figure 5.13: Comparison of experimental and numerical SAC of specimen FG4321 made of wood-PLA.

78
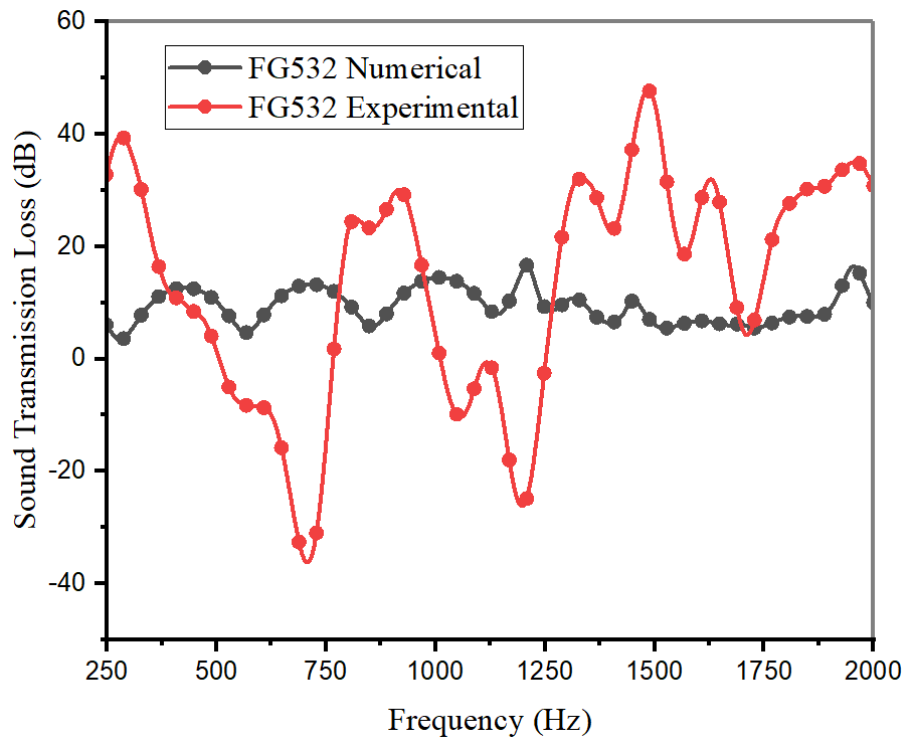
Figure 5.14: Comparison of experimental and numerical STL of specimen FG532 made of Wood-PLA.

the lower side (Figure 5.12-5.14). Simulated and experimental results, including resonant frequencies, has this shift in all cases justified by solid-fluid friction, which is completely neglected in the numerical analysis. Nevertheless, the experimental results overpredict near the ends of the frequency axis. This may be caused by non-compliance with assumptions such as the specimen having perfect rigidity, and the whole surface is perfectly finished. But actually, they are non-rigid solids with rough surfaces, which always intensify frictional interactions and viscothermal dissipations at the solid-fluid interface, thereby increasing the sound absorptivity. The samples made of wood-PLA may have deviated from the above assumptions due to increased porosity, higher friction, and roughness due to the presence of wood powder.

The STL plot of numerical and experimental values of FG532 specimen is shown in Figure 5.14. The experimental results have oscillations in the numerical curve. However, it deviates both sides maintaining a mean average nearer to the numerical results. Ripples found in STL graphs obtained through experiment cannot be completely averted as the setup is always prone to errors and vibration. High quality

components reduce these fluctuations usually found in these STL plots. An acrylic tube along with required damping is used to avoid ripples. A number of tests are carried out to obtain the most optimized values. A cylindrical polyurethane foam piece of 100 mm thickness and an α value of approximately 0.95 is used in the tube to carry out anechoic termination. Imperfection in the termination will also cause oscillations in STL graphs. Pispola et al. (2005) report oscillations in STL graphs caused due to a high porosity material of limited flow resistivity. Teflon tape is wound tightly on the sample edges to ward off any sound leakage. This tight fit sample also adds to ripples in the STL curve.

5.6   Conclusion

A study on SA and STL properties of wood/PLA specimens of perforations with varying cross-sections and spherical and FG spherical geometry has been carried out, and the following conclusions can be drawn.

3D printing of wood/PLA specimens with perforations of especially small dimensions with spheres was highly challenging even with pure PLA due to the required accuracy and precision. Frequent clogging of nozzles further complicated the process, and a total of 250 hours were required, especially due to wood specimens with low mm range perforations. Among all the specimens', improved performance was shown by specimen U2, both in terms of SA and STL. All specimens made of wood/PLA performed better in SA in the low-frequency region than pure PLA specimens. STL characteristics of FG spherical specimens increased significantly with wood PLA material, whereas with constant diameter spherical perforations, the performance is at par with pure PLA specimens. Wood fibers blocked and reflected much of sound energy, especially when the incident entry is larger.

6. SUMMARY AND CONCLUSIONS

6.1   Summary

A comprehensive study has been carried out to analyze the sound absorption, and transmission loss characteristics of varying cross-sections and functionally graded perforations made of PLA and PLA reinforced with wood fiber. The use of environmentally friendly PLA and wood reinforced PLA will help replace all petrochemical-based polymers and hazardous materials like glass wool, rock wool, and PU foams currently used in acoustic applications. Production and market share of PLA are increasing at an exponential rate worldwide. The latest 3D printing techniques have enhanced intricacy, accuracy, precision, and resolution to a remarkable extent. The influence of these techniques has brought remarkable development to Acoustics.

Thick microperforated panels having reasonable strength and stiffness with perforations of varying cross-sections that enhance sound energy's dissipation in terms of absorption and transmission loss were studied. Among them, DC perforation exceeded the peak value of absorption, and all other cross-sections had very high bandwidth compared to a standard constant diameter perforation. Transmission losses of two perforations, DC and D, were comparable with the standard perforation. Analysis was done with boundary layer diagrams, and numerical results were validated with experimental ones reasonably.

Functionally graded perforations having series connected spheres with varying diameters were studied. A comparison was made with series connected constant diameter spheres and cylindrical specimens. The FG perforations were superior in sound absorptions at low frequencies and had a good STL response compared to other specimens. The best specimens out of the above two studies were fabricated with wood fiber reinforced PLA. Only one specimen, U2 was better in terms of both peak value and bandwidth. Nevertheless, all specimens shifted the peak value to a lower frequency range favorable to living beings. All the results were compared with numerical ones and found to comply.

6.2   Conclusions

The important conclusions are summarised as;

Sound absorption and Sound Transmission loss properties of MPPs with varying cross-sections

➢ Geometrical variations of perforations influence the energy dissipation of sound significantly.

➢ DC perforation registered better SA performance than the constant 1 mm diameter perforation pertaining to peak value and bandwidth.

➢ All other perforations depicted less peak value amid comparable values for a constant diameter of 1 mm.

➢ Bandwidths covered by all other perforations for a given range of absorption coefficients were higher than Const 1.

➢ Sound transmission losses are comparable to Const 1, especially where the entry point of perforation is small.

➢ Const 1, DC, and D perforations result in very low sound transmission.

➢ The MPPs studied are excellent in sound absorption and have a reasonably good dissipating power during sound transmission.

Sound absorption and sound transmission loss properties of spherical perforations connected in series.

➢ The influence of spherical bubbles' size and its grading pattern on SA and STL behavior is significant.

➢ In uniform diameter bubble specimens, smaller spherical bubbles result in a better SA coefficient.

➢ FG532 perforations enhanced SA performance in the lower frequencies up to 1000 Hz in a functionally graded case.

➢ The STL response of FG4321 and FG4321R specimens is better than the other cases.

➢ Narrow perforations perform better in SA and STL characteristics since the dissipation is better due to closer streamlines, greater perforations per unit area, and higher porosity.

➤ Thus, spherical perforations with both uniform and graded porosity can be tailored for applications dissipating a wide range of desired frequencies, thereby controlling noise pollution.

Sound absorption and sound transmission loss properties of specimens 3D printed with wood/PLA material.

➤ Frequent clogging of nozzles further complicated the process, and total 250 hours were required, especially due to specimens with low mm range perforations.

➤ Among all the specimens', improved performance was shown by specimen U2, both in terms of SA and STL.

➤ All specimens made of wood/PLA performed better in SA in the low frequency region than pure PLA specimens.

➤ STL characteristics of FG spherical specimens increased significantly with wood PLA material, whereas with constant diameter spherical perforations, the performance is at par with pure PLA specimens.

➤ Wood fibers blocked and reflected much of sound energy, especially when the incident entry is larger.

The whole work successfully asserts the usage of bio-degradable material for acoustic panels, which can be produced with intricate and complicated perforations by the latest 3D printing techniques at a reasonable cost. The results also illustrate the effectiveness of these panels in controlling noise pollution and enhancing sound quality. Thus, this study paves a stepping stone to the effective utilisation of green materials in acoustics, thereby preserving our environment and invaluable petroleum products.

SCOPE OF FUTURE WORK

In the present research work, acoustic characteristics of perforations with varying cross-sections and functionally graded perforations that employ green materials like PLA and wood/PLA have been carried out. A number of possibilities exist with perforations having different geometric variations in thick panels, which can be achieved to desired intricacy, accuracy, and surface finish by the latest additive manufacturing techniques. Apart from FDM, which is used to fabricate specimens in this work, other additive manufacturing techniques may also be studied with green materials other than PLA. Fire retardant studies have not been carried out on both PLA and wood/PLA, which offers scope for study.

Appendix I

The binding equations and calculations for the numerical model are as shown below (C Sujatha 2010).

Calculation of sound absorption coefficient:

For normal incidence case, the incident pressure can be written as

$$P_{in} = A_{in} e^{j(\omega t - k_0 z)} \tag{1}$$

where A_{in} is the amplitude of incident sound pressure, ω is the frequency, and k_0 is the wavenumber. Similarly, the reflected pressure can be written as

$$P_r = A_r e^{j(\omega t + k_0 z)} \tag{2}$$

where, A_r is the amplitude of reflected sound pressure. The sound power reflection coefficient (R) can be written as

$$\alpha_R = \left| \frac{A_r}{A_{in}} \right|^2 \tag{3}$$

Let, $R = \dfrac{A_r}{A_{in}}$ Then, the sound absorption coefficient is calculated by

$$\alpha = 1 - |R|^2 \tag{4}$$

Calculation of sound transmission loss coefficient:

The transmitted pressure can be written as

$$P_t = A_t e^{j(\omega t - k_0 z)} \tag{5}$$

The sound pressure and power can be related in terms of sound intensity using the relation,

$$W = \oint_S I dS \quad \text{where, } S \text{ is the surface area common to the two media.} \tag{6}$$

$$I = \frac{P^2}{Z_0} \tag{7}$$

Where I is the intensity of sound and $Z_0 = \rho_0 c_0$; ρ_0 = Density of air and c_0 = Speed of sound in air.

Hence the sound power transmission coefficient can be written in terms of sound intensity as

$$\tau = \frac{P_t^2}{P_{in}^2} = \left| \frac{A_t}{A_{in}} \right|^2 = \frac{W_{out}}{W_{in}} \tag{8}$$

Then, the sound transmission loss can be written as

$$STL = 10 \log \left(\frac{W_{in}}{W_{out}} \right) = 10 \log \left(\frac{1}{\tau} \right) \tag{9}$$

REFERENCES

Abdel-Hakim, A., El-Basheer, T. M., Abd El-Aziz, A. M., and Afifi, M. (2021). "Acoustic, ultrasonic, mechanical properties and biodegradability of sawdust/ recycled expanded polystyrene eco-friendly composites." *Polymer Testing*, 99, 107215.

Abdi, D. D., Monazzam, M., Taban, E., Putra, A., Golbabaei, F., and Khadem, M. (2021). "Sound absorption performance of natural fiber composite from chrome shave and coffee silver skin." *Applied Acoustics*, 182, 108264.

Akiwate, D. C., Date, M. D., and Venkatesham, B. (2019a). "Acoustic measurement of additive manufactured concentric tube reverse flow resonators." *Mechanics of Advanced Materials and Structures*, 26(1), 56-61.

Akiwate, D. C., Date, M. D., Venkatesham, B., and Suryakumar, S. (2019b). "Acoustic characterization of additive manufactured perforated panel backed by honeycomb structure with circular and non-circular perforations." *Applied Acoustics*, 155, 271-279.

Alshehrei, F. (2017). "Biodegradation of synthetic and natural plastic by microorganisms." *Journal of Applied and Environmental Microbiology*, 5(1), 8-19.

An, X., Lai, C., Fan, H., and Zhang, C. (2020). "3D acoustic metamaterial-based mechanical metalattice structures for low-frequency and broadband vibration attenuation." *International Journal of Solids and Structures*, 191–192, 293-306.

Arslan, H., Ranjbar, M., Secgin, E., and Celik, V. (2020). "Theoretical and experimental investigation of acoustic performance of multi-chamber reactive silencers." *Applied Acoustics*, 157, 106987.

ASTM E2611-09, *Standard Test Method for Measurement of Normal Incidence Sound Transmission of Acoustical Materials Based on the Transfer Matrix Method*, ASTM International, West Conshohocken, PA, USA.

ASTM E1050-19, *Standard Test Method for Impedance and Absorption of Acoustical Materials Using a Tube, Two Microphones and a Digital Frequency Analysis System*, ASTM International, West Conshohocken, PA, USA.

Attenborough, K. (2019). "Macro-and micro-structure designs for porous sound absorbers." *Applied Acoustics*, 145, 349-357.

Auriemma, F. (2017). "Acoustic performance of micro-grooved elements." *Applied Acoustics*, 122, 128-137.

Ayrilmis, N. (2018). "Effect of layer thickness on surface properties of 3D printed materials produced from wood flour/PLA filament." *Polymer Testing*, 71, 163-166.

Ayrilmis, N., Kariz, M., and Kitek Kuzman, M. (2019b). "Effect of wood flour content on surface properties of 3D printed materials produced from wood flour/PLA filament." *International Journal of Polymer Analysis and Characterization*, 24(7), 659-666.

Ayrilmis, N., Kariz, M., Kwon, J. H., and Kitek Kuzman, M. (2019a). "Effect of printing layer thickness on water absorption and mechanical properties of 3D-printed wood/PLA composite materials." *The International Journal of Advanced Manufacturing Technology*, 102(5), 2195-2200.

Ayrilmis, N., Kariz, M., Sernek, M., and Kuzman, M. K. (2021). "Effects of sandwich core structure and infill rate on mechanical properties of 3D-printed wood/PLA composites." *The International Journal of Advanced Manufacturing Technology*, 115(9), 3233-3242.

Ayrilmis, N., Nagarajan, R., and Kuzman, M. K. (2020). "Effects of the face/core layer ratio on the mechanical properties of 3D printed wood/polylactic acid (PLA) green biocomposite panels with a gyroid core." *Polymers*, 12(12), 2929.

Baferani, A. H., Katbab, A. A., and Ohadi, A. R. (2017). "The role of sonication time upon acoustic wave absorption efficiency, microstructure, and viscoelastic behavior of

flexible polyurethane/CNT nanocomposite foam." *European Polymer Journal*, 90, 383-391.

Bhagia, S., Lowden, R. R., Erdman III, D., Rodriguez Jr, M., Haga, B. A., Solano, Ines Roxanne M Gallego, N.C., Pu, Y., Muchero, W., Kunc, V. and Ragauskas, A. J. (2020). "Tensile properties of 3D-printed wood-filled PLA materials using poplar trees." *Applied Materials Today*, 21, 100832.

Biot, M. A. (1962). "Generalized theory of acoustic propagation in porous dissipative media." *The Journal of the Acoustical Society of America*, 34(9A), 1254-1264.

Boulvert, J., Costa-Baptista, J., Cavalieri, T., Perna, M., Fotsing, E. R., Romero-García, V., Gwenael Gabard, Annie Ross, Jacky Mardjono and Groby, J. P. (2020). "Acoustic modeling of micro-lattices obtained by additive manufacturing." *Applied Acoustics*, 164, 107244.

Cai, X., Yang, J., Hu, G., and Lu, T. (2018). "Sound absorption by acoustic microlattice with optimized pore configuration." *The Journal of the Acoustical Society of America*, 144(2), EL138-EL143.

Carlier, E., Marquette, S., Peerboom, C., Denis, L., Benali, S., Raquez, J. M., Amighi, K., and Goole, J. (2019). "Investigation of the parameters used in fused deposition modeling of poly (lactic acid) to optimize 3D printing sessions." *International Journal of Pharmaceutics*, 565, 367-377.

Carpio, A. R., Avallone, F., Ragni, D., Snellen, M., and van der Zwaag, S. (2020). "Quantitative criteria to design optimal permeable trailing edges for noise abatement." *Journal of Sound and Vibration*, 485, 115596.

Cherradi, Y., Rosca, I. C., Cerbu, C., Kebir, H., Guendouz, A., and Benyoucef, M. (2021). "Acoustic properties for composite materials based on alfa and wood fibers." *Applied Acoustics*, 174, 107759.

Chin, D. D. V. S., Yahya, M. N. B., Din, N. B. C., and Ong, P. (2018). "Acoustic properties of biodegradable composite micro-perforated panel (BC-MPP) made from kenaf fibre and polylactic acid (PLA)." *Applied Acoustics*, 138, 179-187.

Deshmukh, S., Ronge, H., and Ramamoorthy, S. (2019). "Design of periodic foam structures for acoustic applications: Concept, parametric study and experimental validation." *Materials and Design*, 175, 107830.

Dong, Y., Milentis, J., and Pramanik, A. (2018). "Additive manufacturing of mechanical testing samples based on virgin poly (lactic acid)(PLA) and PLA/wood fibre composites." *Advances in Manufacturing*, 6(1), 71-82.

Droz, C., Robin, O., Ichchou, M., and Atalla, N. (2019). "Improving sound transmission loss at ring frequency of a curved panel using tunable 3D-printed small-scale resonators." *The Journal of the Acoustical Society of America*, 145(1), EL72-EL78.

Ecker, J. V., Haider, A., Burzic, I., Huber, A., Eder, G., and Hild, S. (2019). "Mechanical properties and water absorption behaviour of PLA and PLA/wood composites prepared by 3D printing and injection moulding." *Rapid Prototyping Journal*, 25(4), 672–678.

Eynde, M. Van den, and Puyvelde, P. Van. (2018). "3D Printing of Poly(lactic acid)." *Advances in Polymer Science*, 282, 139–158.

Ezzaraa, I., Ayrilmis, N., Kuzman, M. K., Belhouideg, S., and Bengourram, J. (2020). "Study of the effects of microstructure on the mechanical properties of 3D printed wood/PLA composite materials by a micromechanical approach." *2020 International Conference on Electronics, Control, Optimization and Computer Science, ICECOCS 2020*, 7–11.

Farah, S., Anderson, D. G., and Langer, R. (2016). "Physical and mechanical properties of PLA, and their functions in widespread applications—A comprehensive review." *Advanced Drug Delivery Reviews*, 107, 367-392.

Fotsing, E. R., Dubourg, A., Ross, A., and Mardjono, J. (2019). "Acoustic properties of periodic micro-structures obtained by additive manufacturing." *Applied Acoustics*, 148, 322-331.

Gao, N., and Hou, H. (2018). "Sound absorption characteristic of micro-helix metamaterial by 3D printing." *Theoretical and Applied Mechanics Letters*, 8(2), 63-67.

Ghaffari, S., Khalid, S., Butler, M., and Naguib, H. E. (2015). "Development of high thermally conductive and electrically insulative polylactic acid (PLA) and hexagonal boron nitride (hBN) composites for electronic packaging applications." *Journal of Biobased Materials and Bioenergy*, 9(2), 145-154.

Ghermezgoli, Z. M., Moezzi, M., Yekrang, J., Rafat, S. A., Soltani, P., and Barez, F. (2021). "Sound absorption and thermal insulation characteristics of fabrics made of pure and crossbred sheep waste wool." *Journal of Building Engineering*, 35, 102060.

Hariprasad, K., Ravichandran, K., Jayaseelan, V., and Muthuramalingam, T. (2020). "Acoustic and mechanical characterisation of polypropylene composites reinforced by natural fibres for automotive applications." *Journal of Material Research and Technology*, 9(6), 14029–14035.

Herdtle, T., Stuart Bolton, J., Kim, N. N., Alexander, J. H., and Gerdes, R. W. (2013). "Transfer impedance of microperforated materials with tapered holes." *The Journal of the Acoustical Society of America*, 134(6), 4752-4762.

Hentati, T., Bouazizi, L., Taktak, M., Trabelsi, H., and Haddar, M. (2016). "Multi-levels inverse identification of physical parameters of porous materials." *Applied Acoustics*, 108, 26-30.

Hoang, M. T., Bonnet, G., Tuan Luu, H., and Perrot, C. (2014). "Linear elastic properties derivation from microstructures representative of transport parameters." *The Journal of the Acoustical Society of America*, 135(6), 3172-3185.

Hong, M., and Chen, E. Y. X. (2017). "Chemically recyclable polymers: a circular economy approach to sustainability." *Green Chemistry*, 19(16), 3692-3706.

Huang, W., Zhang, H., Inman, D. J., Qiu, J., Cesnik, C. E., and Ji, H. (2019). "Low reflection effect by 3D printed functionally graded acoustic black holes." *Journal of Sound and Vibration*, 450, 96-108.

Huda, M. S., Drzal, L. T., Mohanty, A. K., and Misra, M. (2008). "Effect of fiber surface-treatments on the properties of laminated biocomposites from poly(lactic acid) (PLA) and kenaf fibers." *Composites Science and Technology*, 68(2), 424–432.

Jiang, C. S., Li, X. H., Cheng, W. Y., Luo, Y., and Xing, T. (2020). "Acoustic impedance of microperforated plates with stepwise apertures." *Applied Acoustics*, 157, 106998.

Jiang, J., and Li, Y. (2018). "Review of active noise control techniques with emphasis on sound quality enhancement." *Applied Acoustics*, 136, 139-148.

Jiang, J., Gu, H., Li, B., and Zhang, J. (2021). "Preparation and properties of straw/PLA wood plastic composites for 3D printing." *IOP Conference Series: Earth and Environmental Science*, 692(3), 032004.

Jones, P. W. (2010). "Prediction of the acoustic performance of small poroelastic foam filled mufflers: A case study." *Acoustics Australia*, 38(2), 69–75.

Kain, S., Ecker, J. V., Haider, A., Musso, M., and Petutschnigg, A. (2020). "Effects of the infill pattern on mechanical properties of fused layer modeling (FLM) 3D printed wood/polylactic acid (PLA) composites." *European Journal of Wood and Wood Products*, 78(1), 65-74.

Karamanlioglu, M., Preziosi, R., and Robson, G. D. (2017). "Abiotic and biotic environmental degradation of the bioplastic polymer poly (lactic acid): A review." *Polymer Degradation and Stability*, 137, 122-130.

Kariz, M., Sernek, M., and Kuzman, M. K. (2018). "Effect of humidity on 3D-printed specimens from wood-PLA filaments." *Wood Research*, 63(5), 917-922.

Kennedy, J., Flanagan, L., Dowling, L., Bennett, G. J., Rice, H., and Trimble, D. (2019). "The influence of additive manufacturing processes on the performance of a periodic

acoustic metamaterial." *International Journal of Polymer Science*, 2019, Article ID 7029143, 1-11.

Kino, N., and Ueno, T. (2007). "Investigation of sample size effects in impedance tube measurements." *Applied Acoustics*, 68(11-12), 1485-1493.

Knez, N., Kariz, M., Knez, F., Ayrilmis, N., and Kuzman, M. K. (2021). "Effects of Selected Printing Parameters on the Fire Properties of 3D-Printed Neat Polylactic Acid (PLA) and Wood/PLA Composites." *Journal of Renewable Materials*, 9(11), 1883-1895.

Kumar, S., Xiang, T. B., and Lee, H. P. (2020). "Ventilated acoustic metamaterial window panels for simultaneous noise shielding and air circulation." *Applied Acoustics*, 159, 107088.

Kuzman, M. K., Ayrilmis, N., Sernek, M., and Kariz, M. (2019). "Effect of selected printing settings on viscoelastic behaviour of 3D printed polymers with and without wood." *Materials Research Express*, 6(10), 105362.

Leventhall, H. G. (2004). "Low frequency noise and annoyance." *Noise and Health*, 6(23), 59.

Levin, B. C. (1987). "A summary of the NBS literature reviews on the chemical nature and toxicity of the pyrolysis and combustion products from seven plastics: Acrylonitrile–butadiene–styrenes (ABS), nylons, polyesters, polyethylenes, polystyrenes, poly (vinyl chlorides) and rigid polyurethane foams." *Fire and Materials*, 11(3), 143-157.

Liu, C., Xia, B., and Yu, D. (2017a). "The spiral-labyrinthine acoustic metamaterial by coiling up space." *Physics Letters A*, 381(36), 3112-3118.

Liu, J., and Herrin, D. W. (2010). "Enhancing micro-perforated panel attenuation by partitioning the adjoining cavity." *Applied Acoustics*, 71(2), 120-127.

Liu, J., Hua, X., and Herrin, D. W. (2014). "Estimation of effective parameters for microperforated panel absorbers and applications." *Applied Acoustics*, 75, 86-93.

Liu, Z., Zhan, J., Fard, M., and Davy, J. L. (2017b). "Acoustic properties of multilayer sound absorbers with a 3D printed micro-perforated panel." *Applied Acoustics*, 121, 25-32.

Maa, D. Y. (1975) "Theory and Design of Microperforated Panel Sound-absorbing Constructions.", *Scientia Sinica,* 18, 55-71.

Maa, D. Y. (1987) "Microperforated-Panel Wideband Absorbers." *Noise Control Engineering Journal,* 29(3), 77-84.

Maa, D. Y. (1998) "Potential of microperforated panel Absorber." *The Journal of the Acoustical Society of America,* 104(5), 2861-2866.

Mamtaz, H., Fouladi, M. H., Nuawi, M. Z., Namasivayam, S. N., Ghassem, M., and Al-Atabi, M. (2017). "Acoustic absorption of fibro-granular composite with cylindrical grains." *Applied Acoustics*, 126, 58-67.

McKenna, S. T., and Hull, T. R. (2016). "The fire toxicity of polyurethane foams." *Fire Science Reviews*, 5(1), 1-27.

Mehrzad, S., Taban, E., Soltani, P., Samaei, S. E., and Khavanin, A. (2022). "Sugarcane bagasse waste fibers as novel thermal insulation and sound-absorbing materials for application in sustainable buildings." *Building and Environment*, 211, 108753.

Meng, H., Galland, M. A., Ichchou, M., Xin, F. X., and Lu, T. J. (2019). "On the low frequency acoustic properties of novel multifunctional honeycomb sandwich panels with micro-perforated faceplates." *Applied Acoustics*, 152, 31-40.

Moore, J. A., and Lyon, R. H. (1991). "Sound Transmission Loss Characteristics Of Sandwich Panel Constructions." *The Journal of the Acoustical Society of America*, 89(2), 777–791.

Mosa, A. I., Putra, A., Ramlan, R., and Esraa, A. A. (2020). "Wideband sound absorption of a double-layer microperforated panel with inhomogeneous perforation." *Applied Acoustics*, 161, 107167.

Mosanenzadeh, S. G., Doutres, O., Naguib, H. E., Park, C. B., and Atalla, N. (2015). "A numerical scheme for investigating the effect of bimodal structure on acoustic behavior of polylactide foams." *Applied Acoustics*, 88, 75-83.

Nampoothiri, K. M., Nair, N. R., and John, R. P. (2010). "An overview of the recent developments in polylactide (PLA) research." *Bioresource Technology*, 101(22), 8493-8501.

Nam Y. J., Ray Sinha S., and Okamoto, M. (2003). "Crystallization Behavior and Morphology of Biodegradable Polylactide/Layered Silicate Nanocomposite", *Macromolecules,* 36(19), 7126-7131.

Netravali N. A. and Chabba S. (2003). "Composites get greener", *Materials Today*, 6(4), 22-29.

Ning, J. F., Ren, S. W., and Zhao, G. P. (2016). "Acoustic properties of micro-perforated panel absorber having arbitrary cross-sectional perforations." *Applied Acoustics*, 111, 135-142.

Nofar, M., Sacligil, D., Carreau, P. J., Kamal, M. R., and Heuzey, M. C. (2019). "Poly (lactic acid) blends: Processing, properties and applications." *International Journal of Biological Macromolecules*, 125, 307-360.

Nurul Fazita, M.R., Jayaraman, K., Bhattacharyya, D., Mohamad Haafiz, M.K., Saurabh, C.K., Hussin, M.H. and HPS, A.K. (2016). "Green composites made of bamboo fabric and poly (lactic) acid for packaging applications—A review", *Materials*, 9(6), 435.

Othmani, C., Taktak, M., Zain, A., Hantati, T., Dauchez, N., Elnady, T., Fakhfakh, T. and Haddar, M. (2017). "Acoustic characterization of a porous absorber based on recycled sugarcane wastes." *Applied Acoustics*, 120, 90-97.

Park, J. H., Minn, K. S., Lee, H. R., Yang, S. H., Yu, C. B., Pak, S. Y., Oh, C. S., Song, Y. S., Kang , Y. J., and Youn, J. R. (2017). "Cell openness manipulation of low density

polyurethane foam for efficient sound absorption." *Journal of Sound and Vibration*, 406, 224-236.

Petinakis, E., Yu, L., Edward, G., Dean, K., Liu, H., and Scully, A. D. (2009). "Effect of matrix–particle interfacial adhesion on the mechanical properties of poly (lactic acid)/wood-flour micro-composites." *Journal of Polymers and the Environment*, 17(2), 83-94.

Pispola, G., Horoshenkov, K. V., and Asdrubali, F. (2005). "Transmission loss measurement of consolidated granular media (L)." *The Journal of the Acoustical Society of America*, 117(5), 2716-2719.

Plarre, R., Zocca, A., Spitzer, A., Benemann, S., Gorbushina, A. A., Li, Y., Anja Waske., Alexander Funk., Janka Wilbig., and Jens, Gunster. (2021). "Searching for biological feedstock material: 3D printing of wood particles from house borer and drywood termite frass." *Plos One*, 16(2), e0246511.

Porras A., and Maranon, A. (2012). "Development and characterization of a laminate composite material from polylactic acid (PLA) and woven bamboo fabric", *Composites: Part B* 43, 2782–2788.

Putra, A., Abdullah, Y., Efendy, H., Farid, W. M., Ayob, M. R., and Py, M. S. (2013). "Utilizing sugarcane wasted fibers as a sustainable acoustic absorber." *Procedia Engineering*, 53, 632-638.

Qian, Y. J., Cui, K., Liu, S. M., Li, Z. B., Kong, D. Y., and Sun, S. M. (2014). "Numerical study of the acoustic properties of micro-perforated panels with tapered hole." *Noise Control Engineering Journal*, 62(3), 152-159.

Qian, Y. J., Kong, D. Y., Liu, S. M., Sun, S. M., and Zhao, Z. (2013). "Investigation on micro-perforated panel absorber with ultra-micro perforations." *Applied Acoustics*, 74(7), 931-935.

Rice, H. J., Kennedy, J., Goransson, P., Dowling, L., and Trimble, D. (2020). "Design of a Kelvin cell acoustic metamaterial." *Journal of Sound and Vibration*, 472, 115167.

Robin, O., Berry, A., Doutres, O., and Atalla, N. (2014). "Measurement of the absorption coefficient of sound absorbing materials under a synthesized diffuse acoustic field." *The Journal of the Acoustical Society of America*, 136(1), EL13-EL19.

Sakagami, K., Morimoto, M., Yairi, M., and Minemura, A. (2008). "A pilot study on improving the absorptivity of a thick microperforated panel absorber." *Applied Acoustics*, 69(2), 179-182.

Singh, H., and Jain, A. K. (2009). "Ignition, combustion, toxicity, and fire retardancy of polyurethane foams: a comprehensive review." *Journal of Applied Polymer Science*, 111(2), 1115-1143.

Singh, S., and Mohanty, A. R. (2018). "HVAC noise control using natural materials to improve vehicle interior sound quality." *Applied Acoustics*, 140, 100–109.

Soltani, P., Taban, E., Faridan, M., Samaei, S. E., and Amininasab, S. (2020). "Experimental and computational investigation of sound absorption performance of sustainable porous material: Yucca Gloriosa fiber." *Applied Acoustics*, 157, 106999.

Stloukal, P., Kalendova, A., Mattausch, H., Laske, S., Holzer, C., and Koutny, M. (2015). "The influence of a hydrolysis-inhibiting additive on the degradation and biodegradation of PLA and its nanocomposites." *Polymer Testing*, 41, 124-132.

Taban, E., Soltani, P., Berardi, U., Putra, A., Mohammad, S., Faridan, M., Ehsan, S., and Khavanin, A. (2020). "Measurement , modeling , and optimization of sound absorption performance of Kenaf fibers for building applications." *Building and Environment.*, 180, 107087.

Tao, Y., Wang, H., Li, Z., Li, P., and Shi, S. Q. (2017). "Development and application of wood flour-filled polylactic acid composite filament for 3D printing." *Materials*, 10(4), 339.

Tarvainen, K., Estlander, T., Jolanki, R., and Kanerva, L. (1994). "Occupational dermatoses caused by man-made mineral fibers." *Dermatitis*, 5(1), 22-29.

Tayong, R., Dupont, T., & Leclaire, P. (2010). "On the variations of acoustic absorption peak with particle velocity in micro-perforated panels at high level of excitation." *The Journal of the Acoustical Society of America*, 127(5), 2875-2882.

Temiz, M. A., Lopez Arteaga, I., Efraimsson, G., Åbom, M., and Hirschberg, A. (2015). "The influence of edge geometry on end-correction coefficients in micro perforated plates." *The Journal of the Acoustical Society of America*, 138(6), 3668-3677.

Travieso-Rodriguez, J. A., Zandi, M. D., Jerez-Mesa, R., and Lluma-Fuentes, J. (2020). "Fatigue behavior of PLA-wood composite manufactured by fused filament fabrication." *Journal of Materials Research and Technology*, 9(4), 8507-8516.

Vasina, M., Monkova, K., Monka, P. P., Kozak, D., and Tkac, J. (2020). "Study of the sound absorption properties of 3D-printed open-porous ABS material structures." *Polymers*, 12(5), 1062.

Vigneshwaran, K., and Venkateshwaran, N. (2019). "Statistical analysis of mechanical properties of wood-PLA composites prepared via additive manufacturing." *International Journal of Polymer Analysis and Characterization*, 24(7), 584-596.

Wang, T., Sokolinsky, V. S., Rajaram, S., and Nutt, S. R. (2005). "Assessment of sandwich models for the prediction of sound transmission loss in unidirectional sandwich panels." *Applied Acoustics*, 66(3), 245–262.

Wu, Y., Yang, M., and Sheng, P. (2018). "Perspective: Acoustic metamaterials in transition." *Journal of Applied Physics*, 123(9), 090901.

Xu, W., Pranovich, A., Uppstu, P., Wang, X., Kronlund, D., Hemming, J., Öblom, H., Moritz, N., Preis, M., Sandler, N., Willför, S., and Xu, C (2018). "Novel biorenewable composite of wood polysaccharide and polylactic acid for three dimensional printing." *Carbohydrate polymers*, 187, 51-58.

Zielinski, T. G. (2015). "Generation of random microstructures and prediction of sound velocity and absorption for open foams with spherical pores." *The Journal of the Acoustical Society of America*, 137(4), 1790-1801.

Zhang, C., Li, J., Hu, Z., Zhu, F., and Huang, Y. (2012b). "Correlation between the acoustic and porous cell morphology of polyurethane foam: Effect of interconnected porosity." *Materials and Design*, 41, 319-325.

Zhang, H., Wen, J., Xiao, Y., Wang, G., and Wen, X. (2015). "Sound transmission loss of metamaterial thin plates with periodic subwavelength arrays of shunted piezoelectric patches." *Journal of Sound and Vibration*, 343, 104-120.

Zhang, Q., Shi, L., Nie, J., Wang, H., and Yang, D. (2012a). "Study on poly (lactic acid)/natural fibers composites." *Journal of applied polymer science*, 125(S2), E526-E533.

LIST OF PUBLICATIONS

INTERNATIONAL JOURNALS

1. <u>R. Sailesh</u>, L. Yuvaraj, Jeyaraj Pitchaimani, Mrityunjay Doddamani, Lenin Babu Mailan Chinnapandi (2021) "Acoustic behaviour of 3D printed bio-degradable micro-perforated panels with varying perforation cross-sections". Applied Acoustics, Volume 174 : Art. No.107769 (**Elsevier, SCI, IF – 2.639**)

2. <u>R. Sailesh</u>, L. Yuvaraj, Mrityunjay Doddamani, Lenin Babu Mailan Chinnapandi, Jeyaraj Pitchaimani (2022) "Sound absorption and transmission loss characteristics of 3D printed bio-degradable material with graded spherical perforations". Applied Acoustics, Volume 186 : Art. No.108457 (**Elsevier, SCI, IF – 2.639**)

BIO-DATA

1. Name	: Sailesh R
2. Father's Name	: M Raju
3. Date of Birth	: 15th July 1975
4. Nationality	: Indian
5. Marital Status	: Married
6. Address	: Department of Mechanical Engineering, National Institute of Technology Karnataka, Surathkal, P.O. Srinivasnagar – 575 025 Karnataka, India.
7. Mobile Number	: +91 9497265051
8. E-mail id.	: saileshraju@gmail.com
9. Educational Qualification	:

Qualification	University/Board	Year of Passing
Ph.D. (Mechanical engineering)	National Institute of Technology Karnataka, Surathkal, Mangalore	Pursuing
M.Tech (Machine Design)	Kerala University, Thiruvananthapuram	2010
B.Tech (Mechanical Engineering)	University of Calicut	1998